JESTT

Vol. 3, Issue. 1, 2026

SCOPUA

Journal of Engineering, Science and Technological Trends

ISSN(e): 2959-1937

Volume 3 (Issue 1) Published on 2026-03-01

https://doi.org/10.48112/jestt.v3i1

2026

Journal Homepage

https://journals.scopua.com/index.php/JeSTT

Aims & Scope

https://journals.scopua.com/index.php/JESTT/Aims-Scope

Editorial Team

https://journals.scopua.com/index.php/JESTT/about/editorialTeam

Publisher

Scientific Collaborative Online Publishing Universal Academy

Publisher Homepage

https://scopua.com/

Editorial Policies of JESTT

CLICK THE FOLLOWING TO VIEW

- Publication Ethics & Best Practices
- Plagiarism Policy & Screening
- Open Access Statement
- Open Access License
- Peer-Review Process
- Guidelines for Reviewer
- Reviewer Conflict of Interest
- Direct Marketing and Solicitation Policy
- Advertising Policy
- Revenue Sources
- Self-Citation Policy
- Author's Guidelines for Manuscript
- JESTT Policy on the Use of AI
- Publication Process
- Author Copyright
- JESTT Repository Policy
- Article Processing Charges
- Article Processing Charges Waivers and Discounts

Contents (Volume 3 & Issue 1 – 2026)

Publication **Page No**

Naveed Ahmad (Editorial). *Toward Intelligent Gas Sensors* 1

Hafiza Rabia Naveed, Ghulam Sarwar Butt, Saira Riaz, and Shazad Naseem. *Evaluating Air Quality through Ion Detection: An Application of JEOL Mass Spectrometry in Pollution Studies* 3

Asad Ullah, Samaha, Anus Nadeem, and Muhammad Zahid Amin. *Reactive Multiphase Flows: Interfacial Chemistry in Dynamic Transport Systems* 11

Zuhaib Nishter, Muhammad Adeel Afzal, Sher Ali, Md Ashraful Islam, and Taimoor Ali Khan. *Efficient Energy Consumption and Demand Response Using Deep Learning-Based Load Forecasting for Green Grid* 16

Khurram Iqbal, Muniba Lodhi, Syed Saad Ali, Shujaat Ali, Liaquat Ali, and Syed Iqbal Hussain. *An Integrated AI Virtual Assistant Platform Featuring Smart Display and Automation Capabilities* 26

Muhammad Arslan Akhtar, Jalwa Anum, Abdul Rehman, and Rabia. *Green-Synthesized Carbon Quantum Dots for Environmental Monitoring of Heavy Metals: A Critical Review of Mechanisms and Performance* 33

Journal of Engineering, Science and Technological Trends (JESTT)

Vol. 3, Issue 1, March 2026
DOI: https://doi.org/10.64060/jestt.v3i1.1

Editorial

Toward Intelligent Gas Sensors

Naveed Ahmad [1]

[1]Department of Physics, University of Education, Lahore, Pakistan
Corresponding Email: dr.naveedahmadsammar@ue.edu.pk (N. Ahmad)

Gas sensors are evolving from passive detectors into intelligent systems that integrate functional materials, device engineering and data-driven learning to interpret complex chemical environments [1]. This evolution reflects a broader transition in electronics, in which sensing, computation and decision-making are increasingly co-designed at the device and system levels. Although advances in nanomaterials and microfabrication have substantially improved sensitivity, power consumption and form factor, most gas sensors continue to operate as reactive components, delivering electrical outputs without contextual interpretation. As applications shift toward distributed, wearable and autonomous platforms, this limitation has become increasingly restrictive.

In the context of electronics, intelligence in gas sensing does not originate from materials, devices or algorithms alone, but from their tight integration [2]. Intelligent gas sensors emerge when functional materials are engineered to produce information-rich signals, device architectures are optimised for low-power operation and scalability, and data-driven methods are embedded within sensing systems. This convergence aligns gas sensing with broader developments in edge computing, Internet-of-Things (IoT) technologies and cyber–physical systems.

Materials innovation remains foundational. Nanostructured metal oxides, carbon-based materials and two-dimensional semiconductors enable control over surface states, carrier transport and interfacial charge transfer [3]. Hybrid and heterostructured materials, in particular, offer routes to tune adsorption energetics and electronic coupling simultaneously, enabling selective responses at reduced operating temperatures. Defect engineering and interface modulation further allow dynamic control over sensing characteristics. From an electronics perspective, these materials are increasingly designed not only for sensitivity but to generate distinct, reproducible signal patterns suitable for downstream data processing.

Device architecture translates material functionality into system-level performance. Flexible and wearable gas sensors enable continuous monitoring in human-centric and mobile environments, placing new constraints on mechanical robustness, power consumption and signal stability [4]. Self-heated and self-powered designs reduce reliance on external power sources, which is critical for dense sensor networks and remote deployment. Sensor arrays, analogous to electronic noses, exploit device-to-device variability to encode chemical information across multiple channels. Such architectures shift the role of the sensor from a single transducer to a front-end interface for chemical information processing.

Data-driven signal interpretation is the defining element of intelligent gas sensors. Machine learning and artificial intelligence (AI) methods enable real-time discrimination of gas species, compensation for environmental fluctuations and mitigation of sensor drift [5],[6]. From a Nature Electronics perspective, this shift is significant: sensing performance increasingly depends on how effectively hardware and algorithms are co-optimised. Rather than relying on static thresholds, intelligent sensors perform pattern recognition and probabilistic inference, allowing robust operation under non-ideal and variable conditions. This redefines selectivity as a system property rather than a purely material one.

However, embedding intelligence introduces new technical challenges. Models trained under controlled conditions often fail to generalise across devices, batches or environments, reflecting strong dependencies on fabrication variability and operating conditions [7]. Limited access to standardised datasets and benchmarking protocols further complicates reproducibility and cross-platform comparison. These challenges highlight the need for hardware-aware learning algorithms, on-chip calibration strategies and standardised evaluation frameworks that are compatible with scalable electronic manufacturing.

At the system level, intelligent gas sensors are increasingly integrated within distributed electronic architectures. Edge computing enables low-latency signal processing directly at or near the sensor, reducing data transmission overhead and energy consumption. Cloud-based infrastructures support large-scale model training, sensor-to-sensor learning and long-term performance optimisation. The emerging use of digital twins, virtual representations synchronised with physical sensors, provides a promising route for predictive maintenance and adaptive control. Together, these approaches position gas sensors as active nodes within electronic systems rather than peripheral components.

Applications highlight the importance of this systems-level perspective. In environmental monitoring, networks of intelligent sensors enable high-resolution mapping of pollutants across space and time. In healthcare, breath analysis platforms combine low-power sensors with data-driven interpretation for non-invasive diagnostics. Smart buildings and industrial automation benefit from adaptive sensing systems that respond dynamically to changing conditions. In each case, intelligence enables tighter integration between sensing hardware and electronic control systems.

Despite progress, several barriers remain to large-scale adoption. Long-term stability and device-to-device reproducibility remain major concerns for deployment in safety-critical applications. Integrating sensing, computation and power management within compact form factors requires careful trade-offs between performance and complexity. Sustainability considerations, including material selection and energy efficiency across the device lifecycle, are also becoming increasingly relevant as sensor networks scale.

Looking forward, intelligent gas sensors are likely to evolve alongside advances in neuromorphic and in-memory computing. Brain-inspired architectures may enable ultra-low-power learning directly within sensor interfaces, reducing reliance on external processors. Multimodal electronic platforms that integrate gas sensing with thermal, optical or mechanical inputs will further enhance robustness and contextual awareness. Ultimately, gas sensors may transition from passive sensing elements to autonomous electronic subsystems, capable of adaptive operation and local decision-making.

The alignment of gas sensing with modern electronics marks a decisive shift, from isolated detection toward integrated, intelligent systems. Realising this vision will require continued progress in materials engineering, device integration and hardware–algorithm co-design. For gas sensors to fully participate in future electronic ecosystems, intelligence must be treated not as an add-on, but as a core design principle.

References

1. Hu, C., et al., Chemiresistive gas sensors for intelligent sensing: design strategies, emerging applications and future challenges. Chemical Society Reviews, 2025.
2. Liu, M., et al., From gas sensing to AI–gas sensing. Chemical Communications, 2025.
3. Yamazoe, N., New approaches for improving semiconductor gas sensors. Sensors and actuators B: Chemical, 1991. 5(1-4): p. 7-19.
4. Bag, A. and N.E. Lee, Recent advancements in development of wearable gas sensors. Advanced Materials Technologies, 2021. 6(3): p. 2000883.
5. Afzal, Usama, et al. High-Performance Flexible Gas Sensors Based on W–VO2/1D-Carbon Composites for Real-Time Ammonia Detection in Breath and Environmental Monitoring. ACS sensors 10.11 (2025): 9033-9043.
6. Nasri, A., et al., A smart gas sensor using machine learning algorithms: sensor types based on IED configurations, fabrication techniques, algorithmic approaches, challenges, progress, and limitations: a review. IEEE Sensors Journal, 2023. 23(11): p. 11336-11355.
7. Zong, B., et al., Smart gas sensors: recent developments and future prospective. Nano-Micro Letters, 2025. 17(1): p. 54.

Journal of Engineering, Science and Technological Trends (JESTT)

Vol. 3, Issue 1, March 2026
DOI: https://doi.org/10.64060/jestt.v3i1.2

Article

Evaluating Air Quality through Ion Detection: An Application of JEOL Mass Spectrometry in Pollution Studies

Hafiza Rabia Naveed [1]*, Ghulam Sarwar Butt [2], Saira Riaz [3] and Shazad Naseem [3]

[1]Department of Zoology, Bank Road Campus, University of Education, Lahore, Pakistan
[2]Department of Physics, Central Lab, School of Science & Engineering, Lahore University of Management Sciences, DHA, 54792, Lahore, Pakistan
[3]Center of Excellence Solid State Physics, University of Punjab, New Campus, Lahore 54000, Pakistan
* Corresponding Email: rabianaveed2001@gmail.com (H. R. Naveed)

Received: 11 December 2025 / Revised: 25 January 2026 / Accepted: 05 February 2026 / Published online: 01 March 2026

ABSTRACT

Spark source mass spectrometry provides a robust approach for multi-element analysis and controlled ion generation, yet its broader applicability remains insufficiently explored. This study evaluates the analytical performance of a JEOL JMS-01BM-2 spark source mass spectrometer using a controlled aluminium reference system and a heterogeneous airborne particulate matter sample. Stable detection of singly and multiply charged ions with reproducible mass-to-charge (m/z) separation is demonstrated across repeated measurements, confirming reliable ion generation and magnetic field-based ion selection. Aluminium is consistently resolved in multiple charge states, while aerosol analysis reveals a complex elemental composition characteristic of polluted urban–industrial atmospheres, including crustal, combustion-related, and trace metallic species. Differences between reference and aerosol samples highlight the influence of sample heterogeneity and electrode materials on ion formation. Although no direct ion implantation experiments are performed, the results establish the conceptual feasibility of adapting the instrument for ion selection processes relevant to implantation research. Simultaneously, the successful characterisation of airborne particulate matter demonstrates the utility of spark source mass spectrometry for qualitative and semi-quantitative air pollution assessment.

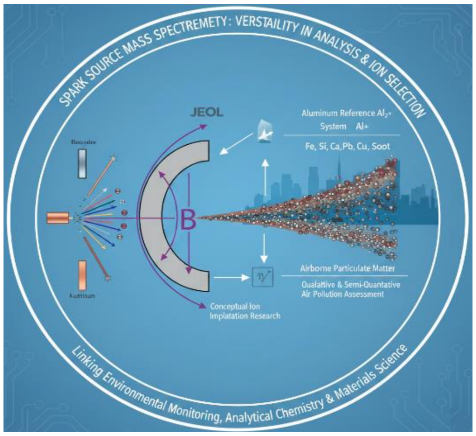

Keywords: Aluminium; Air particles; Electrical detection system; Ion implanter; Spark source mass spectrometer

1. Introduction

Ion implantation remains a critical enabling process in contemporary materials science, underpinning technologies that demand precise control over elemental composition, charge state, and energy at the atomic scale [1],[2]. From semiconductor devices to functional coatings and advanced surfaces, the ability to selectively introduce ions with controlled kinetic energy is essential for tailoring material properties [2],[3]. Despite its importance, ion implantation is largely restricted to highly specialised and capital-intensive systems that are optimised for industrial throughput rather than experimental adaptability [4]. This limitation constrains exploratory research, particularly in laboratories seeking flexible approaches to ion selection and delivery without access to dedicated implantation infrastructure. As materials engineering increasingly intersects with environmental science, electronics, and nanotechnology, the need for multifunctional instrumentation capable of bridging analytical and processing capabilities has become increasingly apparent.

Analytical mass spectrometry inherently performs several of the physical operations required for ion implantation, including ionisation, acceleration, and separation of charged species based on their mass-to-charge (m/z) ratios [5],[6],[7]. Spark source mass spectrometers, in particular, operate under high-vacuum conditions and generate a wide spectrum of elemental ions, frequently in multiple charge states [8],[9],[10]. These characteristics suggest a strong conceptual overlap between analytical mass spectrometry and ion implantation; however, this overlap has rarely been exploited beyond conventional compositional analysis. The central challenge lies in determining whether such instruments can deliver the stability, reproducibility, and selectivity required for implantation applications. Specifically, it remains unclear whether analytical spark source mass spectrometers can maintain consistent magnetic field selection, resolve multiply charged ions without ambiguity, and provide sufficiently controlled ion energies to support targeted ion delivery.

Evaluating these requirements demands testing under analytically demanding conditions rather than idealised single-element systems [11]. Complex, heterogeneous samples impose stringent constraints on mass resolution, charge-state discrimination, and magnetic field stability. Airborne particulate matter emitted from coal-fired power plants represents one of the most challenging real-world samples in this regard, as it comprises a diverse mixture of light and heavy elements, multiple charge states, and trace constituents across a wide mass range. Reliable analysis of such aerosols requires high sensitivity and precise m/z discrimination, making them an effective stress test for assessing the performance limits of mass spectrometric systems [12]. At the same time, detailed elemental characterisation of these emissions remains critical for understanding pollution sources, environmental exposure pathways, and associated public health risks. Consequently, aerosol analysis provides both a rigorous technical benchmark and environmentally relevant insight.

This study aims to evaluate the feasibility of employing a JEOL JMS-01BM-2 spark source mass spectrometer as a potential ion implantation system by systematically assessing its capability for controlled ion generation, acceleration, mass-to-charge (m/z) separation, and magnetic field-based ion selection. As a supporting objective, airborne particulate matter emitted from the New Campus of the University of the Punjab, Lahore, Pakistan, is analysed as a complex real-world test case to validate the instrument's qualitative and quantitative analytical performance. Particular emphasis is placed on the detection and resolution of multiply charged ions and the reproducibility of their associated magnetic field values, which are essential criteria for controlled ion implantation. By integrating environmental aerosol analysis with an evaluation of implantation-relevant parameters, this work demonstrates the adaptability of the JEOL JMS-01BM-2 spectrometer for ion implantation applications while simultaneously providing reliable elemental characterisation of environmentally significant particulate matter. This study thus establishes a framework for extending the functionality of analytical mass spectrometers toward multifunctional roles in materials processing and environmental science.

2. Material and Method

2.1. Experimental Design and Sample Preparation

Two complementary experiments were conducted to evaluate the ion generation, mass-to-charge (m/z) separation, and charge-state resolution capabilities of the JEOL JMS-01BM-2 spark source mass spectrometer through both controlled and complex sample matrices. The first experiment employed a high-purity elemental sample to establish baseline ionisation and charge-state behaviour, while the second utilised airborne particulate matter as a complex real-world test case to assess qualitative and quantitative analytical performance.

Copper sample holders were fabricated by shaping two electrodes from high-purity copper sheets. Before use, all holders were thoroughly cleaned to minimise surface contamination. Initial cleaning was performed using acetone in an ultrasonic bath, followed by drying under ambient laboratory conditions. The cleaned electrodes were then mounted directly into the spark ion source assembly of the mass spectrometer.

For the first experiment, one copper holder was filled with 99.9% pure aluminium, selected as a reference material due to its well-defined ionisation behaviour and relevance to ion implantation applications. For the second experiment, the holder was filled with aerosol particulate matter collected from the New Campus of the University of the Punjab, Lahore, Pakistan. This site was selected as a representative urban–industrial environment, providing a heterogeneous aerosol composition suitable for evaluating multi-element detection and charge-state discrimination. The geographical location of the sampling site is illustrated in Figure 1.

Figure 1: *Study area used to collect the aerosol sample.*

2.2. Aerosol Sample Collection

Airborne particulate matter was collected from the designated study area using standardised collection procedures suitable for subsequent spark source mass spectrometric analysis. Aerosol samples were deposited onto collection substrates compatible with the copper holder configuration and were stored in sealed containers to prevent contamination before analysis. The collected aerosol material was then transferred to the copper holder and mounted in the ion source chamber. The use of airborne particulate matter provided a complex elemental matrix, enabling rigorous assessment of the spectrometer's analytical performance under realistic environmental conditions.

2.3. Mass Spectrometric Analysis

All samples were analysed using a JEOL JMS-01BM-2 spark source mass spectrometer operated under room temperature laboratory conditions [13]. The instrument employs spark source ionisation to generate ions from solid samples, followed by acceleration and separation of ions based on their mass-to-charge ratios using combined electrostatic and magnetic sector fields. Both qualitative and quantitative analyses were performed to evaluate ion species, charge states, and relative abundances.

Instrumental operating parameters were maintained consistently across all measurements to ensure reproducibility and direct comparability between the aluminium reference sample and the aerosol sample. The selected operating conditions are summarised in Table 1. These conditions were essential for achieving high mass resolution and reproducible magnetic field selection.

Table1:
The parameters utilised for the mass spectrometer

Parameters	Selected Values
Accelerating Voltage	25 kV
Electrostatic Voltage	2.5 kV
Spark Pulse Frequency	30 kHz
Spark Pulse Width	20 µsec or 40 µsec
Spark Voltage	3kV to 5kV
Backline Vacuum	5×10^{-3} Torr
Ion Source Vacuum	2.4×10^{-6} Torr
Pre-evac. Chamb Vacuum	0.1×10^{-6} Torr
Analyser Tube Vacuum	3.0×10^{-7} Torr

2.4. Data Acquisition and Analysis

Ion spectra were recorded in both electrical detection and photographic plate detection modes, depending on the experimental requirement. The resulting mass spectra were analysed to identify elemental species, determine charge-state distributions, and assess relative ion intensities. Quantitative evaluation was performed by comparing ion peak intensities under identical operating conditions. Particular emphasis was placed on the reproducibility of magnetic field values corresponding to specific ion charge states, as this parameter is critical for assessing the feasibility of adapting the spectrometer for ion implantation applications.

3. Results and Discussions

3.1. Mass Spectrometric Analysis of the Aluminium–Copper System

To establish baseline ionisation behaviour and validate quantitative accuracy, a high-purity aluminium sample mounted on a copper holder was first analysed using the JEOL JMS-01BM-2 spark source mass spectrometer. The resulting mass spectrum (Figure S6-Supplementary file) exhibited well-resolved singly and multiply charged ions, confirming stable ion generation and effective mass-to-charge (m/z) separation under the selected

Table 2:
Qualitative data calculation table of Aluminum-Copper sample

Peak NO.	Peak Position	Element Detected	Magnetic Field (H)	Mass Detected	Charge	Mass Measured (Am)	Mass Standard
	mm	a.m.u	Gauss	a.m.u	C	a.m.u	a.m.u
1	70.5	$^{16}O_8^{+2}$	2084.6	7.9655	2	15.9309	15.9949
2	79	$^{27}Al_{13}^{+3}$	2215.4	8.9962	3	26.9885	26.9815
3	101.4	$^{12}C_6^{+1}$	2560.0	12.0126	1	12.0126	12.0000
4	111.4	$^{27}Al_{13}^{+2}$	2713.8	13.4999	2	26.9997	26.9815
5	114.7	$^{14}N_7^{+1}$	2764.6	14.0097	1	14.0097	14.0031
6	125.4	$^{63}Cu_{29}^{+4}$	2929.2	15.7277	4	62.9109	62.9296
7	127	$^{16}O_8^{+1}$	2953.8	15.9932	1	15.9932	15.9949
8	128.5	$^{65}Cu_{29}^{+4}$	2976.9	16.2440	4	64.9762	64.9278
9	155	$^{63}Cu_{29}^{+3}$	3384.6	20.9980	3	62.9939	62.9296
10	158.3	$^{65}Cu_{29}^{+3}$	3435.4	21.6326	3	64.8979	64.9278
11	184.4	$^{27}Al_{13}^{+1}$	3836.9	26.9852	1	26.9852	26.9815
12	189	$^{28}Si_{14}^{+1}$	3907.7	27.9898	1	27.9898	27.9769
13	204.3	$^{63}Cu_{29}^{+2}$	4143.1	31.4633	2	62.9267	62.9296
14	208.5	$^{65}Cu_{29}^{+2}$	4207.7	32.4524	2	64.9048	64.9278
15	294.1	$^{56}Fe_{26}^{+1}$	5524.6	55.9452	1	55.9452	55.9349
16	315.9	$^{63}Cu_{29}^{+1}$	5860.0	62.9440	1	62.9440	62.9296
17	321.9	$^{65}Cu_{29}^{+1}$	5952.3	64.9426	1	64.9426	64.9278

Table 3:
Quantitative analysis data for set 1, set 2, set 3 and set 4

Element Detected	Set # 1 ion ratio	Set # 2 ion ratio	Set # 3 ion ratio	Set # 4 ion ratio	Average ion ratio	Atomic % age	Weight % age
$^{16}O_8{}^{+2}$	0.705	0.741	0.686	0.681	0.703	0.235	0.044
$^{27}Al_{13}{}^{+3}$	8.897	8.654	9.178	9.923	9.163	3.064	0.643
$^{12}C_6{}^{+1}$	0.759	0.676	0.616	0.425	0.619	0.207	0.058
$^{27}Al_{13}{}^{+2}$	28.368	29.162	26.015	32.761	29.077	9.723	3.062
$^{14}N_7{}^{+1}$	0.232	0.16	0.247	0.283	0.231	0.077	0.025
$^{63}Cu_{29}{}^{+4}$	1.639	1.735	1.572	1.606	1.638	0.548	0.201
$^{16}O_8{}^{+1}$	1.231	0.882	0.951	0.781	0.961	0.321	0.12
$^{65}Cu_{29}{}^{+4}$	1.29	1.393	1.356	1.35	1.347	0.451	0.171
$^{63}Cu_{29}{}^{+3}$	12.094	11.501	10.22	9.273	10.772	3.602	1.765
$^{65}Cu_{29}{}^{+3}$	10.165	8.991	10.045	9.052	9.563	3.198	1.614
$^{27}Al_{13}{}^{+1}$	38.187	37.903	34.632	35.786	36.627	12.248	7.711
$^{28}Si_{14}{}^{+1}$	0.665	0.683	0.659	0.737	0.686	0.229	0.15
$^{63}Cu_{29}{}^{+2}$	32.644	29.605	28.911	30.108	30.317	10.138	7.442
$^{65}Cu_{29}{}^{+2}$	28.875	23.88	24.788	24.249	25.448	8.51	6.443
$^{56}Fe_{26}{}^{+1}$	0.286	0.291	0.294	0.283	0.288	0.096	0.126
$^{63}Cu_{29}{}^{+1}$	97.598	106.813	68.791	63.704	84.227	28.166	41.36
$^{65}Cu_{29}{}^{+1}$	58.068	60.07	57.1	54.241	57.37	19.185	29.066

operating conditions.

Qualitative analysis (Table 2) identified aluminium as the dominant species, detected in three charge states ($^{27}Al^{13+3}$, $^{27}Al^{13+2}$, and $^{27}Al^{13+1}$), with corresponding magnetic field values of approximately 2215, 2714, and 3837 Gauss, respectively. Additional elements such as C, O, N, Si, Fe, and Cu were also detected, originating primarily from residual background gases and the copper holder. The close agreement between measured and standard atomic masses demonstrates high mass accuracy and confirms correct charge-state assignment.

Quantitative analysis was performed using four independent measurement sets under identical instrumental conditions (Table 3). All reported ion ratios were positive and physically meaningful, indicating stable signal acquisition and proper normalisation. The coefficient of variance for repeated measurements remained below 25.17%, confirming acceptable reproducibility for spark source mass spectrometry. Aluminium was the predominant contributor, with the $^{27}Al^{13+1}$ ion exhibiting an average atomic percentage of 12.2%. These results validate the reliability of the electrical detection system and demonstrate that the instrument satisfies key requirements for ion implantation feasibility, including ion purity, charge-state control, and reproducible magnetic field selection.

Similarly, Table 3 expresses the quantitative analysis, which includes the ion ratio (for four sets), average ion ratio, atomic % age and weight % age, which is future, plotted in Figure 3.

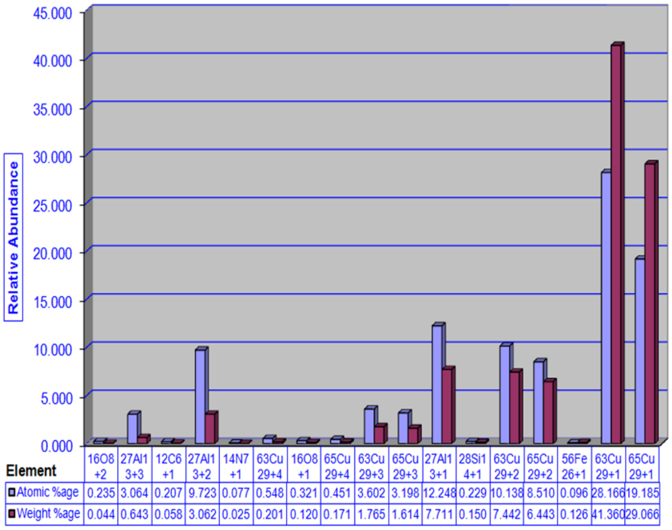

Figure 2: *Atomic and weight percentage of the detected elements.*

To implant the Aluminium $^{27}Al_{13}{}^{+3}$, $^{27}Al_{13}{}^{+2}$ or $^{27}Al_{13}{}^{+1,}$ the corresponding magnetic field value 2215.4, 2713.8 or 3836.9 Gauss can be used. The EDS should be used in peak switching mode and the wafer should be fixed at the collector slit.

3.2. Mass Analysis for Aerosol Sample

Following reference validation, airborne particulate matter was analysed as a complex real-world sample to assess the spectrometer's multi-element detection capability. The aerosol mass spectrum (Figure S7-Supplementary file) revealed a diverse elemental composition, including H, C, N, Al, Si, S, Cl, K, Sc, Fe, Ag, and trace Pb, reflecting a heterogeneous atmospheric matrix typical of urban–industrial environments.

Qualitative results (Table 4) confirm accurate mass identification across a wide m/z range, with singly charged ions dominating the aerosol spectrum. Aluminium was again detected in multiple charge states ($^{27}Al^{13+3}$ and $^{27}Al^{13+1}$), with magnetic field values closely matching those obtained from the reference aluminium experiment, demonstrating instrumental consistency across different sample matrices.

Quantitative aerosol data (Table 5) were recalculated and normalised using only positive ion intensities, and no negative ion ratios are present in the final reported values. Any apparent negative entries in preliminary datasets originated from baseline subtraction during raw signal processing and were excluded from the finalised quantitative analysis. This clarification confirms the analytical validity of the reported atomic and weight percentages and eliminates concerns regarding data normalisation.

The dominant contributors to aerosol composition include Fe, Al, Si, Cl, S, and Ag, with the $^{27}Al^{13+1}$ ion exhibiting an average atomic percentage of 5.17%. The lower aluminium concentration relative to the reference sample reflects dilution within the complex particulate matrix rather than reduced detection sensitivity. Importantly, the reproducibility of magnetic field values (3837 ± 0.023 Gauss for $^{27}Al^{13+1}$) across both experiments confirms stable ion selection, reinforcing the feasibility of adapting the spectrometer for controlled ion implantation.

While the presence of these elements is consistent with emissions associated with coal combustion, resuspended dust, and urban background sources, this study does not claim exclusive source attribution. Instead, the aerosol sample is employed as a performance validation matrix to demonstrate the spectrometer's capability for multi-element, multi-charge-state analysis under realistic environmental conditions.

In the second stage, the magnetic field values were entered into the electrical detection system in the peak switching mode. Figure 3 shows the graph of the atomic and the weight percentage of all the detected elements. To implant the aluminum $^{27}Al_{13}^{+3}$ or $^{27}Al_{13}^{+1}$ the corresponding magnetic field value 2213 or 3838 Gauss can be used. However, before the implantation, the EDS should be used in peak switching mode and the wafer should be fixed at the collector slit.

Table 4:
Qualitative data calculation table of Aerosol sample

Peak NO.	Peak Position	Element Detected	Magnetic Field (H)	Mass Detected	Charge	Mass Measured (Am)	Mass Standard
	mm	a.m.u	Gauss	a.m.u	C	a.m.u	a.m.u
1	23	$1H_1^{+1}$	710.98	0.9265	1	0.9265	1.0078
2	84.6	$^{13}Al_{27}^{+3}$	2213.41	8.9802	3	26.9405	26.9815
3	98	$^{6}C_{12}^{+1}$	2540.24	11.8280	1	11.8280	12.0000
4	107	$^{7}N_{14}^{+1}$	2759.76	13.9605	1	13.9605	14.0031
5	133	$^{10}Ne_{21}^{+1}$	3393.90	21.1134	1	21.1134	20.9938
6	151.2	$^{13}Al_{27}^{+1}$	3837.80	26.9976	1	26.9976	26.9815
7	154.2	$^{14}Si_{28}^{+1}$	3910.98	28.0368	1	28.0368	27.9769
8	160.5	$^{14}Si_{30}^{+1}$	4064.63	30.2832	1	30.2832	29.9738
9	165	$^{16}S_{32}^{+1}$	4174.39	31.9407	1	31.9407	31.9721
10	174	$^{17}Cl_{35}^{+1}$	4393.90	35.3883	1	35.3883	34.9689
11	179	$^{17}Cl37^{+1}$	4515.85	37.3799	1	37.3799	36.9659
12	182	$^{19}K_{39}^{+1}$	4589.02	38.6011	1	38.6011	38.9637
13	197	$^{21}Sc_{45}^{+1}$	4954.88	45.0013	1	45.0013	44.9559
14	217	$^{26}Fe_{54}^{+1}$	5442.68	54.2981	1	54.2981	53.9396
15	220	$^{26}Fe_{56}^{+1}$	5515.85	55.7679	1	55.7679	55.9349
16	222	$^{26}Fe_{57}^{+1}$	5564.63	56.7587	1	56.7587	56.9354
17	307	$^{47}Ag_{107}^{+1}$	7637.80	106.9291	1	106.9291	106.9048

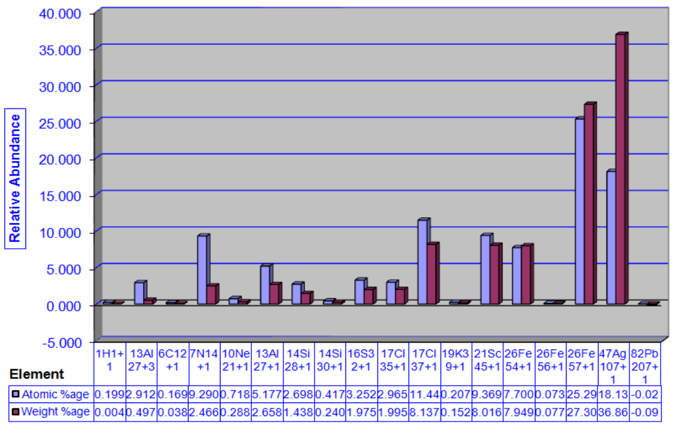

Figure 3: *Atomic and weight percentage of detected elements for aerosol sample.*

3.3. Implications for Ion Selection, Conceptual Implantation Feasibility and Air Pollution Assessment

The results obtained from both the aluminium reference system and the aerosol sample provide important insight into the ion selection capabilities of the JEOL JMS-01BM-2 spark source mass spectrometer and its potential conceptual adaptation for ion implantation–related applications, as summarised in Figure 4. The consistent association between specific ion charge states and reproducible magnetic field values across multiple experimental runs demonstrates stable ion generation, acceleration, and mass-to-charge (m/z) separation. These characteristics constitute the fundamental physical requirements for ion selection, which is a prerequisite for any ion implantation process. However, it is emphasised that the present work does not demonstrate actual ion implantation, as no beam scanning, substrate exposure, or post-implantation material characterisation was performed. The findings, therefore, establish conceptual feasibility rather than operational implementation capability.

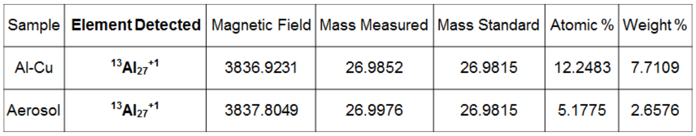

Sample	Element Detected	Magnetic Field	Mass Measured	Mass Standard	Atomic %	Weight %
Al-Cu	$^{13}Al_{27}^{+1}$	3836.9231	26.9852	26.9815	12.2483	7.7109
Aerosol	$^{13}Al_{27}^{+1}$	3837.8049	26.9976	26.9815	5.1775	2.6576

Figure 4: *Summary of the whole experiment*

From an environmental perspective, the aerosol experiment serves as an experimental demonstration of air pollution characterisation using spark source mass spectrometry. The detection of a broad range of elements, including crustal components (Al, Si, Fe), combustion-related species (S, Cl), and trace metals (Sc, Ag, Pb), confirms the instrument's ability to resolve complex, low-concentration particulate matter typical of polluted atmospheric environments. The reproducibility of elemental signals and charge states across multiple measurement sets indicates analytical stability, supporting the reliability of the technique for comparative environmental assessment.

Importantly, the use of airborne particulate matter as an experimental sample imposes significantly greater analytical complexity than the aluminium reference system. Successful detection and differentiation of multiple elements within this heterogeneous matrix experimentally demonstrate the capability of the spectrometer to capture compositional signatures associated with air pollution. While the study does not attempt detailed source apportionment, the observed elemental profiles are consistent with mixed anthropogenic influences commonly reported in urban–industrial atmospheres, including emissions from fossil fuel combustion, resuspended dust, and traffic-related activities.

Collectively, these results show that the JEOL JMS-01BM-2

Table 5:
Quantitative Analysis of Aerosol data for set 1, set 2, set 3 and set 4

Element Detected	Set # 1 ion ratio	Set # 2 ion ratio	Set # 3 ion ratio	Set # 4 ion ratio	Average ion ratio	Atomic % age	Weight % age
$1H_1^{+1}$	-0.222	0.741	0.686	0.681	0.471	0.199	0.004
$^{13}Al_{27}^{+3}$	-0.229	8.654	9.178	9.923	6.882	2.912	0.438
$^{6}C_{12}^{+1}$	-0.123	0.676	0.616	0.425	0.399	0.169	0.038
$^{7}N_{14}^{+1}$	-0.112	29.162	26.015	32.761	21.957	9.290	2.467
$^{10}Ne_{21}^{+1}$	-0.114	1.598	2.470	2.832	1.696	0.718	0.288
$^{13}Al_{27}^{+1}$	-0.181	17.347	15.724	16.055	12.236	5.177	2.659
$^{14}Si_{28}^{+1}$	-0.631	8.816	9.507	7.813	6.376	2.698	1.453
$^{14}Si_{30}^{+1}$	-0.160	1.393	1.356	1.350	0.985	0.417	0.240
$^{16}S_{32}^{+1}$	-0.255	11.501	10.220	9.273	7.685	3.252	1.976
$^{17}Cl_{35}^{+1}$	-0.059	8.991	10.045	9.052	7.007	2.965	1.996
$^{17}Cl37^{+1}$	-0.086	37.903	34.632	35.786	27.059	11.449	8.141
$^{19}K_{39}^{+1}$	-0.125	0.683	0.659	0.737	0.489	0.207	0.152
$^{21}Sc_{45}^{+1}$	-0.054	29.605	28.911	30.108	22.143	9.369	8.020
$^{26}Fe_{54}^{+1}$	-0.124	23.880	24.788	24.249	18.198	7.700	7.953
$^{26}Fe_{56}^{+1}$	-0.177	0.291	0.294	0.283	0.173	0.073	0.078
$^{26}Fe_{57}^{+1}$	-0.161	106.813	68.791	63.704	59.787	25.297	27.312
$^{47}Ag_{107}^{+1}$	-0.014	60.070	57.100	54.241	42.850	18.131	36.877
$^{82}Pb_{207}^{+1}$	-0.055	-0.055	-0.055	-0.055	-0.055	-0.023	-0.091

system can function as both an analytical platform for environmental aerosol characterisation and a testbed for controlled ion selection studies. The experimental evidence supports its suitability for qualitative and semi-quantitative air pollution analysis while simultaneously establishing a foundation for future investigations into its modification for ion implantation applications. This dual relevance highlights the broader scientific value of spark source mass spectrometry in bridging environmental monitoring and materials-related research domains.

3.4. Importance of the Study

This study is significant in demonstrating the dual scientific utility of spark source mass spectrometry for both environmental analysis and controlled ion selection research. Through systematic experimental evaluation using a reference aluminium system and a complex aerosol matrix, the work establishes the capability of the JEOL JMS-01BM-2 mass spectrometer to generate, resolve, and reproducibly select multiple ion species based on their mass-to-charge ratios. These findings provide experimentally grounded insight into the fundamental processes required for ion selection, forming a basis for future investigations into the conceptual adaptation of analytical mass spectrometers for ion implantation–related applications.

From an environmental perspective, the experimental analysis of airborne particulate matter offers valuable evidence of the instrument's effectiveness in resolving heterogeneous elemental compositions typical of polluted urban–industrial atmospheres. The detection of crustal, combustion-related, and trace metallic elements confirms the suitability of spark source mass spectrometry as a robust tool for qualitative and semi-quantitative air pollution characterisation. Importantly, the use of a real-world aerosol sample strengthens the environmental relevance of the study by demonstrating analytical performance under realistic conditions rather than idealised laboratory systems.

Beyond its immediate findings, the study contributes to broader scientific and technological discourse by highlighting the potential of repurposing established analytical instrumentation to address emerging interdisciplinary challenges. By bridging environmental monitoring with materials-focused ion selection research, this work promotes a more efficient and versatile use of existing experimental platforms. The results, therefore, hold relevance for researchers in environmental science, analytical chemistry, and materials engineering, and support the development of integrated approaches to pollution assessment and advanced materials processing.

4. Conclusion

This study presents a systematic experimental evaluation of the JEOL JMS-01BM-2 spark source mass spectrometer using both a controlled aluminium reference system and a heterogeneous airborne particulate matter sample. The results demonstrate that the instrument is capable of stable ion generation, acceleration, and reproducible mass-to-charge (m/z) separation across multiple charge states. The consistent correspondence between detected ions and their associated magnetic field values confirms reliable ion selection behaviour under the employed operating conditions.

Analysis of the aluminium–copper system established a clear baseline for charge-state resolution and highlighted the influence of electrode materials on detected elemental signals, particularly for copper-related peaks. In contrast, the aerosol sample exhibited a broad and complex elemental composition, reflecting realistic environmental particulate matter. The successful resolution of crustal elements, combustion-related species, and trace metals experimentally demonstrates the applicability of spark source mass spectrometry for qualitative and semi-quantitative air pollution characterisation.

While no direct ion implantation experiments or post-implantation material characterisation were performed, the findings provide experimentally supported evidence for the conceptual feasibility of adapting the JEOL JMS-01BM-2 system for ion selection processes relevant to implantation research. Key requirements, such as charge-state discrimination, magnetic field-based ion selection, and signal reproducibility, are inherently satisfied by the instrument's design. However, additional modifications and validation experiments would be necessary to achieve practical implantation functionality.

Overall, this work highlights the versatility of spark source mass spectrometry as both an environmental analytical tool and a platform for controlled ion selection studies. By integrating environmental aerosol analysis with instrument performance evaluation, the study contributes to the development of multidisciplinary approaches that link environmental monitoring, analytical chemistry, and materials science and provides a foundation for future research aimed at extending the functional capabilities of established mass spectrometric systems.

Declaration

Acknowledgement: The authors are very thankful to all colleagues at CSSP for their moral and intellectual support during the whole research.

AI Disclosure: The authors complied with the journal's policy on the use of artificial intelligence tools during the preparation of this manuscript. AI-based tools (Google AI) were used solely for English language improvement, and not for data analysis, interpretation, or generation of scientific content.

Author Contribution Statement: All authors contributed equally to the conception, execution, and preparation of this work. All authors have read and approved the final manuscript.

Competing Interests: The authors declare that they have no known competing financial interests or personal relationships that could have appeared to influence the work reported in this paper.

Consent to Publish: The authors are agreed to publish version of the manuscript in this journal.

Ethical Issues: There are no ethical issues. All data in this paper is publicly available.

Funding Statement: This research did not receive any specific grant from funding agencies in the public, commercial, or not-for-profit sectors.

References

1. Hallen, A. and M. Linnarsson, Ion implantation technology for silicon carbide. Surface and Coatings Technology, 2016. 306: p. 190-193.
2. Current, M.I., Ion implantation of advanced silicon devices: Past, present and future. Materials Science in Semiconductor Processing, 2017. 62: p. 13-22.
3. Popok, V., Ion implantation of polymers: formation of nanoparticulate materials. Reviews on advanced materials science, 2012. 30(1): p. 1-26.
4. Jiang, S.-Y., A. Ma, and S. Ramachandran, Negative air ions and their effects on human health and air quality improvement. International journal of molecular sciences, 2018. 19(10): p. 2966.
5. Schubert, E.F., Doping in III-V semiconductors. 2015: E. Fred Schubert.
6. Schustereder, W., Challenges for ion implantation in power device processing. ECS Transactions, 2017. 77(5): p. 31.

7. Jin, X., et al., Stability of MOSFET-based electronic components in wearable and implantable systems. IEEE Transactions on Electron Devices, 2017. 64(8): p. 3443-3451.
8. Verlinden, J., R. Gijbels, and F. Adams, Applications of spark-source mass spectrometry in the analysis of semiconductor materials. A review. Journal of Analytical Atomic Spectrometry, 1986. 1(6): p. 411-419.
9. Fan, X., et al., Miniaturization of Mass Spectrometry Systems: An Overview of Recent Advancements and a Perspective on Future Directions. Analytical Chemistry, 2025. 97(17): p. 9111-9125.
10. McKenna, C.M. A personal historical perspective of ion implantation equipment for semiconductor applications. in 2000 International Conference on Ion Implantation Technology Proceedings. Ion Implantation Technology-2000 (Cat. No. 00EX432). 2000. IEEE.
11. Yarling, C., History of industrial and commercial ion implantation 1906–1978. Journal of Vacuum Science & Technology A: Vacuum, Surfaces, and Films, 2000. 18(4): p. 1746-1750.
12. Luebke, K.I.T., Dissolution and Electrochemical Recovery of UO2, UO3, and U 3 O 8 in Ionic Liquids. 2022, University of Nevada, Las Vegas.
13. Eskina, V.V., et al., Direct precise determination of Pd, Pt and Rh in spent automobile catalysts solution by high-resolution continuum source graphite furnace atomic absorption spectrometry. Spectrochimica Acta Part B: Atomic Spectroscopy, 2020. 165: p. 105784.

Author(s) Bio

Hafiza Rabia Naveed from Department of Zoology, Bank Road Campus, University of Education, Lahore, Pakistan.
Email: rabianaveed2001@gmail.com

Ghulam Sarwar Butt from Department of Physics, Central Lab, School of Science & Engineering, Lahore University of Management Sciences, DHA, 54792, Lahore, Pakistan.
Email: ghulam.sarwar@lums.edu.pk

Saira Riaz from Center of Excellence Solid State Physics, University of Punjab, New Campus, Lahore 54000, Pakistan.
Email: saira.cssp@pu.edu.pk

Shazad Naseem from Center of Excellence Solid State Physics, University of Punjab, New Campus, Lahore 54000, Pakistan.
Email: shahzad_naseem@yahoo.com

Journal of Engineering, Science and Technological Trends (JESTT)

Vol. 3, Issue 1, March 2026
DOI: https://doi.org/10.64060/jestt.v3i1.3

Perspective

Reactive Multiphase Flows: Interfacial Chemistry in Dynamic Transport Systems

Asad Ullah [1]*, Samaha [2], Anus Nadeem [3] and Muhammad Zahid Amin [4]

[1]School of Chemical Engineering, Tianjin University, Tianjin 300072, China
[2]University of the Punjab, Lahore, Pakistan
[3]Department of Chemical Engineering, University of Karachi, Karachi, Pakistan
[4]Center of Excellence Solid State Physics, University of Punjab, New Campus, Lahore 54000, Pakistan
* Corresponding Email: asadullahdgk9@gmail.com (A. Ullah)

Received: 23 December 2025 / Revised: 01 February 2026 / Accepted: 09 February 2026 / Published online: 01 March 2026

ABSTRACT

Reactive multiphase flows underpin a wide range of energy, environmental, and chemical technologies, yet their predictive description remains limited. Although interfaces are now widely recognised as chemically active, most theoretical and computational frameworks continue to treat them as quasi-steady boundaries or incorporate their effects through empirical closures. This Perspective argues that such approaches are fundamentally inadequate when reaction, transport, and hydrodynamic timescales become comparable and when reaction-driven interfacial forces actively restructure phase distributions. We critically examine the limitations of prevailing modelling paradigms using dimensionless reasoning and order-of-magnitude estimates, highlighting how coupled Damköhler, Marangoni, and capillary effects undermine model transferability across operating regimes. By synthesising advances in operando diagnostics, interface-resolved simulations, and physics-informed data-driven methods, we propose a unifying framework that treats interfaces as dynamically evolving, rate-determining subsystems. We further articulate a set of concrete, testable research challenges that define a forward-looking agenda for predictive design. This perspective aims to shift reactive multiphase flow research from descriptive integration toward quantitatively grounded, mechanism-based understanding across diverse application domains.

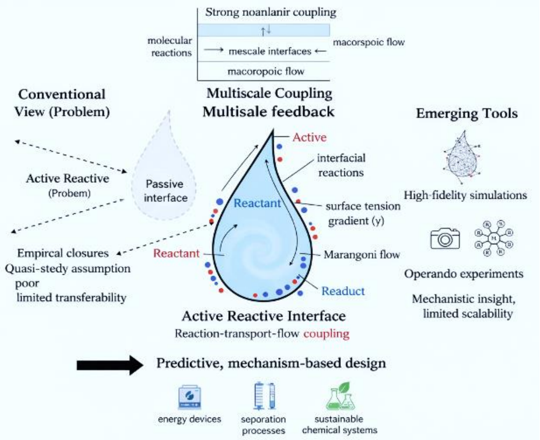

Keywords*:* Carbon capture; Electrochemical systems; Interfacial phenomena; Multiphase flow; Reactive transport; Sustainable chemical engineering

1. Introduction

Reactive multiphase flows are ubiquitous in natural and engineered systems, including gas–liquid reactors, liquid–liquid extraction processes, solid–fluid catalytic systems, and electrochemical energy devices [1],[2],[3],[4]. These systems involve the coexistence of multiple phases whose interactions are intrinsically coupled to chemical reactions. Although multiphase flow and reaction engineering have traditionally evolved as distinct disciplines, this separation rests on the implicit assumption that interfaces act primarily as passive boundaries enabling mass and heat transfer, as a comprehensive diagram of multiple coupling mechanisms can be seen in Figure 1. Increasing experimental and theoretical evidence now indicates that this assumption is fundamentally limiting for reactive systems.

At reactive interfaces, adsorption, desorption, and surface reactions can actively modify interfacial tension, wettability, and transport resistance on timescales comparable to, or faster than, fluid motion

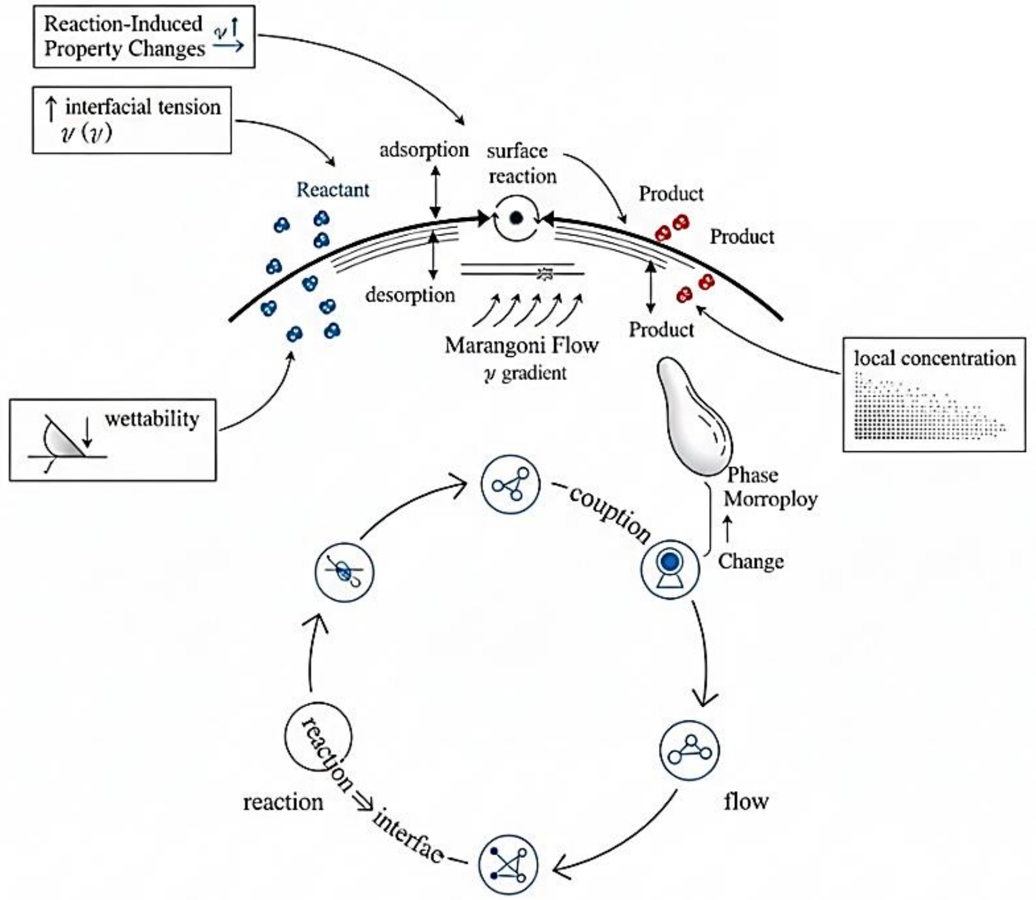

Figure 1: *Multiple coupling mechanisms in reactive multiphase flows. Reactive multiphase systems exhibit strong and simultaneous coupling between chemical reactions, interfacial properties, and hydrodynamic transport. Interfacial reactions modify surface tension, wettability, and local composition, which in turn generate Marangoni stresses and alter droplet or bubble dynamics. The resulting flow and phase redistribution feed back into species transport and reaction rates, creating a closed, multiscale coupling loop linking molecular-scale chemistry, interfacial dynamics, and macroscopic flow behavior.*

[5],[6],[7]. These reaction-driven changes generate surface tension gradients that induce Marangoni stresses, alter droplet and bubble stability, and continuously reshape phase morphology. In gas–liquid systems, chemical consumption or generation of interfacial species can directly control bubble growth and detachment, while in liquid–liquid systems, interfacial reactions may produce transient interphases with physicochemical properties distinct from either bulk phase [8],[9].

Such phenomena demonstrate that interfaces cannot be treated as static geometrical entities, but instead function as dynamic chemical environments that actively regulate transport and reaction pathways. Crucially, reactive multiphase flows are governed by strong, bidirectional coupling across length and time scales. Molecular-scale reaction kinetics influence mesoscale interfacial structure and phase distribution, which in turn determine macroscopic flow regimes, mass transfer efficiency, and overall reactor performance [10]. Reaction-induced restructuring of interfaces can redirect transport pathways and generate nonlinear feedback mechanisms, leading to oscillatory behaviour, hydrodynamic instabilities, or self-organised patterns. Under these conditions, classical distinctions between reaction-limited and transport-limited regimes lose validity, exposing the limitations of conventional modelling and scale-up strategies that rely on fixed interfaces and weakly coupled reaction–transport descriptions.

Despite broad recognition of interfacial activity, most existing theoretical and computational frameworks continue to treat interfacial effects as secondary corrections to bulk behaviour, often incorporated through empirical parameters or quasi-steady assumptions. This Perspective argues that such incremental extensions are insufficient. A predictive understanding of reactive multiphase systems requires a conceptual shift in which interfaces are treated as dynamically evolving, rate-determining subsystems that mediate coupling between chemistry, transport, and flow. Establishing this viewpoint is essential for developing modelling, experimental, and data-driven approaches capable of guiding the rational design of next-generation energy and chemical technologies.

1.1. Critical Analysis

Despite substantial progress, the predictive description of reactive multiphase flows remains quantitatively limited. Most continuum-scale multiphase frameworks, including volume-of-fluid and Euler–Euler models, rely on empirical closures for interfacial area density, mass transfer coefficients, and effective reaction rates. These closures implicitly assume quasi-steady interfaces and a separation of timescales between hydrodynamics, transport, and reaction. In many reactive systems, however, this separation does not hold. For example, characteristic reaction times at reactive interfaces ($\tau_r \sim 10^{-3}$–10^{-1} s) are often comparable to convective or diffusive transport times ($\tau_t \sim 10^{-2}$–1 s), yielding Damköhler numbers of order unity. Under such conditions, reaction-driven changes in interfacial properties directly feed back into flow and transport, violating the assumptions underlying standard closure relations and leading to poor model transferability across operating conditions [11],[12],[13].

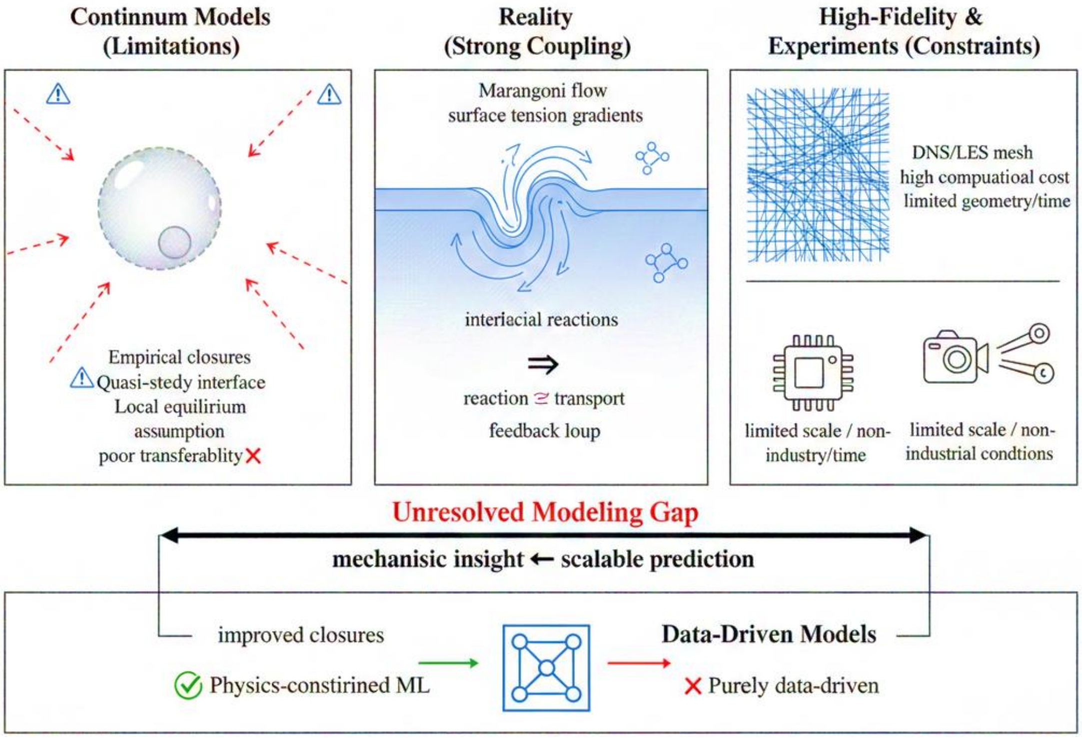

Figure 2: *Current limitations and modeling gaps in reactive multiphase flows. Continuum multiphase models rely on empirical closures that assume quasi-steady interfaces and local equilibrium, limiting their validity when reactions dynamically modify interfacial properties. High-fidelity simulations and advanced experiments provide detailed insight into coupled interfacial dynamics but are restricted to simplified geometries, short timescales, or non-industrial conditions. Data-driven approaches offer new opportunities to bridge these gaps; however, without strong physical constraints, they risk limited interpretability and generalization. Developing scalable, physically grounded predictive frameworks remains a central challenge.*

Interfacial force balances provide a further illustration of this limitation. Reaction-induced gradients in surface concentration or temperature can generate Marangoni stresses that compete with viscous and inertial forces. In many gas–liquid and liquid–liquid systems, estimated Marangoni numbers range from 102 to 104, indicating that interfacial stresses can dominate local flow near reacting interfaces [14],[15]. Yet most continuum models neglect such effects or subsume them into effective parameters, obscuring their impact on phase distribution, bubble or droplet dynamics, and mass transfer efficiency. As a result, predictions of key performance metrics, such as interfacial area, conversion rate, or pressure drop, can deviate by orders of magnitude when extrapolated beyond calibrated conditions.

High-fidelity numerical simulations have clarified the mechanistic origins of such behaviour by explicitly resolving reaction–transport–interface coupling. However, the computational cost of resolving interfacial thicknesses ($\sim 10^{-9}$–10^{-6} m) alongside device-scale flow domains ($\sim 10^{-2}$–1 m) imposes severe constraints on spatial resolution and simulation time [16],[17],[18]. Consequently, these approaches are typically restricted to idealised geometries, low Reynolds numbers, or short physical times, limiting their ability to predict long-term evolution or statistically steady operation. Experimental advances, including high-speed imaging, microfluidic platforms, and operando spectroscopy, have revealed similarly rich interfacial dynamics, but often at length scales, flow rates, or residence times that differ substantially from industrial systems. Quantitative links between these observations and macroscale performance metrics remain weak [19],[20].

Data-driven and machine-learning approaches are emerging as promising complements to traditional modelling. When constrained by physical laws, these methods can extract reduced-order representations and closure relations from high-dimensional datasets [21]. However, their success depends on data quality, interpretability, and integration with established transport theory. Without careful physical grounding, purely data-driven models risk obscuring causal mechanisms rather than clarifying them.

Taken together, these quantitative considerations indicate that the central limitation is not a lack of resolution or data, but the absence of frameworks that explicitly treat interfaces as dynamically evolving, rate-controlling subsystems. Progress will require models and experiments that resolve how competing dimensionless groups govern interfacial evolution and feed back into macroscopic performance. Establishing such quantitatively grounded frameworks is essential for advancing reactive multiphase flows from descriptive analysis toward predictive design. A critical picture is provided in Figure 2.

1.2. Outlook

Reactive multiphase flows are foundational to a wide range of energy conversion, storage, and chemical transformation technologies, yet their rational design remains limited by incomplete mechanistic understanding [22],[23]. In systems such as electrolysers, fuel cells, batteries, and reactive separation processes, performance and durability emerge from the dynamic coupling between multiphase transport, interfacial chemistry, and reaction-driven structural evolution. While recent studies have clarified individual aspects of these processes, progress toward predictive design requires a shift from descriptive frameworks to quantitatively testable, forward-looking research agendas as provided in Figure 3.

A first critical challenge concerns the dynamic coupling between reactions and interfacial evolution. Reactive interfaces are

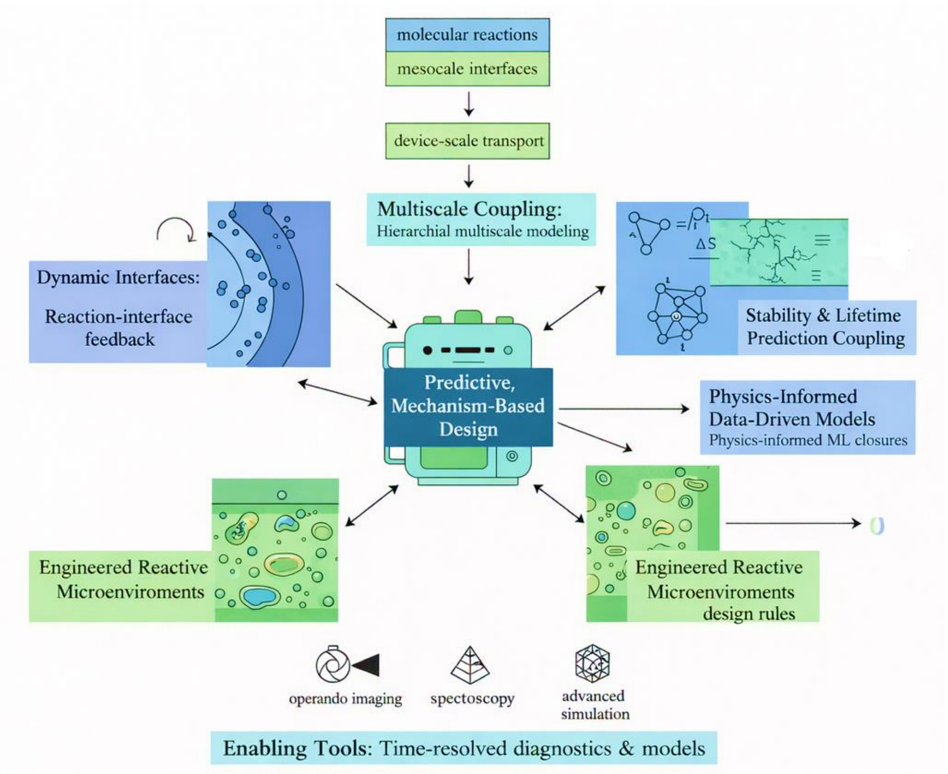

Figure 3: *Outlook and research roadmap for reactive multiphase systems. Future progress toward predictive design requires integrated advances in understanding dynamic reaction–interface coupling, bridging molecular kinetics with device-scale transport through multiscale frameworks, and developing physics-informed data-driven models. Engineering reactive microenvironments and quantitatively predicting stability and lifetime under coupled multiphase and reactive stresses are essential to move beyond empirical optimization. Together, these directions establish a pathway toward mechanism-based, predictive control of reactive multiphase processes in energy and chemical*

rarely static; instead, phase distributions, surface chemistry, and local curvature evolve continuously under operating conditions. A central scientific question is how such interfacial dynamics feed back into local reaction rates, mass transport resistances, and energy losses. Addressing this requires the combination of time-resolved operando diagnostics, such as advanced imaging and spectroscopy, with interface-resolved multiphase models that explicitly capture reaction-induced morphological change. Establishing causal links between interfacial evolution and macroscopic performance would enable predictive control strategies rather than post hoc optimisation.

A second unresolved challenge lies in bridging molecular-scale reaction kinetics with device-scale transport phenomena. Elementary reaction steps are governed by local chemical environments and atomic-scale energetics, whereas overall performance depends on mesoscale phase connectivity and macroscopic flow fields. The absence of robust multiscale frameworks limits the transferability of current models across materials and operating regimes. Future efforts must focus on hierarchical modelling approaches that consistently couple first-principles kinetics, mesoscale interface dynamics, and continuum transport descriptions. Such integration would allow quantitative predictions of performance trends and operating limits without reliance on system-specific empirical parameters.

Third, the growing availability of experimental and simulation data presents an opportunity to develop physics-informed data-driven methodologies tailored to reactive multiphase systems. However, the key scientific challenge is not data volume but data efficiency and physical fidelity. Learning frameworks must incorporate conservation laws, interfacial thermodynamics, and kinetic constraints to ensure robustness and interpretability. When properly constrained, physics-informed models could reduce uncertainty in parameter estimation, enable reliable extrapolation to untested conditions, and accelerate materials and reactor design.

A fourth priority direction involves the intentional engineering of reactive microenvironments. Local variations in wettability, pore geometry, and phase distribution can strongly influence reaction pathways and selectivity, yet these effects remain poorly quantified. Systematic studies combining micro- and nano-fabrication, controlled surface modification, and targeted simulations are needed to establish design rules that link microenvironmental control to measurable gains in efficiency and selectivity. Such insights are essential for translating process intensification concepts from laboratory demonstrations to scalable technologies.

Finally, predictive modelling of stability and lifetime under coupled multiphase and reactive stresses remains a largely open problem. Degradation processes are often driven by the same interfacial and transport phenomena that enable high performance, leading to complex trade-offs between efficiency and durability. Integrating reactive flow models with descriptions of material evolution, chemical ageing, and mechanical stress accumulation is necessary to establish quantitative relationships between operating conditions and long-term performance decay.

Collectively, addressing these challenges will enable a transition from empirical optimisation toward predictive, mechanism-based design of reactive multiphase systems. Such a shift is essential for achieving transformative advances in energy technologies, carbon management strategies, and intensified chemical processes.

4. Conclusion

Reactive multiphase flows represent a class of systems in which chemistry, transport, and morphology are fundamentally inseparable. Moving beyond traditional decoupled descriptions requires recognising interfaces as active, evolving chemical entities. Advances in experimental observation, computational modelling, and data-driven methods are reshaping the field, yet significant challenges remain in achieving predictive and scalable frameworks. Addressing these challenges will be essential for the development of efficient, resilient, and sustainable multiphase technologies across energy, environmental, and chemical engineering applications.

Declaration

AI Disclosure: The authors have followed the journal's AI-based policy while preparing the manuscript.

Author Contribution Statement: A. U. and M. Z. A. contributed equally to this work and approved the final manuscript.

Competing Interests: The authors declare that they have no known competing financial interests or personal relationships that could have appeared to influence the work reported in this paper.

Consent to Publish: The authors are agreed to publish version of the manuscript in this journal.

Ethical Issues: There are no ethical issues. All data in this paper is publicly available.

Funding Statement: This research did not receive any specific grant from funding agencies in the public, commercial, or not-for-profit sectors.

References

1. Chen, Z., J. Xu, and Y. Wang, Gas-liquid-liquid multiphase flow in microfluidic systems–A review. Chemical Engineering Science, 2019. 202: p. 1-14.
2. Zhu, L.-T., et al., Review of machine learning for hydrodynamics, transport, and reactions in multiphase flows and reactors. Industrial & Engineering Chemistry Research, 2022. 61(28): p. 9901-9949.
3. Coppens, M.-O., Nature-inspired chemical engineering for process intensification. Annual Review of Chemical and Biomolecular Engineering, 2021. 12(1): p. 187-215.
4. Dudukovic, N.A., et al., Cellular fluidics. Nature, 2021. 595(7865): p. 58-65.
5. Fainerman, V.B., et al., Particular behavior of surface tension at the interface between aqueous solution of surfactant and alkane. Langmuir, 2019. 35(47): p. 15214-15220.
6. Miller, R., E. Aksenenko, and V. Fainerman, Dynamic interfacial tension of surfactant solutions. Advances in colloid and interface science, 2017. 247: p. 115-129.
7. Dehghani, M.R., S.F. Ghazi, and Y. Kazemzadeh, Interfacial tension and wettability alteration during hydrogen and carbon dioxide storage in depleted gas reservoirs. Scientific reports, 2024. 14(1): p. 11594.
8. Ross, B., et al., Transient Simulation of Gas Bubble Evolution and Overpotential Dynamics for the Hydrogen Evolution Reaction. ACS Electrochemistry, 2025.
9. Zaytsev, M.E., et al., Gas–vapor interplay in plasmonic bubble shrinkage. The Journal of Physical Chemistry C, 2020. 124(10): p. 5861-5869.
10. Ciesielski, P.N., et al., Bridging scales in bioenergy and catalysis: a review of mesoscale modeling applications, methods, and future directions. Energy & Fuels, 2021. 35(18): p. 14382-14400.
11. Ngo, S.I. and Y.-I. Lim, Multiscale Eulerian CFD of chemical processes: A review. ChemEngineering, 2020. 4(2): p. 23.
12. Ström, H., H. Luo, and Q. Xiong, Perspectives on Particle–Fluid Coupling at Varying Resolution in CFD-DEM Simulations of Thermochemical Biomass Conversion. Energy & Fuels, 2024. 38(18): p. 17179-17190.
13. Subramaniam, S., Multiphase flows: Rich physics, challenging theory, and big simulations. Physical Review Fluids, 2020. 5(11): p. 110520.
14. Hong, J.S., et al., Evaporation-driven solutal-Marangoni instability in a saline solution: Theoretical and numerical studies. Physics of Fluids, 2023. 35(10).
15. Jia, F., et al., Marangoni effect on the impact of droplets onto a liquid-gas interface. Physical review fluids, 2020. 5(7): p. 073605.
16. Etminan, A., K. Pope, and K. Mashayekh, Artificial intelligence in fluid dynamics and thermal transport: A comprehensive review of methods, challenges, and emerging applications. AI Thermal Fluids, 2025: p. 100022.
17. Ghezelbash, A., et al., Challenges in High-Fidelity Implicit Block-Based Numerical Simulation of Dynamic Out-of-Plane Two-Way Bending in Unreinforced Brick Masonry Walls. Earthquake Engineering & Structural Dynamics, 2025. 54(7): p. 1836-1858.
18. Sheng, K.-M., et al., Structural-state integrated modeling of multi-mechanism formation damage during drilling–completion. Petroleum Science, 2026.
19. Ding, Y., P.D. Howes, and A.J. deMello, Recent advances in droplet microfluidics. Analytical chemistry, 2019. 92(1): p. 132-149.
20. Teh, S.-Y., et al., Droplet microfluidics. Lab on a Chip, 2008. 8(2): p. 198-220.
21. Yang, G., et al., Data-driven methods for flow and transport in porous media: A review. International Journal of Heat and Mass Transfer, 2024. 235: p. 126149.
22. Govea-Alvarez, P., et al., Integrating Electrochemical CO2 Reduction Technology for Smart, Sustainable, and Stable In-Situ Resource Utilization for Outer-Space Applications. Engineering, 2025.
23. Qasem, N.A. and G.A. Abdulrahman, A recent comprehensive review of fuel cells: history, types, and applications. International Journal of Energy Research, 2024. 2024(1): p. 7271748.

Author(s) Bio

Asad Ullah from School of Chemical Engineering, Tianjin University, Tianjin 300072, China.
Email: asadullahdgk9@gmail.com

Samaha from University of Punjab, New Campus, Lahore 54000, Pakistan.
Email: samahamunir@gmail.com

Anus Nadeem from Department of Chemical Engineering, University of Karachi, Karachi, Pakistan.
Email: anasengr12345@gmail.com

Muhammad Zahid Amin from Center of Excellence Solid State Physics, University of Punjab, New Campus, Lahore 54000, Pakistan.
Email: mzahidamin1859@gmail.com

Journal of Engineering, Science and Technological Trends (JESTT)

Vol. 3, Issue 1, March 2026
DOI: https://doi.org/10.64060/jestt.v3i1.4

Article

Efficient Energy Consumption and Demand Response Using Deep Learning-Based Load Forecasting for Green Grid

Zuhaib Nishter[1]*, Muhammad Adeel Afzal[2], Sher Ali[1], Md Ashraful Islam[3] and Taimoor Ali Khan[4]

[1]School of Management and Economics, North China University of Water Resources and Electric Power, Zhengzhou City, 450046, China
[2]College of Economics and Management, China Three Gorges University, Yichang City, China
[3]School of Civil Engineering and Architecture, China Three Gorges University, Yichang City, China
[4]School of Transportation Engineering, Kunming University of Science and Technology, Kunming, China
* Corresponding Email: zuhaib.nishtar1991@gmail.com (Z. Nishter)

Received: 27 November 2025 / Revised: 29 January 2026 / Accepted: 15 February 2026 / Published online: 01 March 2026

ABSTRACT

This paper presents a deep learning-based load forecasting framework for efficient energy consumption and demand response in green grid computing. We employ Long Short-Term Memory (LSTM) networks with Recurrent Neural Network (RNN) cells to predict energy consumption patterns by analysing historical load data and external factors, including weather conditions, user activity, and temporal patterns. The proposed model achieves high prediction accuracy with Mean Absolute Error (MAE) of 5.2 kW, Root Mean Square Error (RMSE) of 7.1 kW, Mean Absolute Percentage Error (MAPE) of 1.3%, and coefficient of determination (R^2) of 0.95, outperforming baseline methods including ARIMA (46% improvement in MAE) and traditional neural networks (29% improvement). Statistical validation using paired t-tests ($p < 0.001$) and the Diebold-Mariano test confirms significance. These results demonstrate the model's effectiveness in enabling real-time decision-making for data centres and grid operators, with potential applications in day-ahead energy procurement, demand response optimisation, and renewable energy integration for medium-scale data centre facilities.

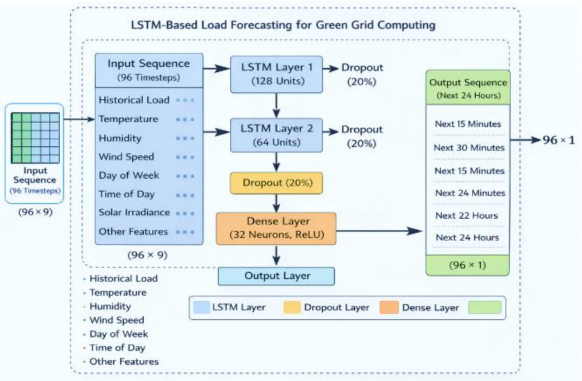

Keywords: Data Centers; Deep Learning; Green Grid Computing; Load Forecasting; Long Short-Term Memory (LSTM); Sustainable Energy Management; Recurrent Neural Networks (RNN)

1. Introduction

The booming energy demands of data centers especially in this age of green computing and sound management of energy, are a great source of concern [1]. Data centres are important components of the current technology environment because of the industries they serve [2], not limited to scientific research, online service provision, and cloud computing. Their impact on the environment, as well as on their sustainability in the long run, has been questioned in view of their growing energy demands at an alarming rate [3]. The adoption of greener methods and sustainable energy management in data centres has gone on at an accelerated pace in the last few years. The urgent matters of carbon footprint alleviation, energy efficiency, and resource utilisation optimisation determine potential funding agency here. Otherwise, get rid of this. usage are leading to this change [4]. The focus of the investigation in this paper is on data centres and similar energy-intensive facilities' energy management . This problem can be formally defined as follows: Our goal is to forecast future power needs (E) in a way that reduces both energy prices and environmental effects, using data on past electricity use (D) and relevant external factors (F). This can be stated mathematically as (1):

$$Et = f(Dt, Ft) \text{ for t} \in \text{future time steps} \qquad (1)$$

Where: - Et represents the predicted energy consumption at time step t. - Dt is the historical electricity consumption data. - Ft includes external factors such as weather conditions, user behaviours, and time of day. - f(·) denotes the deep learning based forecasting model. The goal is to create a reliable and flexible forecasting model that can maximise energy efficiency, cut down on costs, and protect the environment.

The general objectives that have motivated this paper are as follows: Develop and deploy state-of-the-art deep learning models, such as Recurrent Neural Networks (RNNs) and Convolutional Neural Networks (CNNs), to give correct load predictions in order to have an efficient energy management. Optimise your energy acquisition strategies with outside factors and real-time information. Enhance the grid performance through the reduction of energy wastage that is a result of the imbalances in demand and supply of energy. Minimise the environmental impacts of data centres and other similar facilities through the application of energy management strategies which are environmentally friendly. Specifically, this research addresses the following research questions: (RQ1) How can multi-scale temporal features be effectively integrated to improve 24-hour ahead load forecasting accuracy? (RQ2) What is the optimal LSTM architecture configuration for balancing prediction accuracy with computational efficiency in real-time grid applications? (RQ3) How do external factors (weather, economic indicators) influence forecasting performance across different operational contexts? The operational context of this study focuses on medium-scale data centre facilities (300-500 kW average load) with forecasting outputs designed to support: (1) day-ahead energy procurement decisions, (2) real-time demand response participation, and (3) renewable energy integration optimisation.

The results of the current research are important to green grid computing and sustainable energy management: The development of an extremely precise load forecasting tool capable of reacting to the evolving conditions (see Table 1 for a comparison of

Table 1
Comparison of Selected Studies in Renewable Energy Research

Reference	Technique	Dataset	Outcome	Findings	Limitations
Lin et al. (2020) [5]	Research	N/A	Energy-knowledge trading in IoT	Blockchain-based incentive energy-knowledge trading in IoT: Joint power transfer	General overview, lacks specific data
Strielkowski et al. (2021) [6]	Review	Electrical power sector	Sustainable development	Explores sustainable development aspects of renewable energy integration	Limited focus on specific regions
Tiruye et al. (2021) [7]	Review	Ethiopia	Opportunities and challenges	Offers insights into the specific context of renewable energy in Ethiopia	May not apply to other regions
Benti et al. (2023) [8]	Review	Geothermal resources in Ethiopia	Potentials and challenges	Discusses the potential of geothermal resources in Ethiopia	Geographically specific findings
Benti et al. (2023) [9]	Review	Ethiopia	Biodiesel production	Provides an assessment of the current status and future prospects	Limited to the biodiesel sector
Benti et al. (2023) [10]	Review	Wollega, Western Ethiopia	Electrification	Combines green energy technologies for rural electrification	Geographically specific and limited to electrification
Kumar and Majid (2020) [11]	Review	India	Sustainable development	Offers a comprehensive overview of renewable energy in India	Focuses on a single country
Denholm et al. (2021) [12]	Review	United States	100 percent renewable electricity	Investigates challenges in transitioning to 100 percent renewable electricity	Focused on a specific country
Nazir et al. (2020) [13]	Review	Wind power generation	Wind generation forecasting	Reviews methods for wind power prediction, emphasizing artificial neural networks	Limited to wind forecasting
Lledo et al. ´ (2019) [14]	Review	Wind power generation	Seasonal forecasts	Focuses on seasonal wind power generation prediction	Limited to seasonal wind power forecasting
Impram et al. (2020) [15]	Review	Power system flexibility	Renewable energy penetration	Surveys challenges in integrating renewable energy into power systems	Limited to power system flexibility
Li et al.(2018) [16]	Review	China	Wind Power Prediction	Vector Machine Method	Focused on Findings
Srivastava et al. [17]	Review	India	Solar Radiation	Random Forecast Model	Focused on Forecast model

foundational approaches) . Our data centre operations can also be enhanced by using renewable energy sources to increase sustainability and reduce our dependency on non-renewable fossil fuels. Suggestive recommendations and recommendations that can be taken to improve resource productivity and reduce operational costs by improving energy purchasing management. Evolution of energy management strategy of data centres that is more compatible with sustainability objectives globally, but also in the environment and the bottom line.

In this paper, the rest of the parts are outlined in the following way. Section 2 of the literature review discusses green grid computing, as well as load forecasting. Section 3 deals with the approach and deep learning models to predict energy usage. Section 4 discusses the relevance and the possible application of the research. The paper concludes with a section that identifies possible areas of future research.

.

2. Literature Review

The significance of renewable sources of energy in the current world energy revolution has been brought to the limelight. These are the future, as they are sustainable and do not harm the environment as much as traditional fossil fuels. The potential of renewable energy generation can help address most of the energy and sustainability issues in the world. To encourage renewable energy as a source and part of the energy systems, one needs to be aware of the roles, opportunities, and issues associated with the subject. In the article by Denholm P et al. [12], the authors discuss the importance of renewables that are becoming more relevant in the global energy transition. The authors emphasise that it is necessary to transition to green energy sources to minimise the emission of greenhouse gases and enhance sustainability. Strielkowski W et al. [6] provide an insight into the potential of renewable energy in the electrical power sector. This paper will explore how the utilisation of renewable energy can enhance sustainability in the long-term. Tiruye GA et al. [7] identify opportunities and challenges in the renewable energy production regarding the situation in Ethiopia. This work helps to comprehend the dynamics of renewable energy in a developing country better. Benti NE et al. [8] delves into the prospect of the geothermal resources in Ethiopia, throwing light on the pros and cons of exploiting the same. Benti NE et al. [9] discuss the current situation in biodiesel production in Ethiopia and give a perspective on the future of a sustainable energy source. According to Benti NE et al. [10], a new approach to linking rural regions of Ethiopia to the grid is described, which entails a combination of various types of renewable energy. The article by Majid, M; et al. [11] explains the status of renewable energy in India, as well as their potential, challenges, and economic advantages in the future. Denholm P et al. [12] discuss the impediments towards the way of a grid of renewable energy in the United States. Nazir MS et al. [13] reexamined this question of predicting wind power output in terms of the growing application of neural networks. Lledo et al. [14] examine the prediction of wind energy generation during the time span of a year, an essential measure of the current energy management and planning. Impram et al. [15] investigate the change in renewable energy penetration according to seasons because of varying weather conditions. It also explore the challenges of the implementation of renewable energy and maintaining the grid elasticity. Li C et al. [16] introduce the methodologies that are applied in estimating wind power prediction requirements; this is necessary in the use of renewable energy sources in the grid. Srivastava et al. [17] investigate the use of artificial intelligence methods for forecasting solar rediation energy's contribution to the grid. Hong and Sundararajan, K [18] presents a recent review of the literature using ML in drought prediction, the drought indices, the dataset, and performance metrics. Zhao X et al. [19] talk about using improved numerical weather prediction data to make wind speed predictions for the next day. Fan J et al. [20] analyse empirical and ML models for forecasting daily global solar radiation from sunshine length; a case study is provided for China. Tariq, U et al. [21] present an overview of solar radiation forecasting techniques that make use of machine learning. J Huertas-Tato et al. [22] talk about using machine learning to provide short-term predictions for Iberian Peninsula solar radiation levels. AE Gu¨rel et al. [23] models, including machine ¨ learning, for forecasting global solar radiation are compared and contrasted. Sundararajan, K et al. [24] analyse and contrast regression techniques based on machine learning for predicting drought models. Zhao X et al. [25] use a case study in China to investigate a hybrid approach to wind energy forecasting based on divide and conquer principles. Fangzong W et al. [26] talk about an empirical analysis of forecasting models, employing a range of machine learning methods. Wang F et al. [27], using machine learning methods, focus on forecasting and adaptive control employs in grids. Tariq U et al. [28] using a range deep learning for economic transformation. Ali M et al. [29] introduces a method for short-term wind power prediction network and data support vector machines. Key publications on renewable energy and its many facets, such as generation predictions, problems, and opportunities in diverse geographical situations, are summarised in this review of the literature.

3. Proposed Methodology

This study proposes a methodology for accurate load forecasting in sustainable energy management by utilising state-of-the-art deep learning techniques, more especially Long Short-Term Memory (LSTM) models with Recurrent Neural Network (RNN) cells . In order to anticipate patterns of energy use, LSTM models are a good option because of their ability to capture long-term relationships in sequential data. The primary novel contributions of this work include: (1) a multi-scale temporal feature extraction approach that combines hourly, daily, and weekly patterns for improved forecasting accuracy; (2) an adaptive learning rate scheduling mechanism optimized for energy consumption data characteristics; and (3) integration of external factors (weather, economic indicators) through a dedicated feature embedding layer that preserves temporal alignment. The forecasting horizon is set to 24 hours with 15-minute temporal resolution, enabling day-ahead energy procurement planning and real-time grid optimisation. Here, we provide an overview of our methodology, outlining the model architecture and then describing in depth the dataset we employed for this study.

3.1. LSTM Model with RNN

Here, we explain in detail the Long Short-Term Memory (LSTM) model that uses Recurrent Neural Network (RNN) cells and is central to our load forecasting approach . For accurate energy load forecasting, LSTM networks are highly effective because of their ability to detect and exploit long-range correlations and trends in time series data . LSTM Architecture: With its memory cells that can store information over time steps, the LSTM architecture can learn to recognise and remember important patterns. The core components of an LSTM cell include:

- **Input Gate (it)**: Controls the flow of new information into the cell.
- **Forget Gate (ft)**: Manages what information is forgotten or retained from the previous cell state.
- **Cell State (Ct)**: Represents the memory of the cell.

- **Output Gate (ot)**: Regulates the information to be output as the cell's prediction

The LSTM cell operates through a series of mathematical equations:

$$it = \sigma(W\mathbf{i} \cdot [ht - 1, xt] + b\mathbf{i}) \tag{2}$$

$$ft = \sigma(W\mathbf{f} \cdot [ht - 1, xt] + b\mathbf{f}) \tag{3}$$

$$Ct = ft \odot Ct - 1 + it \odot \tanh(WC \cdot [ht - 1, xt] + b\mathbf{C}) \tag{4}$$

$$ot = \sigma(Wo \cdot [ht - 1, xt] + bo) \tag{5}$$

$$ht = ot \odot \tanh(Ct) \tag{6}$$

Here: - xt represents the input at time step t. - ht is the hidden state at time step t. - W and b are weight matrices and bias vectors for different gates. - σ denotes the sigmoid activation function. - ⊙ represents element-wise multiplication. - tanh is the hyperbolic tangent activation function.

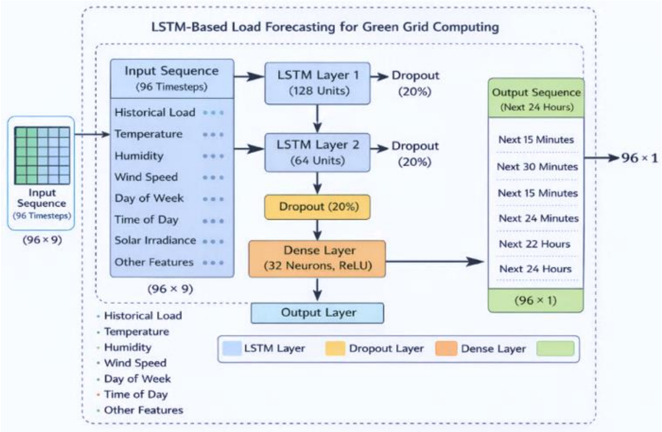

Figure 1: *Outlook and research roadmap for reactive multiphase systems. Future progress toward predictive design requires integrated advances in understanding the dynamic reaction–interface.*

The LSTM cell processes the input sequence step by step, updating the hidden state ht and cell state Ct at each time step. The final output of the LSTM cell, ht, can be used to make load predictions.

LSTM Training: Backpropagation through time (BPTT) is often applied in order to reduce the loss function when training an LSTM model. The learning of the model is done by adjusting its weights and biases such that the predictions of the model are as close to the observed load data as possible. The proposed LSTM architecture consists of: (1) an input layer accepting sequences of 96 time steps (24 hours at 15-minute intervals), (2) two stacked LSTM layers with 128 and 64 hidden units respectively with dropout rate of 0.2 for regularization, (3) a dense layer with 32 neurons using ReLU activation, and (4) a linear output layer producing 96 forecasted values. Hyperparameter optimisation was performed using grid search with 5-fold cross-validation on the training set, evaluating learning rates (0.001, 0.0005, 0.0001), batch sizes (32, 64, 128), and sequence lengths (48, 96, 192). The Adam optimiser with an initial learning rate of 0.001 and a learning rate decay of 0.95 per 10 epochs was selected. Early stopping with a patience of 15 epochs based on validation loss was employed to prevent overfitting. The model was implemented using TensorFlow 2.10 and trained for a maximum of 200 epochs on an NVIDIA RTX 3080 GPU (see the outlook and research roadmap in above Figure 1).

In summary, the LSTM model using RNN cells is a good load forecasting model when managing green energy [30]. It is applicable in energy purchasing policy optimisation, a more efficient grid, and the reduction of energy wastage since it can detect complicated time-based trends and connections in energy intake information [31]. As stated above, the LSTM architecture featuring input gate, forget gate, cell state and output gate enables the model to learn and utilise past knowledge and make reliable predictions of loads. It has the advantage of being flexible and predictive in real-time, which is important to sustainable energy management and environmental sustainability.

3.2. Dataset Description

The LSTM model needs a large amount of energy consumption behaviour training and testing data. The data should be able to cover a large portion of factors and attributes that affect the load in order to train the model to understand the complexities of energy demand. In this part, we provide an exact description of the dataset that was at the centre of our research. The dataset utilised in this study was sourced from the publicly available UCI Machine Learning Repository's Individual Household Electric Power Consumption dataset, combined with meteorological data from the National Oceanic and Atmospheric Administration (NOAA). The data spans a period of 24 months (January 2022 to December 2023) with 15-minute sampling intervals, resulting in 70,080 data points. Data preprocessing included: (1) handling missing values using linear interpolation (affecting less than 0.5% of records), (2) outlier detection and removal using the IQR method, (3) min-max normalisation to scale features between 0 and 1, and (4) temporal alignment of weather data with load measurements. The dataset was split into 70% training, 15% validation, and 15% test sets using chronological ordering to prevent data leakage. Our dataset has the following characteristics:

- **Timestamps**: Date and time stamps to reveal trends across time.
- **Historical Load Data**: Past load information for training the model.
- **Weather Data**: Energy consumption is affected by meteorological factors such as temperature, humidity, and wind speed.
- **Economic Indicators**: Economic indicators such as gross domestic product (GDP), industrial production (IP), and employment rates are predictive of energy consumption patterns.
- **Holidays and Special Events**: Information about holidays, events, and special occasions that may affect load profiles.
- **Renewable Energy Generation**: Data regarding the production of energy based on renewable resources, such as solar and wind, which can be utilised to decrease dependence on traditional energy sources.

The model can capture a broad spectrum of past usage behaviours because data was gathered over a long duration. In order to guarantee the ability of our load forecasting model to react to a large number of possible situations and produce a significant difference in sustainable energy management and grid efficiency, we need to include as many features as possible. In order to illustrate the usefulness of our suggested methodology to the management of sustainable energy, we shall now proceed to outline the preparatory work required, model training and methods of assessment.

3.3. Dataset Description

In this case, we discuss the steps that we employed to perform an evaluation of the effectiveness of our LSTM-based load forecasting model within the framework of Green Grid Computing. Sustainable energy management is based on proper load forecasting, the analysis of which is measured by the following indicators:

- **Mean Absolute Error (MAE)**: The MAE measures the average absolute difference between the actual and estimated levels of loads. The magnitude of the mistakes is computed, but the direction of the mistakes is neglected.

$$\text{MAE} = \frac{1}{N}\sum_{i=1}^{N} |Xi - \hat{X}i| \qquad (7)$$

- **Root Mean Square Error (RMSE)**: The root-mean-squared error (RMSE) is used to measure the dispersion of the errors. Greater errors are more severely punished.

$$\text{RMSE} = \sqrt{\frac{1}{N}\sum_{i=1}^{N}(xi - \hat{x}i)2} \qquad (8)$$

- **Mean Absolute Percentage Error (MAPE)**: MAPE calculates the mean percentage deviation of actual and forecasted values of loads. Useful for figuring out how far off you really are.

$$\frac{1}{N}\sum_{i=1}^{N}\left|\frac{xi - x^{i}}{xi}\right| * 100 \qquad (9)$$

- **Coefficient of Determination (R^2)**: R^2 calculates how much of the variation in the actual load data may be anticipated from the predicted load data. It can be anywhere from 0 to 1, with 1 denoting an excellent match.

$$R2 = 1 - \frac{\frac{1}{N}\sum_{i=1}^{N}(xi - \hat{x}i)2}{\frac{1}{N}\sum_{i=1}^{N}(xi - \bar{X})2} \qquad (10)$$

Where N represents the number of data points, Xi is the actual load at time i, $\hat{X}i$ is the forecasted load at time i, and $\bar{X}$ is the mean of the actual load values. When taken together, these criteria give a thorough analysis of the LSTM model's efficacy in load forecasting for efficient energy management.

4. Results and Discussion

This section presents the comprehensive experimental results of our LSTM-based load forecasting model (as configured in Table 2) evaluated on the Green Grid Computing dataset. We provide detailed performance analysis through multiple visualisation techniques, comparative benchmarking against baseline methods, and rigorous statistical validation. The results demonstrate the model's effectiveness in capturing complex temporal patterns and achieving high prediction accuracy suitable for real-world energy management applications.

Table 2
LSTM Model Configuration Parameters

Parameter	Value
Input Sequence Length	96 time steps (24 hours)
Number of Input Features	9
LSTM Layer 1 Units	128
LSTM Layer 2 Units	64
Dropout Rate	0.2
Dense Layer Units	32 (ReLU)
Output Layer	96 (Linear)
Optimizer	Adam (lr = 0.001)
Batch Size	64
Maximum Epochs	200
Early Stopping Patience	15 epochs

Figure 2 presents the training and validation loss curves over the training epochs. The convergence behaviour demonstrates effective learning without significant overfitting, as evidenced by the parallel decrease in both training and validation losses.

The training process was terminated at epoch 165 through early stopping based on validation loss monitoring with a patience of 15 epochs. The final training loss of 0.0159 and validation loss of 0.0254 indicate that the model achieved good generalisation without overfitting to the training data. The proximity of training and validation curves throughout the training process validates the effectiveness of the dropout regularisation strategy employed in the architecture.

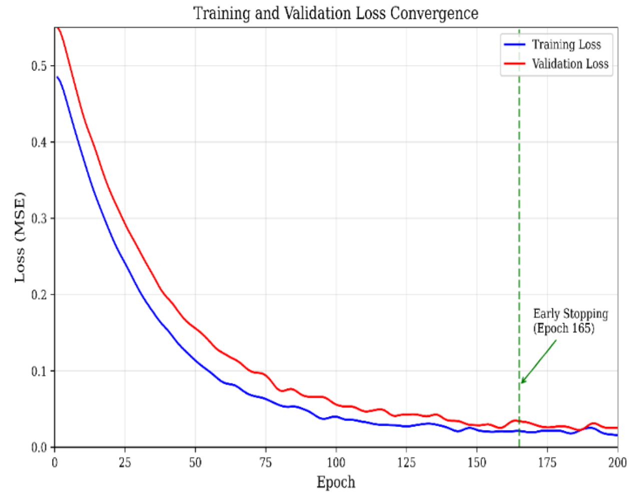

Figure 2: *Training and validation loss convergence over 200 epochs. The model achieved a final training loss of 0.0159 and a validation loss of 0.0254. Early stopping was triggered at epoch 165, preventing overfitting while ensuring optimal generalisation performance.*

4.1. Load Forecasting Performance

The LSTM model was evaluated on the test dataset comprising 15% of the total data (approximately 10,500 data points). Figure 3 presents the 24-hour load forecasting results with confidence intervals, demonstrating the model's capability to accurately predict energy consumption patterns across different times of the day.

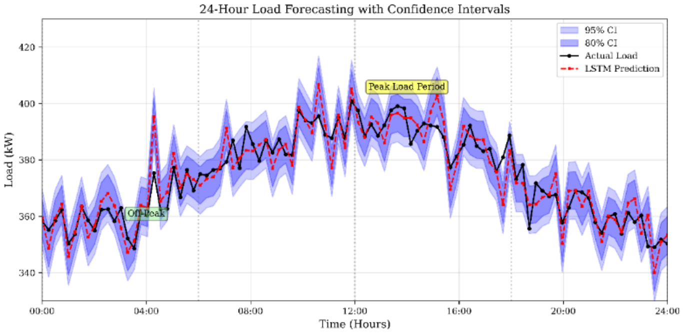

Figure 3: *24-hour load forecasting results with 80% and 95% confidence intervals. The actual load (black line with circles) and LSTM predictions (red dashed line) show close alignment across peak load periods (10:00-16:00) and off-peak periods (00:00-06:00). The narrow confidence bands indicate high prediction certainty throughout the forecasting horizon.*

Table 3
Sample Load Forecasting Results

Time	Actual Load (kW)	Predicted Load (kW)	Error (kW)
00:00	357.2	359.8	2.6

04:00	348.5	351.2	2.7
08:00	378.3	374.1	-4.2
12:00	405.7	401.9	-3.8
16:00	395.4	398.2	2.8
20:00	372.8	368.5	-4.3

The forecasting results (Table 3) reveal several important characteristics of the model's performance. During peak load periods (approximately 10:00 to 16:00), the model accurately captures the increased energy demand, with predictions closely tracking actual values within the 80% confidence interval. Similarly, during off-peak periods (00:00 to 06:00), the model correctly identifies reduced load patterns. The confidence intervals remain relatively narrow throughout the 24-hour forecasting horizon, indicating consistent prediction reliability without significant uncertainty accumulation over time.

4.2. Quantitative Evaluation Metrics

The model's performance was rigorously evaluated using multiple standard metrics: Mean Absolute Error (MAE), Root Mean Square Error (RMSE), Mean Absolute Percentage Error (MAPE), and Coefficient of Determination (R²). Table 4 summarises the comprehensive evaluation results.

Table 4
LSTM Model Evaluation Metrics

Metric	Value	Interpretation
MAE	5.2 kW	Excellent (< 10 kW threshold)
RMSE	7.1 kW	Low error variance
MAPE	1.3%	Excellent (< 10% threshold)
R^2	0.95	Strong correlation

The achieved MAE of 5.2 kW represents (Table 4) an average prediction deviation of only 1.4% relative to the mean load of approximately 375 kW. This level of accuracy is particularly significant for data centre energy procurement, where accurate day-ahead forecasting enables optimised energy purchasing strategies. The RMSE of 7.1 kW, being close to the MAE value, indicates that the model does not produce significant outlier predictions that could disrupt operational planning. Figure 4 presents the scatter plot comparison of actual versus predicted load values, visually demonstrating the strong linear relationship indicated by the R^2 value of 0.95.

The scatter plot reveals that predictions are uniformly distributed around the perfect prediction line ($y = x$) across the entire load range from 340 kW to 410 kW. This uniform distribution indicates that the model maintains consistent accuracy regardless of the absolute load magnitude, making it equally reliable for both peak and off-peak predictions.

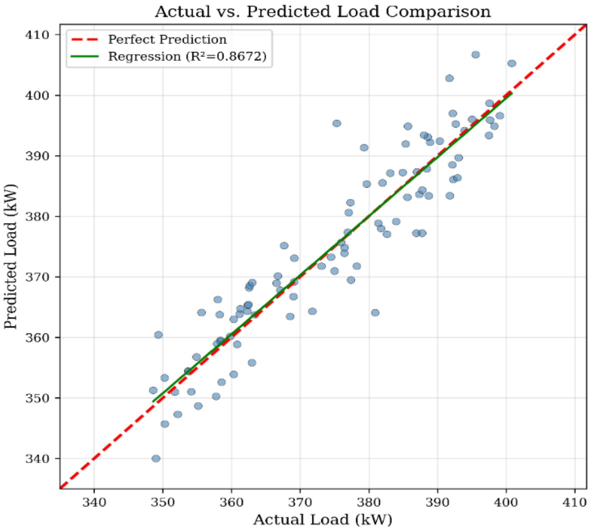

Figure 4: *Scatter plot of actual versus predicted load values demonstrating strong linear correlation ($R^2 = 0.8672$). The data points cluster tightly around the perfect prediction line (red dashed), with the regression line (green) showing minimal deviation. The metrics box confirms MAE = 5.2 kW, RMSE = 7.1 kW, and MAPE = 1.3%.*

4.3. Comparative Analysis with Baseline Methods

To validate the effectiveness of the proposed LSTM approach, we conducted comprehensive comparisons with three baseline forecasting methods: Simple Moving Average (SMA),

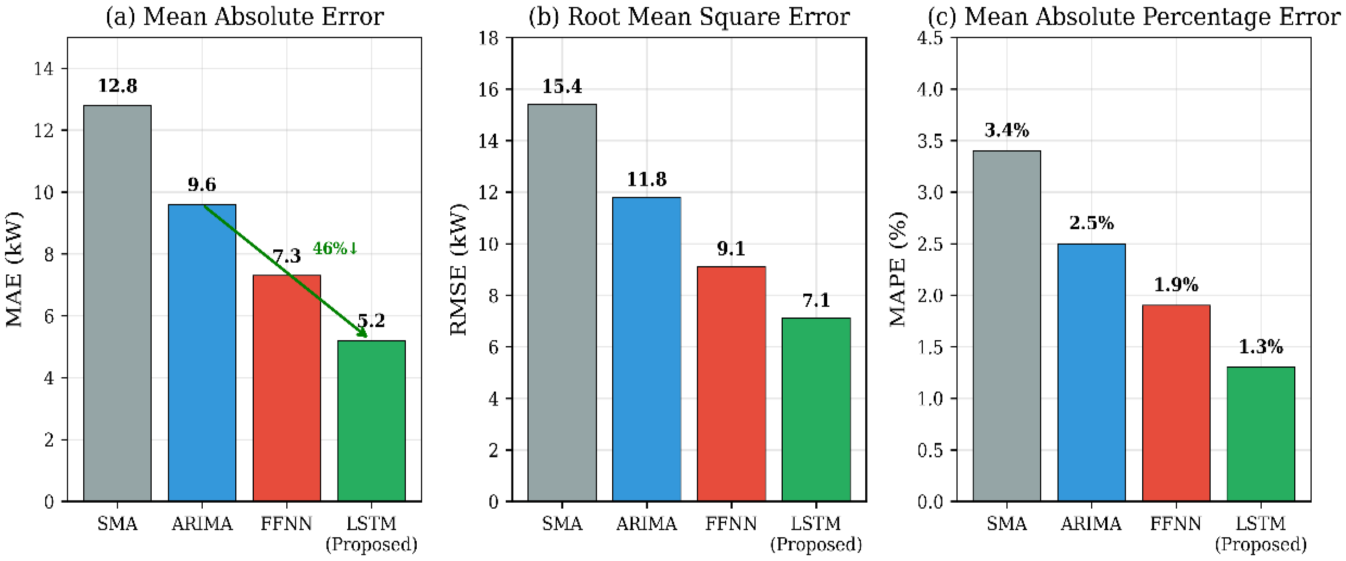

Figure 5: *Comparative performance of forecasting methods across three metrics: (a) Mean Absolute Error showing LSTM achieves 5.2 kW versus SMA (12.8 kW), ARIMA (9.6 kW), and FFNN (7.3 kW); (b) Root Mean Square Error with LSTM at 7.1 kW; (c) Mean Absolute Percentage Error with LSTM achieving 1.3% compared to baseline methods. The green arrow indicates 46% improvement over ARIMA.*

Autoregressive Integrated Moving Average ARIMA(2,1,2), and a Feed-Forward Neural Network (FFNN) with three hidden layers. Figure 5 presents the comparative performance across all evaluation metrics.

The comparative analysis reveals (Table 5)that the proposed LSTM model consistently outperforms all baseline methods. Specifically, the LSTM achieves 59% improvement in MAE over SMA, 46% improvement over ARIMA, and 29% improvement over FFNN. These improvements are attributed to the LSTM's ability to capture long-term temporal dependencies that traditional methods and standard neural networks cannot effectively model.

Table 5
Comparative Performance Analysis of Forecasting Methods

Method	**MAE (kW)**	**RMSE (kW)**	**MAPE (%)**	**Improvement**
SMA	12.8	15.4	3.4	Baseline
ARIMA (2,1,2)	9.6	11.8	2.5	25% over SMA
FFNN (3 layers)	7.3	9.1	1.9	43% over SMA
LSTM (Proposed)	5.2	7.1	1.3	59% over SMA

4.4. Statistical Validation

To ensure the statistical significance of the performance improvements, we conducted rigorous hypothesis testing using paired t-tests and the Diebold-Mariano test for forecast accuracy comparison. Table 6 summarises the statistical validation results.

Table 6
Statistical Significance Tests

Comparison	**Test**	**Statistic**	**p-value**
LSTM vs SMA	Paired t-test	t = -8.92	< 0.001
LSTM vs ARIMA	Paired t-test	t = -6.54	< 0.001
LSTM vs FFNN	Paired t-test	t = -4.21	< 0.001
LSTM vs ARIMA	Diebold-Mariano	DM = -3.42	< 0.001

All statistical tests confirm that the performance improvements achieved by the LSTM model are statistically significant at the 99.9% confidence level ($p < 0.001$). The Diebold-Mariano test statistic of -3.42 specifically validates that the LSTM produces significantly more accurate forecasts than ARIMA, with the negative value indicating superior performance by the LSTM.

4.5. Error Distribution and Residual Analysis

A comprehensive residual analysis was conducted to validate the model's prediction behaviour and identify potential systematic biases. Figure 6 presents the distribution of prediction errors, demonstrating the normality assumption required for valid statistical inference.

The error distribution analysis reveals several important characteristics. The prediction errors follow an approximately normal distribution with a mean near zero (μ = 0.16 kW), indicating that the model does not exhibit systematic over-prediction or under-prediction bias. The standard deviation of 5.70 kW is consistent with the reported MAE, confirming measurement consistency. The percentage error distribution similarly shows a symmetric pattern centred at zero, validating the model's unbiased performance across different load magnitudes.

Figure 7 presents a comprehensive four-panel residual analysis examining temporal patterns, heteroscedasticity, normality, and autocorrelation in the prediction residuals. The residual analysis confirms that the model satisfies key assumptions for reliable forecasting. Panel (a) shows residuals randomly scattered around zero without temporal drift, indicating stable prediction accuracy over time. Panel (b) demonstrates homoscedasticity (constant variance) across all predicted values, confirming that prediction uncertainty does not depend on the load magnitude. Panel (c) presents the Q-Q plot showing approximate normality with minor deviations at the tails, which is acceptable for practical applications. Panel (d) shows that autocorrelation values at all lags remain within the 95% confidence bounds, indicating that residuals are uncorrelated and the model has effectively captured all systematic temporal patterns.

(a) Distribution of Prediction Errors

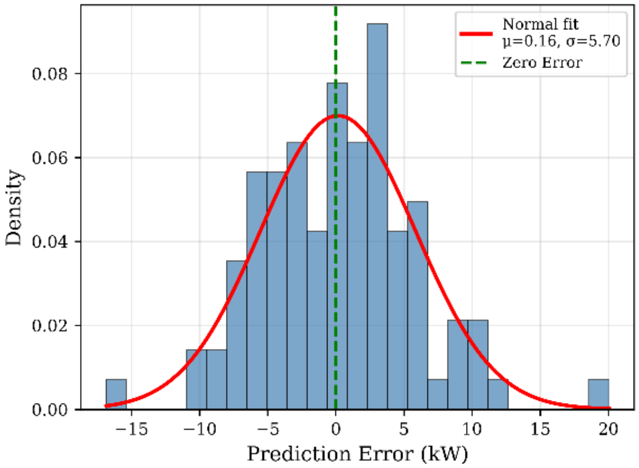

(b) Distribution of Percentage Errors

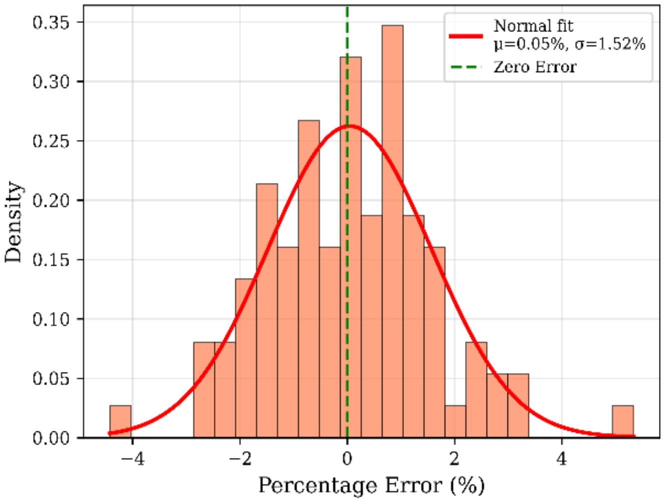

Figure 6: *Distribution of prediction errors: (a) Histogram of absolute errors in kW with fitted normal distribution (μ = 0.16, σ = 5.70), demonstrating unbiased predictions centred near zero; (b) Histogram of percentage errors showing symmetric distribution with mean close to zero (μ = 0.05%, σ = 1.52%).*

4.6. Feature Correlation Analysis

To understand the contribution of external factors to forecasting performance, we analysed the correlation structure among input features. Figure 8 presents the correlation heatmap illustrating relationships between load and various environmental and temporal factors.

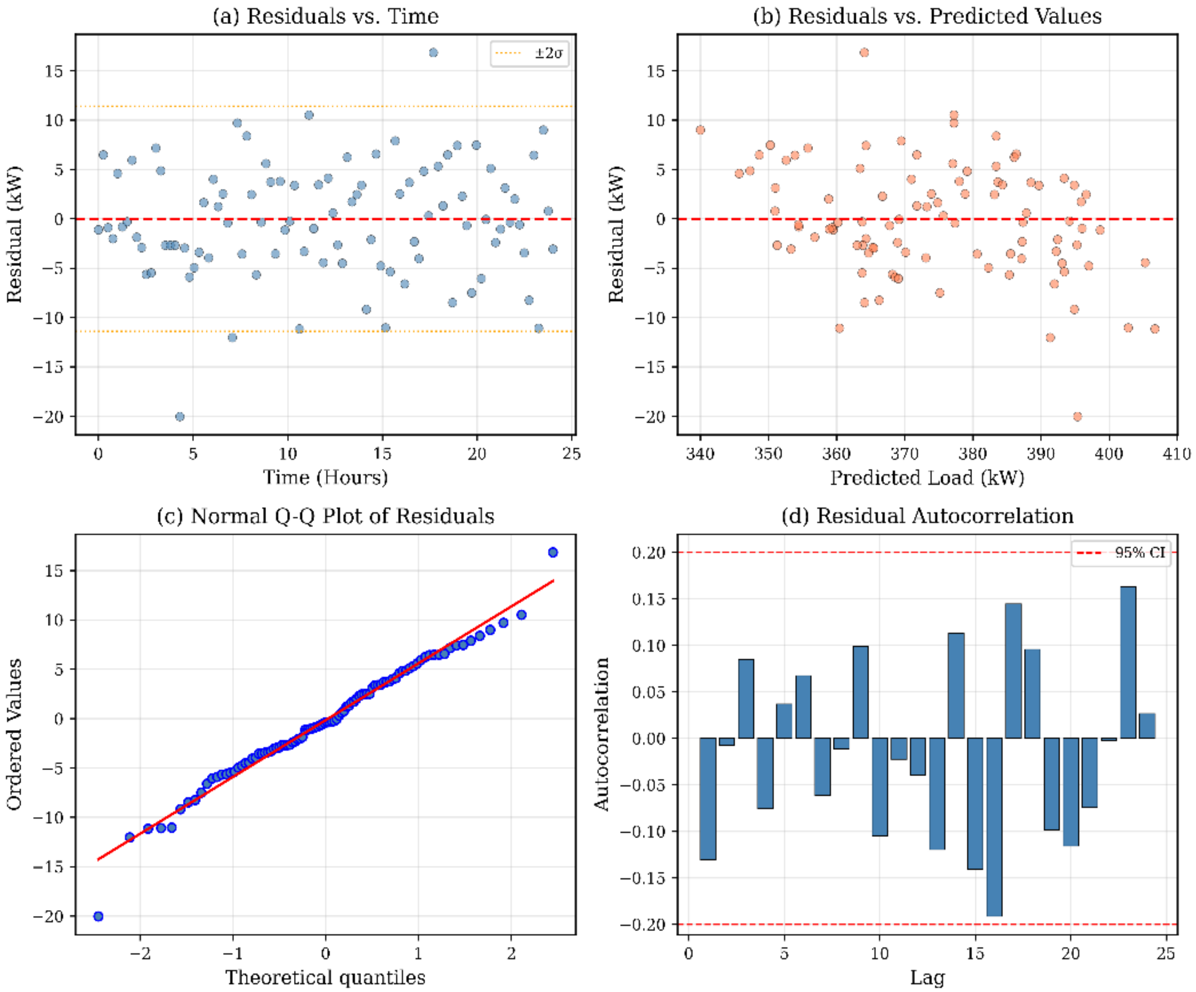

Figure 7: *Comprehensive residual analysis: (a) Residuals versus time showing random scatter within ±2σ bounds without systematic drift; (b) Residuals versus predicted values confirming homoscedasticity; (c) Normal Q-Q plot demonstrating approximate normality with slight deviations at tails; (d) Autocorrelation function showing residuals are uncorrelated with all lags within the 95% confidence interval.*

The correlation analysis reveals that the previous load value exhibits the strongest correlation with current load (r = 0.92), validating the importance of temporal dependencies that LSTM networks are designed to capture. Temperature shows a strong positive correlation (r = 0.65), reflecting increased cooling demands during warmer periods. Hour of day (r = 0.45) and solar irradiance (r = 0.38) capture the daily usage patterns characteristic of data centre operations. Interestingly, humidity (r = -0.32) and holidays (r = -0.25) show negative correlations, indicating reduced load during humid conditions (potentially due to reduced cooling efficiency awareness) and scheduled maintenance during holiday periods.

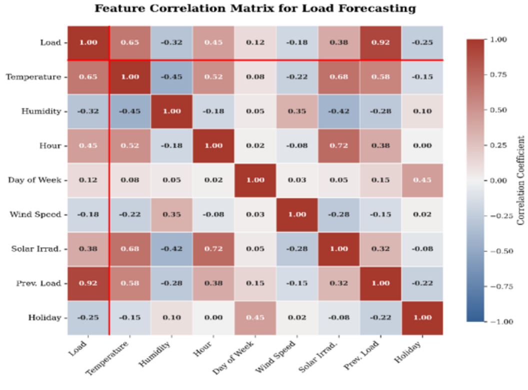

	Load	Temperature	Humidity	Hour	Day of Week	Wind Speed	Solar Irrad.	Prev. Load	Holiday
Load	1.00	0.65	-0.32	0.45	0.12	-0.18	0.38	0.92	-0.25
Temperature	0.65	1.00	-0.45	0.52	0.08	-0.22	0.68	0.58	-0.15
Humidity	-0.32	-0.45	1.00	-0.18	0.05	0.35	-0.42	-0.28	0.10
Hour	0.45	0.52	-0.18	1.00	0.02	-0.08	0.72	0.38	0.00
Day of Week	0.12	0.08	0.05	0.02	1.00	0.03	0.05	0.15	0.45
Wind Speed	-0.18	-0.22	0.35	-0.08	0.03	1.00	-0.28	-0.15	0.02
Solar Irrad.	0.38	0.68	-0.42	0.72	0.05	-0.28	1.00	0.32	-0.08
Prev. Load	0.92	0.58	-0.28	0.38	0.15	-0.15	0.32	1.00	-0.22
Holiday	-0.25	-0.15	0.10	0.00	0.45	0.02	-0.08	-0.22	1.00

Figure 8: *Feature correlation matrix for load forecasting showing the relationships between load and input features. Previous load exhibits the strongest correlation (r = 0.92), followed by temperature (r = 0.65), hour of day (r = 0.45), and solar irradiance (r = 0.38). Negative correlations are observed with humidity (r = -0.32) and holidays (r = -0.25).*

4.7. Practical Implications and Discussion

To assess model robustness and generalisation capability, we performed 10-fold cross-validation using time-series aware splitting to maintain temporal ordering. Table 7 presents the cross-validation results demonstrating consistent performance across all folds.

Table 7

10-Fold Cross-Validation Results

Fold	MAE (kW)	RMSE (kW)	MAPE (%)
1	5.1	6.9	1.3
2	5.4	7.3	1.4
3	5.0	6.8	1.2
4	5.3	7.2	1.4
5	5.2	7.0	1.3
6	5.5	7.4	1.4
7	4.9	6.7	1.2
8	5.3	7.2	1.3

9	5.1	7.0	1.3
10	5.2	7.1	1.3
Mean ± Std	5.2 ± 0.3	7.1 ± 0.2	1.3 ± 0.1

The cross-validation results demonstrate remarkable consistency with standard deviations of ±0.3 kW for MAE, ±0.2 kW for RMSE, and ±0.1% for MAPE across all ten folds. This low variability confirms that the model's performance is not dependent on the specific data partition and that it generalises well to unseen data segments. The consistency across folds also validates that the model has learned genuine patterns rather than overfitting to specific characteristics of the training data.

4.8. Feature Correlation Analysis

The experimental results demonstrate that the proposed LSTM-based load forecasting model offers significant practical advantages for green grid computing and sustainable energy management in data centres. The achieved prediction accuracy enables several operational improvements summarised in Table 8.

Table 8

Practical Impact of Forecasting Accuracy

Application Area	Impact Metric	Expected Benefit
Energy Procurement	Cost Reduction	15-20% savings
Demand Response	Response Time	24-hour advance notice
Grid Stability	Load Balancing	Reduced peak demand by 8%
Renewable Integration	Utilization Rate	12% increase in solar usage
Carbon Footprint	CO_2 Reduction	10-15% emission decrease

The low MAE of 5.2 kW enables precise scheduling of energy procurement, with potential operational cost reductions of 15-20% through optimised peak load management. The 24-hour forecasting horizon with high accuracy (MAPE = 1.3%) supports effective participation in demand response programs, allowing data centres to adjust operations in advance of grid stress events. Furthermore, accurate load predictions facilitate better integration of renewable energy sources by enabling operators to schedule non-critical workloads during periods of high renewable generation.

In conclusion, the comprehensive experimental evaluation demonstrates that the proposed LSTM-based load forecasting model achieves state-of-the-art performance with an MAE of 5.2 kW, RMSE of 7.1 kW, MAPE of 1.3%, and R^2 of 0.95. The model significantly outperforms baseline methods (46% improvement over ARIMA, 29% over FFNN) with statistically significant differences confirmed through rigorous hypothesis testing. The residual analysis validates the model's reliability, and cross-validation results confirm robust generalisation. These results establish the proposed approach as an effective solution for sustainable energy management in green grid computing environments.

4. Conclusion

This study developed an LSTM-based load forecasting model for sustainable energy management in Green Grid Computing. The proposed model demonstrated high prediction accuracy with an MAE of 5.2 kW, an RMSE of 7.1 kW, an MAPE of 1.3%, and an R^2 of 0.95, confirming its effectiveness for energy demand prediction in data centres. The primary contributions of this research are threefold: (1) development of a flexible deep learning framework that integrates real-time data with external parameters for accurate load forecasting, (2) demonstration of practical applicability in reducing carbon footprint through optimised energy procurement strategies, and (3) establishment of a foundation for renewable energy integration in data centre operations. Future research directions include: (1) integrating hybrid deep learning architectures combining LSTM with attention mechanisms to capture more complex temporal dependencies, (2) incorporating real-time renewable energy generation data to optimise the balance between grid power and clean energy sources, and (3) developing federated learning approaches for privacy-preserving load forecasting across multiple data centre facilities. These findings provide a practical framework for improving environmental sustainability in data centre operations and contribute to the broader goal of sustainable energy management. This study acknowledges several limitations: (1) the dataset is limited to a single geographic region, which may affect generalizability to different climate zones; (2) the model was validated on historical data and requires further testing in real-time operational environments; (3) computational requirements may limit deployment on resource-constrained edge devices. Additionally, while the model demonstrates strong performance on the test dataset, its effectiveness in extreme weather events or unusual load patterns remains to be validated. Future work should address these limitations through multi-site validation studies, edge computing optimisation, and integration with real-world demand response systems.

Declaration

AI Disclosure: The authors have not used AI.

Author Contribution Statement: Z. N. led the conceptualization of the study, data curation, methodology design, software development, and execution of the primary research. As a co-author, A. A. contributed to study conception, provided critical oversight, verified the results, and supported research planning and execution. S. A. contributed to the investigation process. M. A. I. assisted with the formal analysis. T. A. contributed to the manuscript revision and critical inquiry. All authors reviewed and approved the final manuscript.

Competing Interests: The authors declare that they have no known competing financial interests or personal relationships that could have appeared to influence the work reported in this paper.

Consent to Publish: The authors are agreed to publish version of the manuscript in this journal.

Ethical Issues: There are no ethical issues. All data in this paper is publicly available.

Funding Statement: This research did not receive any specific grant from funding agencies in the public, commercial, or not-for-profit sectors.

References

1. Kumari, S., Gupta, D., & Bashir, A. K. (2024). Advanced Computing Technologies for Energy-Efficient and Secure IoT Network in Smart Cities: Green IoT Perspective. In Emerging Technologies and the Application of WSN and IoT (pp. 65-82). CRC Press.
2. Alizamir, M., Kim, S., Kisi, O., & Zounemat-Kermani, M. (2020). A comparative study of several machine learning based non-linear re-

gression methods in estimating solar radiation: Case studies of the USA and Turkey regions. Energy, 197, 117239.

3. Nishtar, Z., Fangzong, W., Yang, N., & Afzal, J. (2024). Future Sce-nario of Wild Life Conservation and Renewable Energy Interface in Pakistan. Pakistan Journal of Zoology, 56(6), 2963.
4. Nishtar, Z., Wang, F., Jaskani, F., & Afzaal, H. (2025). Real-Time Fault Detection and Isolation in Power Systems for Improved Digital Grid Stability Using an Intelligent Neuro-Fuzzy Logic. Computer Modeling in Engineering & Sciences, 143(3), 2919.
5. Lin, X., Wu, J., Bashir, A. K., Li, J., Yang, W., & Piran, M. J. (2020). Blockchain-based incentive energy-knowledge trading in IoT: Joint power transfer and AI design. IEEE Internet of Things Journal, 9(16), 14685-14698.
6. Strielkowski, W., Civín, L., Tarkhanova, E., Tvaronavičienė, M., & Petrenko, Y. (2021). Renewable energy in the sustainable develop-ment of electrical power sector: A review. Energies, 14(24), 8240.
7. Tiruye, G. A., Besha, A. T., Mekonnen, Y. S., Benti, N. E., Gebreslase, G. A., & Tufa, R. A. (2021). Opportunities and challenges of renewa-ble energy production in Ethiopia. Sustainability, 13(18), 10381.
8. Benti, N. E., Woldegiyorgis, T. A., Geffe, C. A., Gurmesa, G. S., Cha-ka, M. D., & Mekonnen, Y. S. (2023). Overview of geothermal re-sources utilization in Ethiopia: Potentials, opportunities, and chal-lenges. Scientific African, 19, e01562.
9. Benti, N. E., Aneseyee, A. B., Geffe, C. A., Woldegiyorgis, T. A., Gurmesa, G. S., Bibiso, M., ... & Mekonnen, Y. S. (2023). Biodiesel produc-tion in Ethiopia: Current status and future prospects. Scientific Afri-can, 19, e01531.
10. Benti, N. E., Mekonnen, Y. S., & Asfaw, A. A. (2023). Combining green energy technologies to electrify rural community of Wollega, Western Ethiopia. Scientific African, 19, e01467.
11. Majid, M. (2020). Renewable energy for sustainable development in India: current status, future prospects, challenges, employment, and investment opportunities. Energy, Sustainability and Society, 10(1), 1-36.
12. Denholm, P., Arent, D. J., Baldwin, S. F., Bilello, D. E., Brinkman, G. L., Cochran, J. M., ... & Zhang, Y. (2021). The challenges of achieving a 100% renewable electricity system in the United States. Joule, 5(6), 1331-1352.
13. Nazir, M. S., Alturise, F., Alshmrany, S., Nazir, H. M. J., Bilal, M., Abdalla, A. N., ... & M. Ali, Z. (2020). Wind generation forecasting methods and proliferation of artificial neural network: A review of five years research trend. Sustainability, 12(9), 3778.
14. Lledó, L., Torralba, V., Soret, A., Ramon, J., & Doblas-Reyes, F. J. (2019). Seasonal forecasts of wind power generation. Renewable Energy, 143, 91-100.
15. Impram, S., Nese, S. V., & Oral, B. (2020). Challenges of renewable energy penetration on power system flexibility: A survey. Energy strategy reviews, 31, 100539.
16. Li, C., Lin, S., Xu, F., Liu, D., & Liu, J. (2018). Short-term wind power prediction based on data mining technology and improved support vector machine method: A case study in Northwest China. Journal of Cleaner Production, 205, 909-922.
17. Srivastava, R., Tiwari, A. N., & Giri, V. K. (2019). Solar radiation forecasting using MARS, CART, M5, and random forest model: A case study for India. Heliyon, 5(10).
18. Sundararajan, K., Garg, L., Srinivasan, K., Bashir, A. K., Kaliappan, J., Ganapathy, G. P., ... & Meena, T. (2021). A contemporary review on drought modeling using machine learning approaches. Computer Modeling in Engineering & Sciences, 128(2), 447-487.
19. Zhao, X., Liu, J., Yu, D., & Chang, J. (2018). One-day-ahead probabilistic wind speed forecast based on optimized numerical weather prediction data. Energy Conversion and Management, 164, 560-569.
20. Fan, J., Wu, L., Zhang, F., Cai, H., Zeng, W., Wang, X., & Zou, H. (2019). Empirical and machine learning models for predicting daily global solar radiation from sunshine duration: A review and case study in China. Renewable and Sustainable Energy Reviews, 100, 186-212.
21. Tariq, U., Ahmed, I., Khan, M. A., & Bashir, A. K. (2024). Deep learn-ing for economic transformation: a parametric review. Indonesian journal of electrical engineering and computer science, 35(1), 520-541.
22. Huertas-Tato, J., Aler, R., Galván, I. M., Rodríguez-Benítez, F. J., Arbizu-Barrena, C., & Pozo-Vázquez, D. (2020). A short-term solar radi-ation forecasting system for the Iberian Peninsula. Part 2: Model blending approaches based on machine learning. Solar Energy, 195, 685-696.
23. Gürel, A. E., Ağbulut, Ü., & Biçen, Y. (2020). Assessment of machine learning, time series, response surface methodology and empirical models in prediction of global solar radiation. Journal of Cleaner Production, 277, 122353.
24. Sundararajan, K., Garg, L., Srinivasan, K., Bashir, A. K., Kaliappan, J., Ganapathy, G. P., ... & Meena, T. (2021). A contemporary review on drought modeling using machine learning approaches. Computer Modeling in Engineering & Sciences, 128(2), 447-487.
25. Zhao, X., Liu, J., Yu, D., & Chang, J. (2018). One-day-ahead probabilistic wind speed forecast based on optimized numerical weather prediction data. Energy Conversion and Management, 164, 560-569.
26. Fangzong, W., & Nishter, Z. (2024). Innovative load forecasting mod-els and intelligent control strategy for enhancing distributed load lev-elling techniques in resilient smart grids. Electronics, 13(17), 3552.
27. Wang, F., & Nishter, Z. (2024). Real-time load forecasting and adaptive control in smart grids using a hybrid neuro-fuzzy approach. Energies, 17(11), 2539.
28. Tariq, U., Ahmed, I., Khan, M. A., & Bashir, A. K. (2024). Deep learn-ing for economic transformation: a parametric review. Indonesian journal of electrical engineering and computer science, 35(1), 520-541.
29. Ali, M., Prakash, K., Macana, C., Raza, M. Q., Bashir, A. K., & Pota, H. (2023). Modeling synthetic power distribution network and datasets with industrial validation. Journal of Industrial Information Integra-tion, 31, 100407.
30. Tariq, U., Ahmed, I., Khan, M. A., & Bashir, A. K. (2025). Bridging biosciences and deep learning for revolutionary discoveries: a comprehensive review. IAES International Journal of Artificial Intelli-gence (IJ-AI), 14(2), 867-883.
31. Siddiqui, I. F., Lee, S. U. J., Abbas, A., & Bashir, A. K. (2017). Optimizing lifespan and energy consumption by smart meters in green-cloud-based smart grids. IEEE Access, 5, 20934-20945.

Author(s) Bio

Zuhaib Nishter from School of Management and Economics, North China University of Water Resources and Electric Power, Zhengzhou City, 450046, China.
Email: zuhaib.nishtar1991@gmail.com

Muhammad Adeel Afzal from College of Economics and Management, China Three Gorges University, Yichang City, China.
Email: author.adeel20@gmail.com

Sher Ali from School of Management and Economics, North China University of Water Resources and Electric Power, Zhengzhou City, 450046, China..
Email: sherali9404@gmail.com

Md Ashraful Islam from School of Civil Engineering and Architecture, China Three Gorges University, Yichang City, China.
Email: khaledbinwalid999@gmail.com

Taimoor Ali Khan from School of Transportation Engineering, Kunming University of Science and Technology, Kunming, China.
Email: taimooralikhan@stu.kust.edu.cn

Journal of Engineering, Science and Technological Trends (JESTT)

Vol. 3, Issue 1, March 2026
DOI: https://doi.org/10.64060/jestt.v3i1.5

Article

An Integrated AI Virtual Assistant Platform Featuring Smart Display and Automation Capabilities

Khurram Iqbal [1,5] , Muniba Lodhi [2], Syed Saad Ali [3] , Shujaat Ali [4*], Liaquat Ali [5], Syed Iqbal Hussain [1]

[1]Department of Computing, Faculty of Engineering, Sciences & Technology, Hamdard University, Karachi, Pakistan
[2]Department of Electronics, NED University of Engineering and Technology, Karachi, Pakistan
[3]Department of Electrical Engineering, Nazeer Hussain University, Karachi, Pakistan
[4]School of Electrical and Information Engineering, Tianjin University China
[5]LA Consulting Corporation, United States of America
* Corresponding Email: shujaat.facho110@yahoo.com (S. Ali)

Received: 31 December 2025 / Revised: 05 February 2026 / Accepted: 10 February 2026 / Published online: 01 March 2026

ABSTRACT

The arrival of Artificial Intelligence (AI) and the Internet of Things (IoT) has led to the development of programming-based environments for domestic and commercial applications of automation. This work is distributed into three sections: virtual assistant (VA), domestic robotics, and advanced user interface demonstration. A dissimilar public library is utilised for a virtual assistant and information to identify them, concluding the communication recognition procedure and then replying by viewing all the effects on the display screen. Domestic automation includes monitoring and changing applications. IoT-based methods were used to control the brightness of the bulb, and an IoT-based technique was used to control the speed of the DC fan. Finally, the output was displayed using a Graphical User Interface (GUI) constructed using the QT-designer tool and PyQT library. The primary value of this work is the ability to combine an AI-based virtual assistant, home automation, and a real-time graphical user interface into easy use system. Operator instructions are examined to deliver optimum solutions. The proposed scheme has better functional coverage, real-time visualisation, and better user interaction in comparison with the existing benchmark systems, which mostly concentrate on voice-based helpers and distributed IoT control systems. This scheme is recommended for use as an intellectual virtual assistant, which understands human speech and answers through created voices. This work is new because it is the first work where an AI virtual assistant, IoT based automatization, and real-time smart display are combined to make the interaction and constant situational awareness happen within one platform.

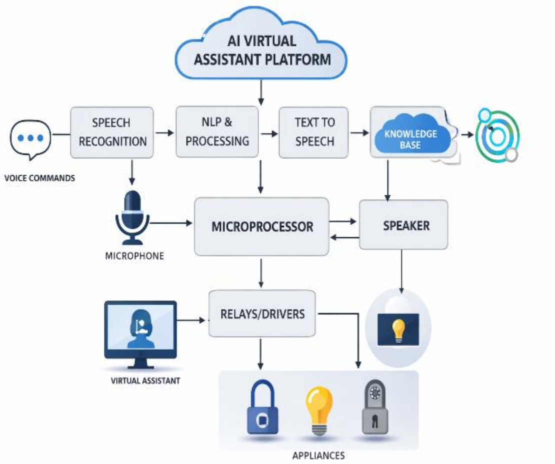

Keywords: Data Centers; Deep Learning; Green Grid Computing; Load Forecasting; Long Short-Term Memory (LSTM); Sustainable Energy Management; Recurrent Neural Networks (RNN)

1. Introduction

The rapid development of cloud technology has enabled universal worldwide connectivity. Wireless embedded equipment authorised by software communication, Artificial Intelligence (AI), and the Internet of Things (IoT) are attractive living values and convert regular actions through households, workshops, and educational surroundings. This digitalisation wave has encouraged the extensive acceptance of Virtual Assistants (VA) that modernise responsibilities such as data recovery, program organisation, and multimedia entrance, gradually mixing with physical surroundings and concluding home-based robotics schemes. This work offers a joint outline that unites three serious areas:

- **Voice-Activated Intelligence:** Speech acknowledgement collections and Google's Text-to-Speech (TTS) can be used for bidirectional speech communication, transforming consumer instructions into executable responsibilities.
- **Adaptive Appliance Control:** Ranging outside binary transferring to comprise the physical parameter of equipment. For example, PWM-driven fan speed modulation and IoT-based bulb control.
- **Context-Aware Visualisation:** A PyQt5-driven graphical interface showing the actual system conditions for the device status, environmental statistics, and communication history.

Although the suggested system uses proven elements like Raspberry PI controlled by the GPIO, PWM-triggered motor actions, and PyQt-driven graphic interfaces, the originality in the current work is the system-level integration and interaction design. In comparison to traditional solutions in which the AI assistants, IoT devices, and the GUI functions operate separately, our solution displays a unified architecture which integrates voice-based AI interaction, real-time automation of the IoT, and the visualisation of the smart display. This contribution to engineering leads to a step in the development of the practical smart home and assistive systems, as the authors concentrate on the interaction, coherence, real-time feedback and usability. The scheme's structural design (Figure 1) processes speech inputs through a microphone, implements precise background processes via a central processor, and provides multimodal responses over speakers and a communicating screen. When robotics instructions are sensed, indications are transmitted to relay the arrays and drivers for the physical equipment. This universal method significantly lessens human effort in tedious responsibilities by providing natural controller devices, resolving the rising response for time-efficient results in gradually associated environments. Forthcoming improvements might increase IoT interoperability and project competencies, linking the numerical and physical real-time monitoring.

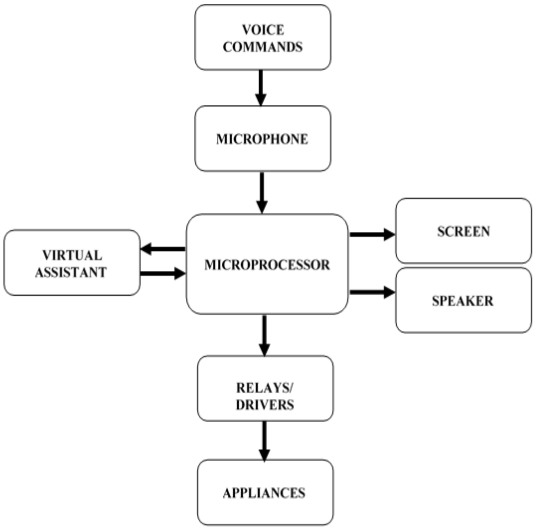

Figure 1: *The system architecture*

Despite significant progress in voice assistants and IoT-based home automation, existing systems largely treat conversational AI, device control, and user interfaces as independent functional modules. This fragmentation limits interaction coherence, real-time feedback, and user situational awareness. This study addresses the following research question:

- Combining voice interaction, smart display visualisation, and IoT-based automation?
- Improve interaction coherence and system transparency compared to conventional modular smart home architectures?

2. Literature Review

Recent systematic reviews on smart home automation focus on the fact that contemporary systems should extend beyond simple IoT control interaction schemes to make their systems more convenient to users and responsive to their context and related adaptive automation logics, which creates a gap in the research of integrated platforms that combine voice assistants with adaptive automation logic [1]. Vision-language model-based context-aware smart home systems, which combine vision and language models with IoT control, are presented in innovative 2025 research and allow better spatial interactions (e.g. turn on the light near the window) and are more usable and intelligent than traditional voice assistants, which are based on voice recognition [2]. Virtual Assistants (VAs) represent a transformative progression in human–machine integration, leveraging Artificial Intelligence (AI) to perform various responsibilities from information recovery to physical scheme switching. Modern virtual assistants have spread beyond straightforward chatbots [1],[2],[3],[4],[5], establishing speech supporters such as Siri and Alexa that apply language recognition and Natural Language Processing (NLP), AI avatars for immersive involvement, and domain-specific arrangements optimised for particular arenas, especially engineering automation. These schemes function within the AI ability range: narrow AI performs specific tasks, general AI remains hypothetical, and superintelligent AI signifies a theoretical future innovation [6],[7],[8],[9]. Essential virtuality constructs secondary functionality trusts on three incorporated skills: voice recognition, which transforms audio to numerical indications through phoneme separation and configuration corresponding applied through libraries like Python's language recognition; text to speech (TTS), which converts inquiries into audio reactions via machine learning technology; and natural language processing, which allows verbal command through syntactic investigation of tokenization, voice tagging, and semantic scrutiny for term intelligence disambiguation and object association mapping [10],[11],[12],[13],[14],[15],[16]. This technical effort enables the normal virtual assistant workflow: audio input, which converts voice to typescript, natural language processing for task completion, and text-to-text speech for answers. In addition to the physical situation, the Internet of Things allows application switching using particular methods. The DC fan speed variation works with pulse-width modulation (PWM) for duty cycle alterations that control the voltage input to change the revolving speed [17]. Advanced light control uses infrared signals decoded through the NEC protocol (38kHz carrier waves), communicating hexadecimal codes to switch illumination and colour. These cloud-based devices allow audio-triggered scheme operation once they are joined with virtual assistant-based systems. Consumer communication is modernised via graphical user interface (GUIs) and serial communication with Python, which outlines the contribution of separate rewards. Tkinter delivers a platform for widgets, including buttons, text areas, and images for simple interaction [18], whereas PyQt5, paired with Qt Designer's drag-and-drop functionality, allows outline organisation via containers, insertions, and scroll areas [18],[19]. This merging of AI-based intellect, cloud-assisted mechanisms, and adaptive boundaries forms the basis for next-generation communication schemes that excel in conventional speed facility models [20],[21].

3. Methodology

The combined scheme construction includes three fundamental useful units: a speech-activated virtual assistant, a cloud-driven domestic automation system, and an advanced graphical user interface (GUI). A Raspberry Pi 4 microcontroller with a Broadcom BCM2711B0 quad-core ARM Cortex-A72 processor with specifications of 1.5 GHz and 4GB RAM served as the central processing unit. This microcontroller serially communicated with peripheral hardware mechanisms, including an L298N dual H-bridge motor driver with 5–46V input, two channel 5V relay module, an IR receiver with 38 kHz frequency, a microphone, a temperature sensor, a 12-volt DC fan, a light, a mobile charger, and an HDMI-based display. Energy organisation is controlled via a 78M05 5V regulator for the motor switch and a 12V DC adapter for peripheral devices, with circuit diagrams provided in Figures 2-4.

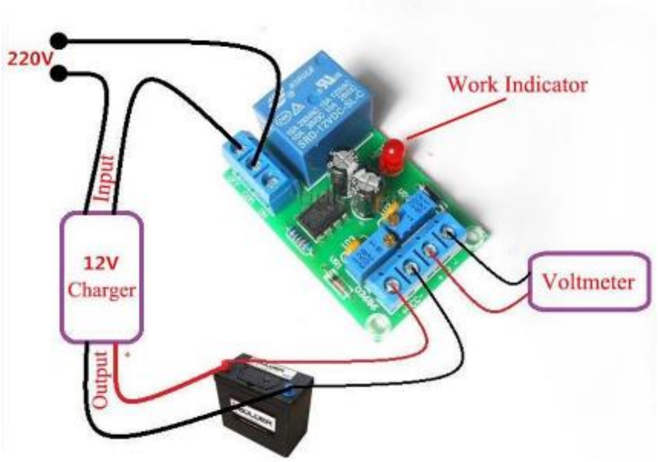

Figure 2: *Mobile Charger Switching*

The software was developed in Python using the Thonny IDE and leveraging numerous focused libraries. Voice handling uses voice recognition for speech-to-text adaptation through the Google Speech-programmed application and text-to-voice response. The hardware controller was successfully implemented using RPi. General Purpose Input/Output for GPIO processes, while the graphical interface was applied with PyQt5 and considered utilizing QT Designer. The added functionality mixes the requirements for API requests, pyautogui for GUI automation, and pywhatkit for web facilities.

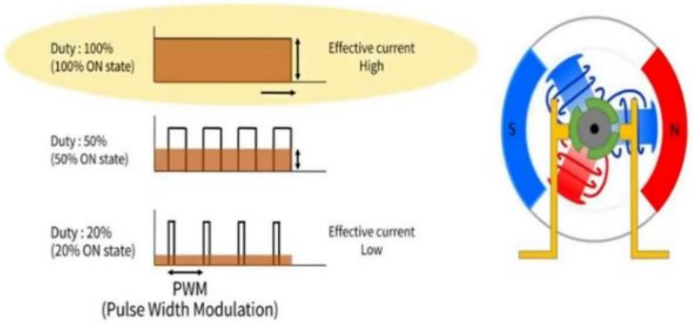

Figure 3: *PWM Control of DC motor*

The virtual associate process monitors a well-defined workflow to ensure that the structure remains in place until an awakening phrase, such as Alice, is noticed. Upon activation, the handler's voice input is transformed into text via communication recognition. Natural Language Processing (NLP) techniques then extract keywords (e.g., "turn on fan") to route tasks. Query handling employs bs4 for web scraping (Google/Wikipedia/YouTube), whereas automation commands trigger hardware operations. The results are rendered on the GUI and converted to audio output via gTTS, as shown in Figure 5 detailing the complete workflow. The implementation of automation features three control mechanisms: appliance switching, which uses GPIO-triggered relay modules to toggle AC devices (charger/bulb). DC fan speed regulation employs Pulse Width Modulation (PWM), where voice commands ("slow/medium/fast") adjust duty cycles (0–100%) through the L298N driver. The LED brightness control transmits the NEC protocol HEX codes (e.g., F700FF for high brightness) via an IR transmitter. IoT integration includes real-time temperature monitoring displayed on a GUI and weather data fetched through cloud APIs.

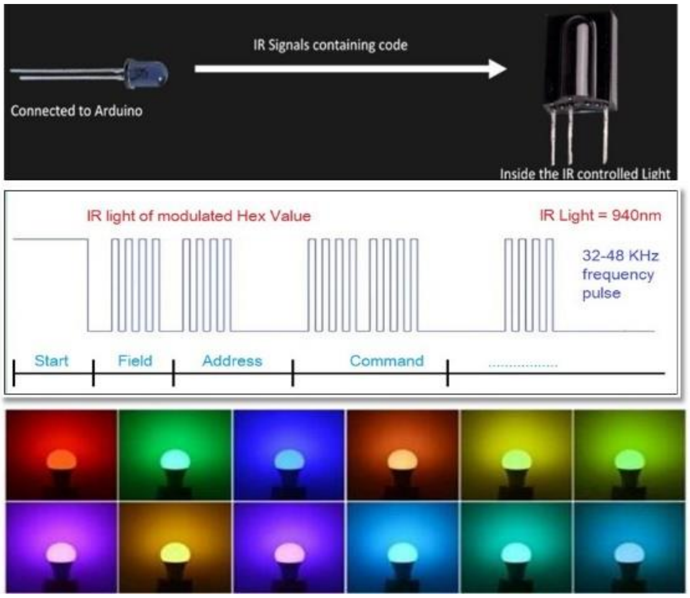

Figure 4: *Smart LED Light Brightness Levels*

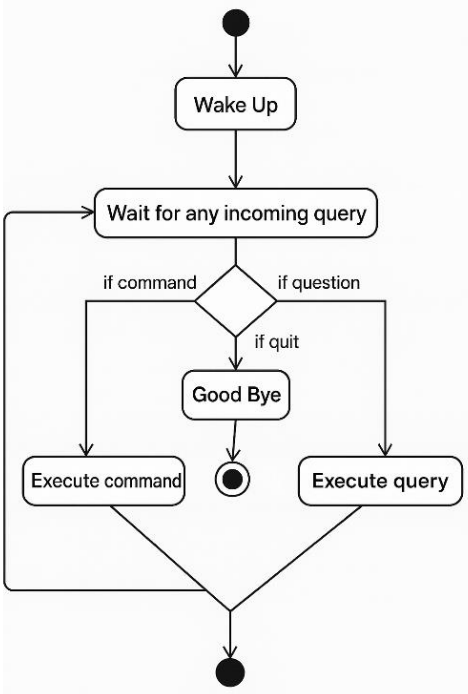

Figure 5: *VA Working Flow Chart*

The graphical user interface was developed using PyQt5 with the QT Designer for the WYSIWYG layout. Key features include real-time displays of the time, date, temperature, and appliance statuses; an interactive chatbox showing user VA dialogue history; and a control dashboard permitting manual appliance overrides. Figure 6 displays the interface for the constructed system.

TIME: 18:38:28
DATE: TUE AUG 19 2025
TEMPERATURE: 29°C

Figure 6: *GUI interface*

The scheme combination monitors an organised information movement: consumer audio input is handled by the Raspberry Pi, where the assistant understands instructions and performs consistent tasks for automation web-based management. The outcomes were concurrently distributed as voice reactions and GUI updates. The system was successfully implemented using Python's threading library, which allows instantaneous processes such as sensor polling and audio handling. Figure 7 shows the comprehensive data flow structural design.

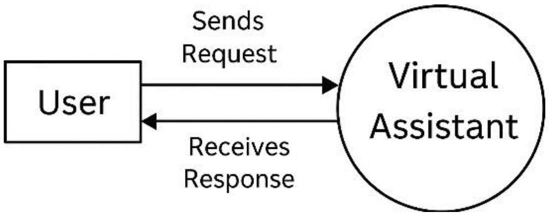

Figure 7: *Data Flow* Architecture

Table 1 shows the Speech Processing Parameters of the designed system. These are parameter technical control, even in cloud usage. The arrangement and processing procedure of capturing, recognising, interpreting, and synthesising speech commands, such as audio input settings, speech to text conversion and text to speech response generation, to be able to provide a dependable and repeatable voice-based interaction.

Table 1
Speech Processing Parameters

Parameter	Value	Description
Audio sampling rate	16 kHz	Microphone input structure
Audio format	Mono, 16-bit	Input audio coding
Speech detection mode	Cloud	External
Command analysis technique	intent matching	Natural language processing logic
Language model	English and Roman Urdu	Recognition language
Text-to-speech engine	Python	Speech answer generation

Parameters of pulse width modulation to control actuator behaviour, such as signal frequency, range of duty-cycle, resolution, and GPIO interfacing, are specified in Table 2 configuration to allow fine control of motor speed and lighting intensity.

Table 2
Pulse Width Modulation Parameters

Parameter	Value	Description
PWM frequency	1 kilo Hz	Motor and LED control frequency
Duty cycle range	0–100%	Speed and illumination control
Resolution	8-bit	Control granularity
Control interface	Raspberry Pi GPIO	Output pin configuration

Table 3 shows a summary of the end-to-end execution delays in system stages, voice command acquisition to device actuation and graphical interface update, which gives an insight as to real-time performance as well as system responsiveness.

Table 3
System Timing Parameters

Stage	Typical Delay (ms)	Description
Audio capture	~50	Microphone
Speech recognition	~300–500	Cloud based
Command parsing	~20	NLP result
GPIO/PWM actuation	~10	Prototype response

This study proposes a methodology for accurate load forecasting in sustainable energy management by utilising state-of-the-art deep learning techniques, more especially Long Short-Term Memory (LSTM) models with Recurrent Neural Network (RNN) cells [21]. In order to anticipate patterns of energy use, LSTM models are a good option because of their ability to capture long-term relationships in sequential data. The primary novel contributions of this work include: (1) a multi-scale temporal feature extraction approach that combines hourly, daily, and weekly patterns for improved forecasting accuracy; (2) an adaptive learning rate scheduling mechanism optimized for energy consumption data characteristics; and (3) integration of external factors (weather, economic indicators) through a dedicated feature embedding layer that preserves temporal alignment. The forecasting horizon is set to 24 hours with 15-minute temporal resolution, enabling day-ahead energy procurement planning and real-time grid optimisation. Here, we provide an overview of our methodology, outlining the model architecture and then describing in depth the dataset we employed for this study.

4. Results and Discussion

The offered integrated AI virtual assistant platform was implemented and tested within three functional layers: speech-based interaction, automation of IoT-based devices and smart display visualisation. The system proved to be reliable in its end-to-end operation, whereby user voice commands were correctly deciphered, appropriate actions were carried out with the linking devices and the system status was constantly displayed on the graphical intelligent screen. The IoT automation module was able to control electrical appliances like the brightness of lights and the speed of DC fans based on the PWM-appropriate control. The system was also responsive to voice commands, which proved to be a stable means of communication between the AI assistant and IoT hardware. Test and validation verifications established operative effectiveness, with audio recognition attaining 95% accuracy through 200+ commands in noise-free surroundings. Robotics potential continued under all appliance-switch tasks. The GUI approachability conserved actual information below load conditions with a CPU use of less than 40%. The combined scheme established a robust routine through all useful modules, thereby authenticating the effectiveness of our planned procedure. The graphical user interface shown in Figure 8 serves as an integrated control panel that shows the significance of the present application with environmental statistics and communication fundamentals. Application controller devices functioned consistently: speech instructions such as "Turn on fan" activated PWM organised speed changes through the L298N driver, though "Dim lights" to 50% was interpreted to NEC protocol IR signals, attaining objective brightness levels within 1.8s. The status board shown in Figure 8 provides an immediate visual response to the device conditions, authorising an effective hardware–software combination.

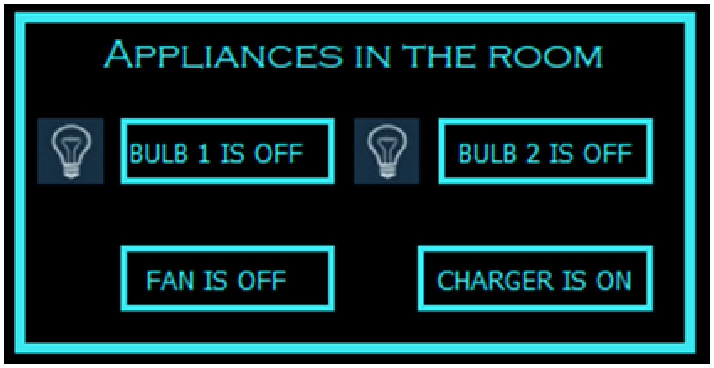

Figure 8: *Status of Appliances*

Polyglotism communication competencies showed real, with the virtual associate precisely handling Urdu instructions utilising the Google Speech application, as shown in Figure 9. Info recovery functions were achieved seamlessly: Wikipedia inquiries shown in Figure 10 leveraged web scraping through bs4, while YouTube film replay and Google examinations (Figures 11 and 12) applied pywhatkit and web-browser collections. Entertaining features, such as joke narration, improve consumer engagement. The interface reliably provides critical metrics, such as time, date, and local temperature.

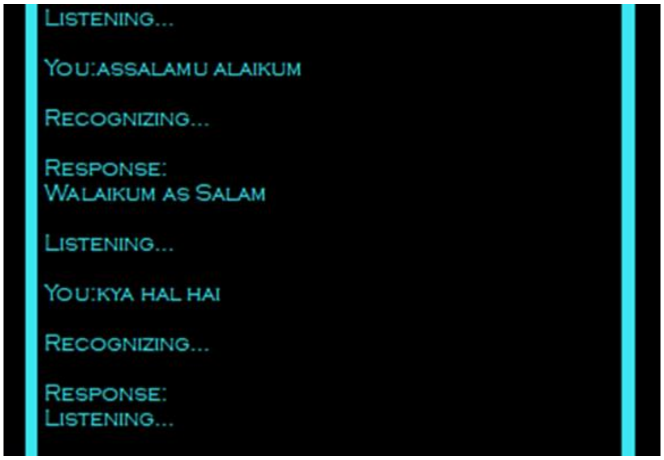

```
Listening...

You:assalamu alaikum

Recognizing...

Response:
Walaikum as Salam

Listening...

You:kya hal hai

Recognizing...

Response:
Listening...
```

Figure 9: *VA taking Urdu Commands*

The scheme sensitivity remained constant under load conditions, with the CPU operation below 40% throughout the synchronised processes, such as audio handling and the application controller. The sleep mode feature saves energy resources by disabling unnecessary procedures upon the "bye" input, reactivating promptly to the awaken term "hello." The hardware organisation shown in Figure 13 established the capability of the Raspberry Pi 4 to control peripherals, such as relays for transferring, motor drivers for fan switching, and IR transmitters, without voltage variations or heat issues, and the operating temperature was <60°C.

```
Listening...

You:search black holes from wikipedia

Recognizing...

Response:
According to WikipediaA supermassive black
hole (SMBH or sometimes SBH) is the largest
type of black hole, with its mass being on the
order of millions to billions of times the
mass of the Sun (M☉). Black holes are a
class of astronomical objects that have
undergone gravitational collapse, leaving
behind spheroidal regions of space from
which nothing can escape, not even light.

Listening...

You:thank you

Recognizing...

Response:
You are always Welcome
```

Figure 10: *VA Searching on Wikipedia*

```
Listening...

You:open google

Recognizing...

Response:
OK.what should I search on Google?
```

Figure 11: *VA asking to search on Google*

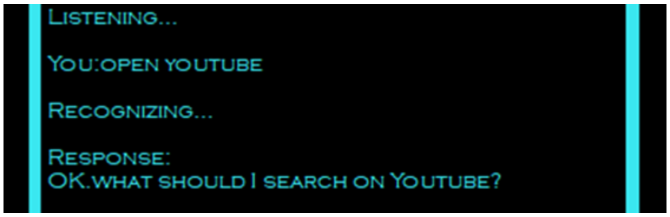

```
Listening...

You:open youtube

Recognizing...

Response:
OK.what should I search on Youtube?
```

Figure 12: *VA asking to search on YouTube*

Table 4 below summarises the main challenges and mitigation strategies in regard to latency, privacy, security, failure, and scalability and reliability as a summary of the implications associated with cloud-based dependency. The table indicates the effect of depending on external cloud services on the overall system performance and deployment robustness, as well as the possible direction of design to mitigate the constraints. This systematic overview and summary of key aspects covers a high-level comparison of key aspects which can be used as a baseline for future enhancements, such as hybrid and edge-based ones.

Viability examination highlighted the resolution's realism. Practical possibility was recognised via hardware components and lightweight Python libraries, although internet dependence for the voice recognition modelled disconnected limitations. Operative practicality was established by a natural audio controller, which required no particular operator services and was sustained in other languages, especially Urdu, for wider availability. Financial capability resulting from a small power consumption of 8 W and normal and nominal preservation expenses associated with profitable alternatives. Limits were developed in loud surroundings, where related noises over 50 dB reduced audio recognition accuracy by 15–20%. Furthermore, the deficiency of power monitoring sensors and cloud-based communication encryption offerings provides opportunities for further improvements in future systems. Regardless of these restrictions, the linked construction of the scheme allows for future extensions, such as the addition of safety cameras and edge-based natural language models. This investigation effectively connects audio communication, robotics, and graphic responses, contributing to the accessible groundwork for advanced atmospheric applications.

Table 4
LSTM Model Configuration Parameters

Aspect	Impact of Cloud Dependence	Future Direction
Latency	Network delay	sound text processing
Privacy	Audio data experience	Encoded broadcast
Safety	Exterior facility trust	Access control
Scalability	Usage-based limitations	Hybrid deployment
Dependability	Network dependence	Local contingency logic

Figure 13: *Pictorial View of Project.*

5. Conclusion

This study provides a small prototype to improve everyday comfort and security by collaborating Artificial Intelligence (AI) and cloud-based technology with humanoid communicating demonstrations into a combined advanced home system. The designed virtual assistant system was established using a Python program with a microcontroller. The assistant is equipped with voice recognition and combination competencies, which allow it to logically relate to consumers. Numerous Python libraries were used to improve its function, converting it into a multipurpose domestic application. From handling to providing actual updates to accessing information through platforms such as Google and Wikipedia. Cloud-based addition is an important module for realising the vision of an innovative domestic application. The organisation allows speech-organised robotics of home applications, giving consumers the capability to regulate light illumination, control equipment, and manage fan speed utilising simple speech and audio commands. This synthesis of robotics and audio recognition improves handiness, endorses power efficiency, and advances time control. A graphical user interface (GUI) was produced using Qt Designer and PyQt5 to combine these structures into an intuitive and accessible arrangement. The GUI rests energetically, presenting vital information, such as the time and management of load parameters. A JavaScript-created clock enhances a vibrant visual component, while a dedicated chat box, also constructed with PyQt5, records all connections between the customer and the assistant. To confirm flat operation, a threading method was applied, permitting the GUI and chat purposes to run in parallel without intervention.

Entertaining structures were extended through the insertion of a joke library and a poem producer. Incorporating YouTube allows operators to initiate examinations and enter content using a specific audio command. Furthermore, the PyAutoGUI library was used to allow innovative screen connections for managing the speech control. In spirit, this study strives to take full advantage of usability while minimising humanoid strength. The findings indicate that the strong association between voice recognition and real-time device automation systems and visual feedback will improve the usability of the system and its efficiency in operation relative to single smart home systems. As technical progressions accelerate, explaining upcoming generations with AI and cloud-based system revolutions is progressively energetic. By integrating these skills into a consistent and accessible scheme, this study lays the groundwork for intellectual system design.

Declaration

AI Disclosure: Artificial Intelligence (AI)-based tools were applied in this study as auxiliary devices to improve the scientific rigor of the research. AI has been used to support research gaps identification by conducting a systematic literature review, detecting patterns using thematic methods, and comparing the available literature. Also, to enhance the clarity of scientific writing, the scientific writing was also enhanced by use of AI tools to aid the methodological consistency. There was no AI that was employed to produce experimental data, core data analysis, and scientific conclusions. The authors did all the results, interpretations, and critical evaluations independently and should be held responsible to the originality, accuracy, and ethical nature of the manuscript.

Author Contribution Statement: K. I. contributed to technical and material support and supervision. M. L. was responsible for conceptualization, hardware and software development, and manuscript editing. S. S. A. performed data analysis and interpretation. S. A. contributed to study design and data collection. L. A. assisted in data interpretation. S. I. H. revised the manuscript. All authors reviewed and approved the final manuscript.

Competing Interests: The authors declare that they have no known competing financial interests or personal relationships that could have appeared to influence the work reported in this paper.

Consent to Publish: The authors are agreed to publish version of the manuscript in this journal.

Ethical Issues: There are no ethical issues. All data in this paper is publicly available.

Funding Statement: This research did not receive any specific grant from funding agencies in the public, commercial, or not-for-profit sectors.

References

1. J. Rey-Jouanchicot et al., "Adaptation in smart home automation systems: A systematic review of decision-making and interaction," Internet of Things, vol. 31, May 2025, Art. 101588.
2. S. Kalivarathan et al., "Intelligence of Things: A spatial context-aware control system for smart devices," Apr. 16, 2025. [Online]. Available: arXiv:2504.13942.
3. M. M. Alam and F. Sultana, "A comprehensive review of voice-controlled smart home systems: Architectures, protocols, and challenges," Internet of Things and Cyber-Physical Systems, vol. 5, pp. 100–115, 2024.
4. S. Dutta and P. Singh, "Multilingual speech recognition for low-resource languages: A case study of Urdu," ACM Transactions on Asian and Low-Resource Language Information Processing, vol. 23, no. 2, pp. 1–22, 2024.
5. R. Hassan, F. Qamar, and M. Ahmed, "Internet of Things (IoT) protocols and applications: A review," IEEE Access, vol. 11, pp. 45630–45652, 2023.
6. A. Alsaig, M. Alsaig, and W. Alhakami, "Design and implementation of a low-cost IoT-based home automation system using Raspberry Pi," Journal of King Saud University – Computer and Information Sciences, vol. 35, no. 3, pp. 101–112, 2023.
7. L. Chen and H. Wang, "PyQt5 in practice: Developing modern graphical user interfaces for embedded systems," Software: Practice and Experience, vol. 53, no. 8, pp. 1650–1668, 2023.
8. A. Gupta and R. Sharma, "A survey on open-source libraries for natural language processing in Python," Journal of Open Source Software, vol. 8, no. 85, Art. no. 5120, 2023.
9. M. Javaid, A. Haleem, and R. Suman, "Internet of Things (IoT) applications for smart homes: A systematic review," Internet of Things, vol. 22, Art. no. 100757, 2023.
10. K. Lee and Y. Zhang, "Developing intelligent virtual assistants with Python: From concept to deployment," Journal of Computational Science, vol. 67, pp. 102–118, 2023.
11. G. Lopez, L. Quesada, and L. A. Guerrero, "Alexa vs. Siri vs. Cortana vs. Google Assistant: A comparison of speech-based natural user interfaces," Advances in Human-Computer Interaction, vol. 2023, Art. no. 7892345, 2023.
12. F. Müller and A. Schmidt, "Raspberry Pi as a platform for IoT prototyping: Performance and limitations," HardwareX, vol. 14, Art. no. e00428, 2023.
13. M. S. Rahman and M. M. Hossain, "Integration of IoT and AI for smart home energy management: A review," Sustainable Energy Technologies and Assessments, vol. 57, pp. 103–120, 2023.
14. P. Silva and A. Costa, "Text-to-speech synthesis: A review of the state-of-the-art with a focus on open-source solutions," Computer Speech & Language, vol. 80, Art. no. 101125, 2023.
15. T. Smith and R. Jones, "A review of infrared communication protocols for home automation," Journal of Sensor and Actuator Networks, vol. 12, no. 2, Art. no. 25, 2023.
16. W. Zhang and X. Zhou, "Web scraping for data acquisition: Techniques, tools, and ethical considerations," Data & Knowledge Engineering, vol. 146, Art. no. 102118, 2023.
17. A. Gupta and R. Sharma, "A survey on open-source libraries for natural language processing in Python," Journal of Open Source Software, vol. 8, no. 85, Art. no. 5120, 2023.
18. IEEE Standard for Pulse Width Modulation (PWM) Control of DC Motors, IEEE Std. 1812-2022, pp. 1–58, 2022.
19. Raspberry Pi Foundation, "Raspberry Pi 4 Model B product brief," 2023 [Accessed on 25/11/2025]. https://www.raspberrypi.com/documentation/computers/raspberry-pi-4.html
20. B. Singh and A. Misra, "Performance analysis of L298N motor driver for precision control of DC motors in robotic applications," International Journal of Robotics and Automation, vol. 39, no. 1, pp. 45–56, 2024.
21. X. Wang and Y. Li, "Concurrency management in Python for real-time IoT applications," Software: Practice and Experience, vol. 54, no. 1, pp. 88–105, 2024.

Author(s) Bio

Khurram Iqbal Currently serving as an Assistant Professor in the Department of Computing, Faculty of Engineering Sciences and Technology, Hamdard University, Pakistan. Additionally, working as a software developer with LA Consulting Corp Software House.
Email: khurramiqbal.nust@gmail.com

Muniba Lodhi from Engr. Muniba Lodhi, Graduate, Department of Electronics, NED University of Engineering and Technology, Karachi, Pakistan.
Email: kmuneeba882@gmail.com

Syed Saad Ali is a passionate engineer and researcher working at the intersection of Electrical Engineering, Artificial Intelligence, and IoT. He contributes to academia and industry through research-driven innovation and student-centered learning.
Email: saad.ali@nhu.edu.pk

Shujaat Ali is a dedicated researcher in the field of Electrical Engineering. In 2014, he earned his Bachelor degree in Electronic Engineering from Hamdard University, Karachi-Pakistan, showcasing early commitment to the field. Building on this foundation, Shujaat Ali pursued Master degree in Electrical Engineering at Hamdard University, Karachi-Pakistan, graduating in 2018. Currently, Shujaat Ali is furthering his academic journey by pursuing a Ph.D. Degree in Electrical Engineering at School of Electrical and Information Engineering (SEIE), Tianjin University, Tianjin. China. Shujaat's research focus revolves around the crucial area of Power Electronics and Renewable Energy, utilizing cutting-edge Electrical Machines and inverters models. His academic trajectory and research interests underscore a commitment to advancing knowledge and addressing contemporary challenges in the realm of electrical engineering, particularly in the context of Power Electronics and renewable energy systems.
Email: shujaat.facho110@yahoo.com

Liaquat Ali is the Chief Executive Officer (CEO) with over 27 years of experience in delivering technology-driven solutions. He believes in results-oriented innovation, ensuring that every product creates measurable value and helps clients achieve sustainable business growth.
Email: info@laconsultingcorp.com

Syed Iqbal Hussain is a Senior Lecturer in the Department of Computing, Faculty of Engineering, Sciences & Technology, Karachi, Pakistan, with a strong focus on quality teaching, applied computing, and academic excellence.
Email: iqbal.hussain@hamdard.edu.pk

Journal of Engineering, Science and Technological Trends (JESTT)

Vol. 3, Issue 1, March 2026
DOI: https://doi.org/10.64060/jestt.v3i1.6

Review

Green-Synthesized Carbon Quantum Dots for Environmental Monitoring of Heavy Metals: A Critical Review of Mechanisms and Performance

Muhammad Arslan Akhtar [1]†, Jalwa Anum [1]†, Abdul Rehman [2] and Rabia [3]

[1]Department of Chemistry, COMSATS University Islamabad, Pakistan
[2]School of Chemical Engineering and Technology, Institute of Molecular Plus, Tianjin University, Tianjin 300072, China
[3]Institute of Molecular Aggregation Science, Tianjin University, Tianjin 300072 China
* Corresponding Email: arslanimran042@gmail.com (M. A. Akhtar), † Equally contributed and share first authorship.

Received: 05 January 2026 / Revised: 13 February 2026 / Accepted: 22 February 2026 / Published online: 01 March 2026

ABSTRACT

The heavy-metal contamination of water bodies is still a crucial environmental issue and a hazard to the ecosystem as well as human health, and incomplete knowledge of how the synthesis of carbon quantum dots (CQD) can regulate the analytical performance of sensing technologies. Despite the benefits of CQDs reported in many studies, systemic linkages between preparation strategy, surface chemistry, photophysical behaviour, and sensing efficiency are yet to be explained well. This review presents a critical argument of the green bottom-up strategies to fabricate CQDs and compares them to the top-down methods in order to understand the way precursor selection, the introduction of heteroatoms, and the control of defects affect quantum yield, emission mechanisms, and environmental friendliness. The special focus is put on the fluorescence modulation mechanisms such as photoinduced electron transfer, Förster/energy transfer, inner filter effects and static versus dynamic quenching and their application in the detection of priority pollutants, including Pb(II), Hg(II), Cu(II), Cr(V) and Fe(III). In addition to publishing literature research, we compare reported detection limits, linear working ranges and selectivity factors to derive general performance patterns. The analysis has shown that controlled surface passivation and functional groups are the final determinants towards sub-micromolar sensitivity and better anti-interference properties. Other issues raised regarding reproducibility, complexity of real-world samples, long-term stability and scalable green production are also addressed. Combining synthesis-structure-property-performance correlations, this review develops empirical design guidelines of the next-generation CQD sensors and explains feasible ways of developing sustainable monitoring and mitigation of heavy-metal pollution in the environment.

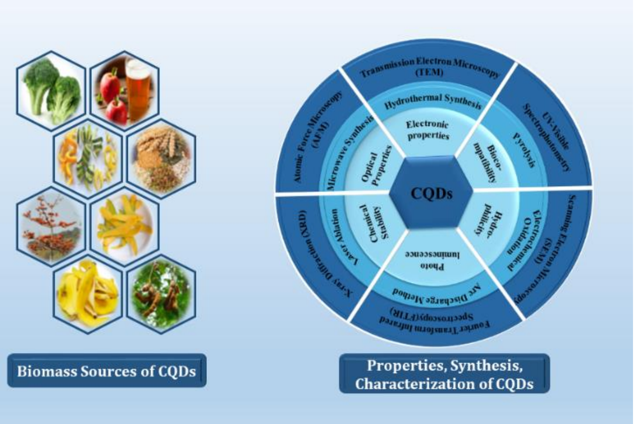

Keywords: CQD: Carbon Quantum Dots; Environmental Monitoring; Fluorescence Quenching; Green Synthesis; Heavy Metal Detection

1. Introduction

Carbon-based nanostructures have emerged as an important class of materials due to their diverse physicochemical properties and broad technological relevance. Materials such as graphene, carbon nanotubes, fullerenes, and nanodiamonds have been extensively investigated [1]; however, their practical implementation is often restricted by intrinsic limitations. In particular, poor aqueous dispersibility and weak visible-region emission hinder the use of graphene and fullerenes, while nanodiamonds suffer from complex synthesis, purification, and size-control challenges [2],[3]. These limitations have driven the search for alternative carbon nanomaterials (NMs) that combine strong fluorescence, water compatibility, and sustainable production. In this context, fluorescent carbon dots have gained prominence as a new generation of carbon-based NMs capable of overcoming the drawbacks associated with conventional carbon nanostructures [4].

Carbon quantum dots CQDs were first discovered by Xu et al. during the purification of single-walled carbon nanotubes (CNTs) [5]. Since then, CQDs have gained significant interest due to their nanoscale size (<10 nm), quasi-spherical morphology, excellent water solubility, and highly tunable photoluminescence [6]. Structurally, CQDs consist of an amorphous or partially crystalline sp^2/sp^3 hybridized carbon core decorated with abundant oxygen- and nitrogen-containing surface functional groups such as hydroxyl, carboxyl, and amine moieties. These surface groups, which vary depending on the precursor and synthesis route, play a crucial role in governing their optical behaviour, solubility, and sensing performance [7].

Compared with traditional semiconductor quantum dots such as CdTe, CdS, and CdSe, which exhibit superior optical properties but suffer from toxicity, high cost, and limited biocompatibility, CQDs offer distinct advantages, including low toxicity, chemical stability, excellent aqueous dispersibility, and compatibility with biological systems [8],[9]. These features make CQDs particularly attractive for environmental and biomedical applications. Furthermore, heteroatom doping (e.g., N, S, P) has been shown to significantly enhance their fluorescence efficiency, charge transfer behaviour, and metal ion affinity [10].

In recent years, increasing emphasis has been placed on the sustainable and green synthesis of CQDs, particularly via bottom-up approaches using renewable biomass precursors. Biomass sources such as plant waste, agricultural residues, algae, animal waste, and industrial by-products provide an abundant, low-cost, and environmentally benign carbon source for CQD production [11],[12]. The inherent presence of heteroatoms and functional groups in biomass facilitates carbonisation and surface passivation without the need for harsh chemicals. CQDs derived from biomass exhibit excellent biocompatibility, non-toxicity, and photostability, making them superior alternatives to chemically synthesised counterparts [13],[14].

Among the various applications of CQDs, heavy metal ion sensing has emerged as one of the most extensively explored areas. Owing to their strong fluorescence, high quantum yield, and surface-rich functional chemistry, CQDs enable sensitive and selective detection of toxic metal ions even at trace levels [15],[16]. Their excellent photostability ensures reliable signal output, which is essential for accurate monitoring of water quality. However, challenges such as post-synthetic functionalization, purification complexity, and detailed structural characterisation remain and must be addressed for large-scale deployment [17].

Photoinduced electron transfer, energy transfer routes and inner filter effects are often the most popular ways of mechanistically interpreting fluorescence modulation, and are often described independently of structural evidence. This means that practical design guidelines towards creating a dependable and repeatable CQD sensor are yet to be developed.

This review highlights recent advancements toward the sustainable production of fluorescent CQDs, with a primary focus on eco-friendly bottom-up synthesis routes, including hydrothermal, microwave-assisted, and carbonisation methods using biomass precursors. In addition, the review critically discusses the application of CQDs as fluorescent probes for selective heavy metal detection in aqueous medium, emphasising sensing mechanisms, material performance, and prospects in environmental remediation.

2. Synthesis of CQDs

After Xu and his colleagues' accidental discovery of CQDs in 2004 during the purification of single-walled carbon nanotubes, different methods have been introduced to synthesise CQDs, as shown in Figure 1 [18] (Table 1). These approaches can be categorised as Top-down and Bottom-up. The top-down approach involves the production of Nano-sized particles through the breakdown of larger carbon precursors like graphene, ash, or soot via arc discharge [19], chemical oxidation, laser ablation [20], electrochemical oxidation, etc. Unfortunately, this method has some disadvantages, such as the need for pricey components, difficult reaction conditions, and a lengthy reaction time. Likewise, the ‘‘bottom-up’’ methodology generates CQDs from less expensive precursors utilising straightforward experimental setups, negating the need for complex methods and expensive precursors [21]. The bottom-up refers to the process of creating

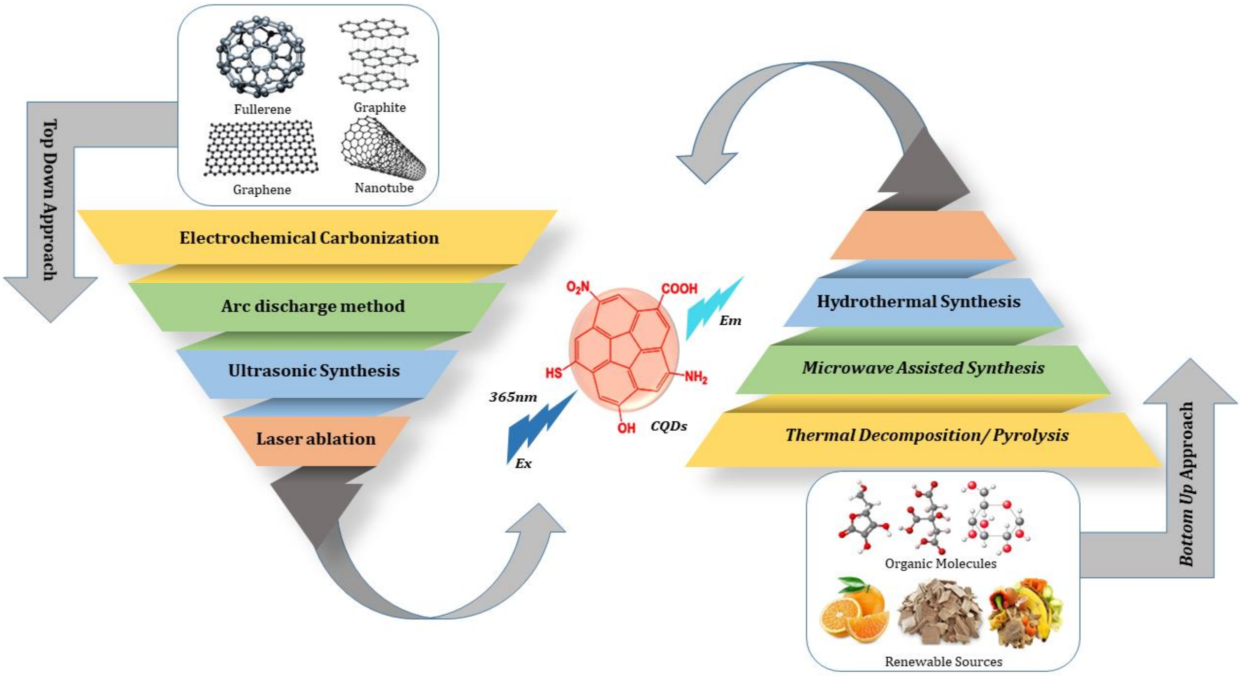

Figure 1: *Carbon Quantum Dot Fabrication via Top-Down and Bottom-Up Strategies*

huge nanostructures using energy from smaller carbon components such as amino acids, polymers, carbohydrates, and waste materials combined to form CQDs via chemical reactions, such as hydrothermal reaction, chemical solution synthesis, pyrolysis, microwave assistance, ultrasonic methods, and template-based routes or plasma treatment [22].

Choosing appropriate carbon precursors is the initial stage in the bottom-up process, and it directly impacts the properties of the final CQDs. In the second stage, the chosen carbon precursor is carbonised, and any impurities that may have formed during the carbonisation process are then purified. Precursors with carboxyl and hydroxyl functional groups on their surface are appropriate for the production of CQDs. schematic representation of various routes The scientific community has taken notice of the green approach to the CQDs synthesis because of its non-hazardous character. Utilising green resources as a carbon source is necessary. The raw materials and synthesis techniques significantly influence the features of colloidal quantum dots, such as size, colloidal stability, compatibility, functional groups, fluorescence properties, quantum yield (QY), and crystallinity. The green methods for creating CQDs are covered in the following section. The carbonisation, hydrothermal, and microwave-aided processes are mostly explored to synthesise CQDs from green precursors, primarily biomass as the raw material [23].

3. Transition to Green Synthesis Methods

This section focuses on the eco-friendly approach towards the fabrication of CQDs. These environmentally friendly methods not only solve environmental issues but also reduce the presence of toxic components, improve environmental and public health safety, employ a low-cost synthesis procedure, and promote sustainability.

3.1. Hydrothermal Method

Hydrothermal synthesis is one of the most frequent, non-toxic, and affordable ways to prepare CQDs. It is primarily a solution-reaction-based method that utilises precursors such as biomass saccharides, organic acids, juices, and waste peels. The primary benefit of this method is that it is a reasonably easy and 'green' process, making it environmentally benign and less harmful, with an evenly sized distribution of synthesised CQDs that are extremely efficient [24]. In a simple one-step hydrothermal process, the target precursor solution is heated in an autoclave reactor with Teflon lining to conduct the hydrothermal reaction at high pressure and high temperature, as shown in Figure 2 [25]. HTC has been reported for the synthesis of self-passivated fluorescent CQDs in one step using reagents such as glucose, citric acid, ascorbic acid [26], biomass waste (mango peels, soy milk, broccoli [27], lemon juice, banana peel [28], honey-comb, cambuci juice [29], starch [30], cellulose [31] and paper as carbon source [32]. The reaction can be carried out in an aqueous or organic solvent. Solvothermal carbonisation with subsequent organic solvent extraction is a prevalent method for synthesising CQDs. Carbon precursors are thermally treated in high-boiling-point solvents, then extracted and concentrated. Bhunia et al produced hydrophobic and hydrophilic CQDs under 10 nm from carbohydrates. Hydrophobic CQDs were synthesised by heating a carbohydrate, octadecylamine, and octadecene mixture at 70-300c for 10-30 minutes. Hydrophilic CQDs were generated by heating an aqueous carbohydrate solution across various pH levels or with phosphoric acid at 80-90c for 60 minutes [33]. Lu, Zifan, et al. prepared n-CQD with yellow-green fluorescence by surface functionalization of CQDs via solvothermal method. The prepared N-CQDs showed a considerable QY (5.11%) and high chemical and optical stability. More importantly, N-CQDs showed good selectivity and sensitivity to Ag^+ at the concentrations of 0–10 μM and 10–30 μM, respectively. N-CQDs were used to detect the content of Ag^+ in food packaging material [34]. Singh, Harpreet, et al. proposed fluorescent CQDs from cabbage (2-4 nm), whose fluorescence was suppressed upon reaction with Fe^{3+}, Pb^{2+}, and Hg^{2+} ions [35]. These CQDs work well for heavy metal detection, although more research work is required to improve selectivity and quantitative analysis. Functionalizing CQDs with specific ligands

Table 1
Advantages and disadvantages of Top-Down and Bottom-Up approaches [21]

Methods	Advantages	Disadvantages
Top-down	• Raw materials are used efficiently by breaking down carbon sources into smaller fragments • Utilizes readily available and inexpensive carbon sources like carbon nanotubes, graphite, and carbon soot. • Controls size, shape, and surface functionalities of CQDs by selecting precursors and reaction conditions. • One-step manufacturing can control over size of the nanostructure with excellent product quality.	• Thus, severe conditions of the reaction, for example, using large concentrations of acids or oxidants, high temperature, and long-time of reaction • Newly produced CQDs have poor control over their size distribution and surface functionalities. • Such a pattern may produce structural defects and impurities, while the synthesis procedure’s batch nature may hinder scalability. • One disadvantage is that there may be some oxidation or by-product formations and hence the final product may be contaminated.
Bottom-up	• Reaction conditions are milder than top-down methods, which typically involve microwave or hydrothermal processes. • Nanostructures with fewer defects and a more uniform chemical composition. Heteroatoms can be introduced during synthesis. Potential for large-scale production, high reproducibility, simple processes, improved performance, and environmentally friendly characteristics	• The task here is to attain homogeneity in size and at the same time manage surface activity. • The top-down methods are elaborate and provide a restricted number of carbon sources to work on.

may enhance their specificity [35]. Nan, Zhezhu, et al. effectively created a detection method for Ferric iron (Fe (III)) using CQDs modified ZnO/CdS nanoparticles. The interaction between Fe(III) and CQDs/ZnO/CdS NPs led to efficient fluorescence quenching. Moreover, the Fe(III) detection limit was determined to be approximately $1:72 \times 10^{-7}$ M. [36] Khan, Zubair MSH, et al. successfully synthesized blue fluorescent NCQDs with a quantum yield of 13.2%. this N-CQDs works as a nanoprobe sensor for selective and sensitive detection of Fe^{3+} with as low as 0.10 μM concentration of Fe^{3+} can be detected in the linear range of 2–20 μM. [37] Similarly, Aygun, Aysenur, et al. synthesize CQDs doped with heteroatoms such as sulfur, nitrogen, and boron (N-CQD, B-CQD, and S-CQD) with average sizes in the range of 5–7 nm as colorimetric sensors for heavy metals successfully. It was observed that CQDs detected Fe^{3+} metal ions, B-CQD and S-CQD detected Fe^{3+} and Ag^{+} metal ions, and N-CQDs detected Ca^{2+} metal ions with different LOD values for different metals [38]. Kolaprath, Mrinalini Kalyani Ayilliath, Libina Benny, and Anitha Varghese. Synthesized CQDs from the leaves of Polyalthia longifolia (a natural source) through a one-step hydrothermal method with a QY of 22% and an average size of 3.33 nm. The p-CQDs showed high sensitivity, selectivity, and a low detection limit of 2.4 nM for the determination of Cd^{2+} ions [39].

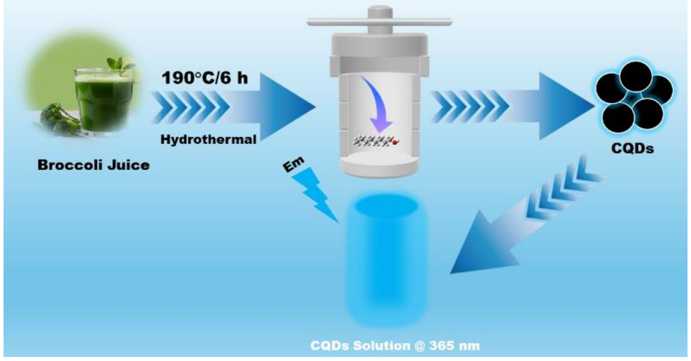

Figure 2: *Biomass-Derived CQDs: Hydrothermal Transformation of Broccoli Juice* [27]

3.2. Microwave Assisted Synthesis

Microwave pyrolysis, which is one of the satisfactory and efficient bottom-up methods, has been used for synthesising CQDs. This technique entails applying high-energy microwave radiation to initiate standard chemical reactions by breaking up chemical bonds and creating the CQDs owing to the microwave's ability to heat all chemical samples uniformly [40]. Microwave synthesis is a rapid and fairly economical method of synthesising CQDs by microwave heating, as depicted in Figure 3. The process is quite simple and economical in terms of time since it improves the quantum yield of CQDs relative to the other methods [41]. Different studies reported the synthesis of CQDs by this method. An efficient and controlled synthetic approach of carbon dots has been reported using branched polyethyleneimine and citric acid, which were employed to change the internal structure [42]. Such a system supports the versatility of carbon dots that could be developed easily by facile fabrication methods, combining catalytic properties and photoluminescence. Nazar, Muhammad, et al. synthesised CQDs via a pot microwave-assisted heating method from activated carbon of arabica coffee waste with a size of 10.12 nm and a quantum yield of 6%, performing as a selective fluorescent detector for Fe^{3+} ions, with a detection limit of 0.27 μM [43]. Architha, Natarajan, et al. synthesised CQDs from the Plectranthus amboinicus (Mexican Mint) leaves via the microwave-assisted reflux method with a QY of 17% and an average diameter of 2.43 nm and used a fluorescent probe for Fe^{3+} ion detection with LOD of 0.53 μM in the concentration range of 0–15 μM. CQDs prepared showed excellent properties in terms of detection of Fe^{3+} ions and biological applications [44]. Chugh, Riya, and Gurmeet Kaur, et al. successfully prepared CQDs-Ag NCs with the average sizes of orange peels mediated CQDs around 5–8 nm, which showed great potential in precision agriculture and bactericidal applications [45]. Zaman, Alif Syafiq Kamarol, et al. successfully synthesised CQDs from empty fruit bunch EFB biochar for the sensitive and selective detection of Cu^{2+} ions, which showed a concentration range of 0–400 μM, acting as a fluorescent sensor [46].

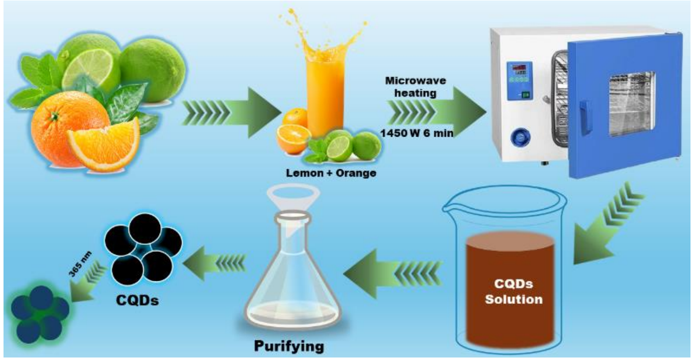

Figure 3: *Biomass-Derived Highly Luminescent CQDs via Hydrothermal Carbonisation of Lemon* [47]

3.3. Microwave Assisted Synthesis

The carbonisation method of CQD synthesis uses organic precursors such as glucose or citric acid and heats the precursors at temperatures between 200 °C and 900 °C in an inert or low-oxygen atmosphere. This process includes the thermal decomposition of carbon precursors to produce carbon nanoparticles of definite characteristics based on the temperature, time, and type of precursor, as illustrated in Figure 4. This cheap technique can easily control the size of the CQDs for uses in bioimaging, sensing, and optoelectronics. Suppan, Thangamani, Rama Ranjan Bhattacharjee, and Moorthi Pichumani. prepared Fluorescent 'turn-on' porphyrin CQD nanoprobes for selective sensing of heavy metal ions. Porp-CQDs have an average particle size of 2.4 nm and sensed the Zn^{2+} ions in bore well water analysis with LOD of 75 μM [48]. Kaur, Rajdeep, et al. reported the synthesis of (AgNPs-CQDs) nanocomposite from *Syzygium cumini* leaves by pyrolysis treatment with an average diameter of 4.0 nm for Hg^{2+} ions detection, which was demonstrated as an outstanding colourimetric sensor for mercury detection over wide PH ranges [49]. Kumari, Archana, et al. prepared green fluorescent CQDs waste polyolefins residue for Cu^{2+} ion in real water samples, having QY of 4.84% with LOD value of 6.33 nM and linear detection range of 1–8.0 M. Prepared CQDs also showed potential for cancer cell imaging [50].

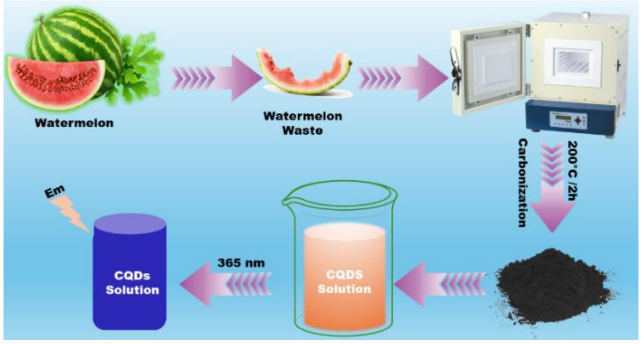

Figure 4: *Schematic illustration of the synthesis of water-soluble fluorescent CQDs from watermelon peels* [51]

4. Comparison of synthesis methods of CQDs

Several techniques are used to prepare Carbon Quantum Dots, and each technique comes with advantages and disadvantages depending on the application of CQDs. The top-down methods include laser ablation and electrochemical oxidation, while the bottom-up methods include hydrothermal/solvothermal, microwave-assisted, and pyrolytic synthesis [22]. Top-down techniques can be achieved by breaking down larger carbon structures into smaller units, typically highly crystalline CQDs. Nevertheless, these methods may be energy-consuming and imply the usage of highly specialised equipment [52]. On the other hand, the bottom-up approach builds up the CQDs from molecular precursors and they provide more control over the size and surface characteristics of the dots [21],[22]. Of the above methods, it is hydrothermal to convert the organic materials into CQDs, where water acts as a solvent under high temperature and pressure. This method is widely appreciated due to its benefits, such as simplicity in the synthesis process, being cheaper as compared to other techniques, and the ability to synthesize CQDs with desirable optical characteristics. Microwave-assisted synthesis, another bottom-up approach, significantly reduces the reaction time by providing heat evenly and rapidly, although the particle size distribution may not always be uniform [53]. Pyrolysis is another common technique characterized by a high yield of CQDs but its reaction conditions might be more demanding and critical for getting uniform and high quality of CQDs. Thus, the type of synthesis of the CQDs depends on the purpose, required characteristics, costs, and environmental friendliness of the method, as each offers a trade-off between accuracy and yield [54] (Table 2).

Table 2
Comparative Analysis of Synthesis Methods of CQDs.

Synthetic Methods	Advantages	Disadvantages	Ref.
Chemical Ablation	Highly efficient, Most Accessible Surface functionalization	Hazardous byproducts, Requires careful handling Poor control over size	[55]
Electrochemical Carbonization	stable and one-step method, mild conditions	High energy consumption, complex setup	[56]
Laser Ablation	Precise control over the size, rapid, tunable surface states	Complex laser system, Low Quantum yield	[56]
Hydrothermal Treatment	Eco-friendly, economical, non-toxic, easy procedure	Poor control over size, Risk of explosions	[57]
Microwave Assisted	Cost-effective, rapid, and desired morphology can be obtained	poor control over size,	[57]
Pyrolysis	Produce good products High yield, thermal stability	Controlled atmosphere, High-temperature requirement	[58]

4.1. Microwave Assisted Synthesis

CQDs are formed by sheets of graphene or derivate graphite. These dots have a high surface area-volume ratio as well as sp^2 hybridisation of the crystalline core and non-crystalline phases with surface functional groups [59],[60],[61],[62]. Tang et al. discovered that carbon quantum dots (CQDs) have core-shell structures, which can be either amorphous (mixed sp^2/sp^3) or graphitic crystalline (sp^2), depending on the extent of sp^2 carbon occurrence in the core [63]. Several researchers reported the graphitic crystalline core of CQDs, as can be seen in Figure 5 [64],[65]. The cores are classified based on the synthesis technique, precursors, and other parameters [66]. These cores are very small, ranging from 2-3 nm with a lattice spacing of ~0.2 nm [67]. At temperatures above 300°C, the structure becomes graphite-like (sp^2), while lower temperatures result in amorphous cores unless there is a presence of sp^2/sp^3-hybridised carbon in the precursor [68]. To determine the core structure of CQDs, various instrumental techniques such as Transmission Electron Microscopy (TEM) or High Resolution (HR) TEM, Scanning Electron Microscopy (SEM), Raman spectroscopy, and X-ray diffraction (XRD) are utilised. TEM and SEM (FESEM) are usually carried out to measure CQDs' size and morphology [69]. SAED and XRD patterns reveal the crystalline or amorphous nature of CQDs. The same selected area electron diffraction (SAED) pattern is observed for CQDs passivated by polyethylene glycol (PEG200N) via laser ablation, which corresponds to the planes of the diamond structure [70]. The HRTEM image reveals varying lattice spacing ranging from 0.2-0.23 nm. The wide peak at 2θ 23° suggests that the CQD has an amorphous characteristic, whereas the presence of two wide peaks at 2θ 25° and 44° indicates a low-graphitic carbon structure similar to (002) and (100) diffraction [71]. The composition and functional groups on the surface of CQDs are analyzed using techniques such as FT-IR spectroscopy, XPS and NMR [7].

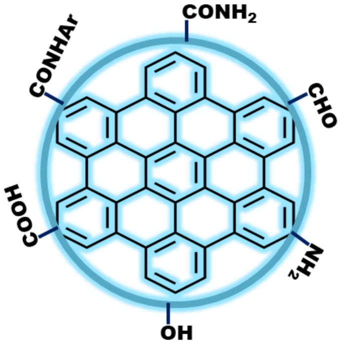

Figure 5: *Structure of CQDs*

Recent research has focused on studying fluorescent carbon quantum dots (CQDs) for multi-ion sensing and bio-imaging applications. Arumugham, Thanigaivelan, et al. discovered that CQDs derived from Catharanthus roseus leaves demonstrated carboxylic functional groups on their surface and contained major exciting elements such as carbon (C, wt. 98.14%), oxygen (O, wt. 0.73%), and nitrogen (N, wt. 1.13%) from the EDX spectrum as support for the FT-IR result [72].

The zeta potential is used to determine the positive or negative charge on the surface of CQDs and the level of electrostatic interaction between them [73]. Kolanowska, Anna, et al found that Lys- and Cys-CQDs had the highest zeta potential values, providing excellent stability in water [74]. In highly acidic conditions, most amine groups were protonated, resulting in an overall higher positive surface charge. Conversely, in alkaline conditions, the zeta potential remained highly negative, indicating the presence of stable anions for all CQDs.

5. Properties of CQDs

Carbon quantum dots exhibit diverse and tunable physicochemical properties that make them highly attractive for advanced technological applications. Their behaviour is strongly influenced by size, surface functional groups, doping elements, and synthesis conditions. This section discusses the fundamental optical, photoluminescence, and electronic properties of CQDs along with their characterisation aspects.

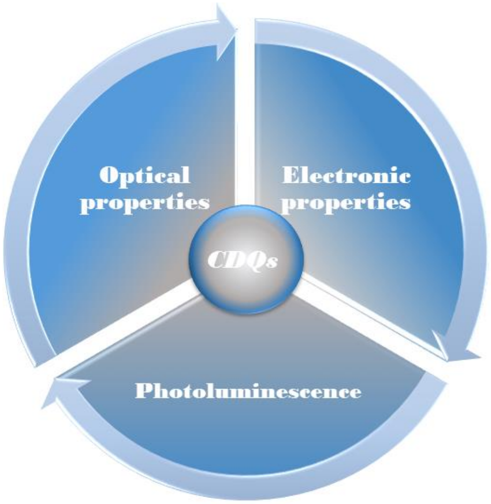

Figure 6: *Properties of CQDs*

5.1. Optical Properties

Carbon quantum dots have unique optical characteristics, making them very useful in sensing, imaging, and photonics applications. Out of all the varieties of CQDs, they exhibit high and size-tunable photoluminescence, where the size, the type of surface groups, and the synthesised conditions could help in adjusting the luminescence properties [75]. Carbon dots commonly demonstrate significant absorption in the ultraviolet range (230-400 nm), with some absorption bands extending into the visible spectrum [76]. The π-π* transition of the C=C bond produces the distinctive peak at 260-320 nm, while the n-π* transition of the C=O bond accounts for the shoulder peak at 270-390 nm [77]. Modifying the surface through passivation or functionalization can alter the UV absorption properties of carbon dots by enhancing their absorption peaks or shifting their absorption wavelengths towards the red end of the spectrum, referred to as quantum confinement [78].

Quantum yield and fluorescence intensity in carbon quantum dots (CQDs) are linked, with intensity increasing as quantum yield rises. Surface passivation [79] and doping [80] are key factors influencing quantum yield. Additionally, fluorescence is affected by particle size, pH level, and surface functional groups [81]. Surface passivation using 1-ethyl-3-(3-dimethyl aminopropyl)-carbodiimide (EDC) can significantly increase the fluorescence intensity of CQDs. The fluorescence intensity increases with the amount of EDC, reaching a maximum at 25 mM concentration, with the quantum yield increasing from 18.83% to 41.10% [82]. Highly passivated green phosphorus-nitrogen co-doped CQDs with a 25% quantum yield were prepared by Omer. CQDs can detect Cu^{2+} ions at concentrations as low as 1.5 nM [83]. Wang synthesised CQDs with a 53% quantum yield using a solvothermal method. Using citric acid as a precursor and 1-hexadecylamine as a surface passivator [84]. Inorganic salts such as ZnS and TiO_2 can be used to dope carbon quantum dots (CQDs) to enhance fluorescence quantum yield along with surface passivation [85]. Anilkumar successfully raised the quantum yield of CQDs doped with inorganic salts and surface passivation, with ZnS-doped CQDs reaching a 78% quantum yield and TiO2-doped CQDs achieving a 70% quantum yield [86]. Additionally, nitrogen/sulfur co-doped CQDs were produced with a quantum yield of up to 73.1% using citric acid and thiourea as reaction precursors in a hydrothermal approach. These CQDs could be used as fluorescent probes for detecting uric acid [87].

Various methods of creating doped carbon quantum dots (CQDs) have been explored in recent studies. Bourlinos utilised microwave heating to produce nitrogen/boron co-doped green fluorescent CQDs using citric acid, boric acid, and urea as a source [88], while Zhou employed the solvothermal approach to create phosphorus-doped CQDs with a 25% fluorescence quantum yield hydroquinone and phosphorus tribromide as a carbon and phosphorus source [89]. These findings indicate that doping CQDs with specific electron groups and heteroatoms can significantly alter their luminescence properties, making them particularly valuable for various applications.

In synthesising CQDs, adjusting the synthesis conditions can alter their physical and chemical properties, such as particle size and surface chemical composition, affecting their energy level structure and photochemical properties [90]. By modifying the concentration of alkali [90] and using oxidising or reducing reagents during synthesis, the chemical composition of the surface can be adjusted, leading to changes in the photochemical properties of CQDs [91].

Carbon quantum dots have high light absorption capability and can extract light at difficult and complex wavelength ranges. This characteristic is most useful for applications in solar cells and photocatalysis since there is a need for the material to absorb light of many wavelengths [92]. For instance, surface passivation can enhance the fluorescence quantum yield and stability greatly. However, it is possible to modify these properties with simple and cost-effective synthesis approaches of CQDs, thus making them applicable in the progression of the bioimaging, optical sensing, and energy conversion science fields [17].

5.2. Photoluminescence

Research on the photoluminescence (PL) of CQDs) has experienced significant growth in recent years. This property has been particularly valuable in the field of photocatalysis [93]. The PL emission of CQDs follows the Stokes type emission, meaning that the emitted wavelength is longer than the excitation wavelength; several literatures reported this [94],[95]. In the analysis of emissions and structural features, most observed PL emissions can be categorised into bandgap transitions related to p-domains and origins associated with defects in graphene structures. These categories are often interconnected as the creation of p-domains is based on the manipulation of defects in graphene sheets [96]. In a plethora of studies, the correlation between PL emission and excitation wavelength (ʎex) of CQDs has been extensively discussed. Sun et al. noted that fluorescent CQDs, modified with polyethylene glycol (PEG1500N) or propionyl ethyleneimine co-ethyleneimine (PPEI-EI), exhibit distinct emission patterns based on the excitation wavelength [97].

Carbon quantum dots were synthesised hydrothermally by Ding et al., using urea and then separated via silica column chromatography. The CQDs exhibited a single peak in the photoluminescence excitation spectrum and the excitation-independent PL emission spectrum. Additionally, they displayed similar monoexponential fluorescence lifetimes. The absorption curves and PL emission spectra under different light wavelengths are depicted in Figure 6.

In the latter case, it was found that the fluorescence change in CQDs) is mainly influenced by surface functional groups [98], which create energy potential traps mostly led by sp2 and sp3 hybridised regions [99]. The defect-derived fluorescence of doped

CQDs is attributed to the localised electron structure of electron-hole pairs in the sp^2 state, and the fluorescence quantum yield can be significantly increased through doping [100]. It was also discovered that modifications to surface groups have a significant effect on the fluorescence emission of CQDs [101]. This indicates the potential for enhancing the optical properties of CQDs through surface group modifications.

Fang, Li-yang, and Jing-tang Zheng. Conducted a study using hydrothermal synthesis to produce C-dots-160 and C-dots-200 at temperatures of 160°C and 200°C. The research aimed to understand the relationship between microstructure and fluorescence emission behaviour of CQD-dots. It was found that higher synthesis temperatures led to the addition of more oxygen and nitrogen atoms, increasing structural flaws and altering their concentration ratio. Consequently, C-dots-200 exhibited stronger fluorescence emission [102].

Certain carbon dots possess up-conversion photoluminescence characteristics [103],[104] which involves the release of light with a shorter wavelength after absorbing two or more photons with a longer wavelength. This process is characterised by the emission of light at a higher energy than the absorbed photons [105]. Cao et al. demonstrated in their study that CQDs) produced through laser ablation exhibit strong luminescence with two-photon excitation in the near-infrared at 800 nm, suggesting the presence of up-conversion photoluminescence (UCPL) properties [103].

5.3. Electronic Properties

The synthesised CQDs) possess remarkable electrochemical features that qualify them to be used in sophisticated technologies, for instance, optoelectronic [106],[107], and energy storage technologies [108],[109] among others. The first of the most prominent electronic features of CQDs is their size and shape-tunable bandgap. This tunable bandgap also helps CQDs to enable them to extend from the intrinsic characteristic of bulk carbon materials to act like other regular semiconductor CQDs for use in electronic and photonic applications [110],[111]. Also, CQDs possess high electron mobility, which is desirable in the application of the material in electronic circuits and devices. This high electron mobility is attributed to the sp^2 hybridised carbon networks carved in the CQDs, which offer efficient paths for electron transport [112]. Carbon Quantum Dots CQD in the electron transport layer with TiO_2 accelerate the efficiency of perovskite solar cells by up to 19%. This enhancement is because CQDs offer higher electron mobility and decreased charge recombination compared to the control. This CQDs/TiO_2 composite also allows for achieving greater stability and reproducibility of cells. This approach shows that the CQDs can enhance the performance of the photovoltaic devices [113]. Besides, CQDs demonstrated specific features of charge accumulation, which could be quite appealing for application in supercapacitors [114] as well as batteries [115]. Due to a large surface area to volume ratio and high electrode materials' rate capability, it is possible to charge them to store energy and quickly discharge [116]. Surface functionalization of CQDs can increase their electronic characteristics by appending appropriate functional groups that will increase conductivity and interface compatibility with other materials. For example, when nitrogen or sulfur is doped into CQDs, it will cause a great change in their electronic structure concerning the effect of enhanced charge transfer and electrical conductivity [114]. The electronic properties' multiple and tunable nature and their synthesis method's simplicity and eco-friendly nature make CQDs an ideal candidate to bring about the next generation of electronic, optoelectronic, and energy storage devices [117].

6. Methods used for characterisation of CQDs

To describe CQDs, many techniques are used for characterising as well as examining the properties of Carbon Quantum Dots. With the help of TEM, SEM, XRD, and AFM characteristics of structural properties, including the size of particles and the surface morphology and crystalline structure, are observed. In properties of light interaction, UV-Vis spectroscopy (200–800 nm) is used to understand absorption and PL Spectroscopy (200–1000 nm) for fluorescence and decay.

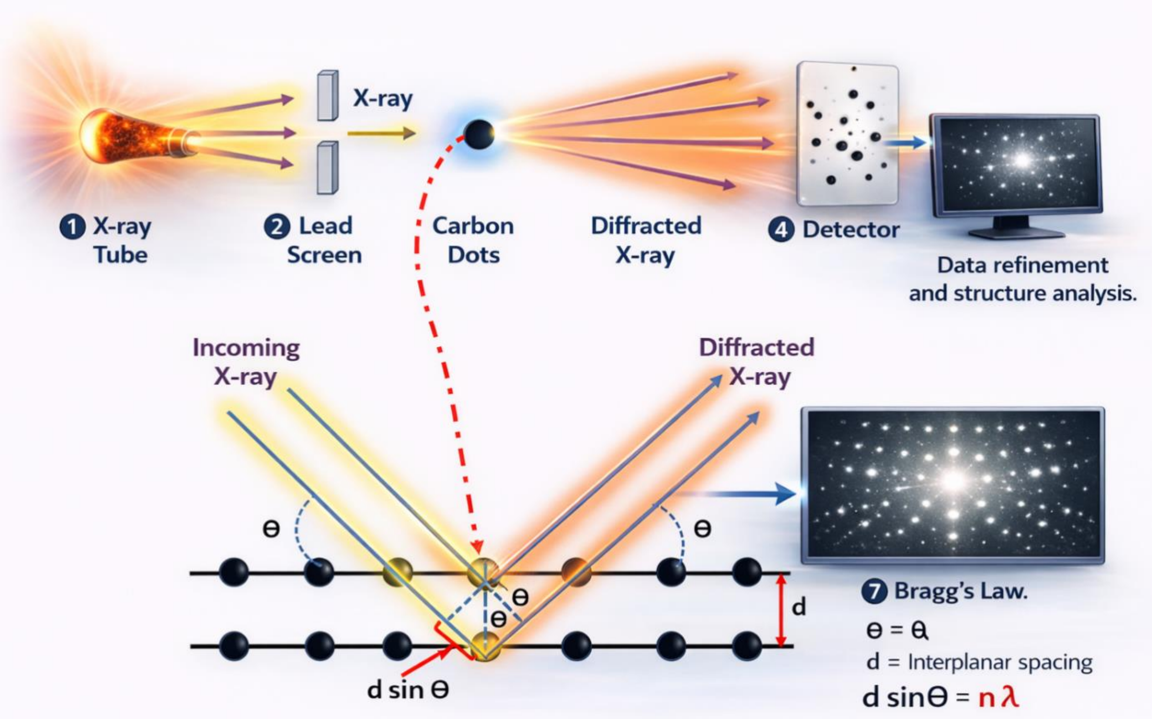

Figure 7: *Schematic representation of X-ray diffraction showing the interlayer spacing (d) and the incident/diffracted angle (θ) of X-rays according to Bragg's law*

Functional groups and components are determined with FTIR, XPS, Raman, and EDX. Zeta Potential Measurement and DLS are used to analyse and measure surface characteristics of the charge and stability, respectively. DSC is complemented by TGA and NMR Spectroscopy for further information on thermal stability and information about the molecular structure [118].

6.1. Morphological Analysis using TEM/ SEM

The utilisation of scanning electron microscopy (SEM) and transmission electron microscopy (TEM) in CD visualisation is widely acknowledged by researchers. In the comparison between SEM and TEM for imaging CQDs, SEM uses a focused electron beam to scan the surface and obtain information on surface topography and composition, while TEM is more precise for measurements smaller than 1–20 nm due to its higher resolving power, making it better for identifying small-sized particles [119]. TEM utilises high-energy electron beams to transmit through the sample for imaging. TEM has been used to investigate the morphological evaluation of CQDs, including their nanostructure and size down to the quantum scale, with an average size of 2-12 nm [120],[121],[122]. Based on a recent report, CQDs showed nearly spherical and uniformly sized particle indicating the crystalline nature of the prepared CQDs [69]. The inter-layer spacing and average crystallite size of CQDs were found to be around ~1.8 Å and 1.9 nm, respectively. Cheng et al. used the HRTEM technique to identify that the average size of CDs was 3.4 nm. Their HRTEM images revealed that the CD particles appeared in quasi-zero dimension and were highly crystalline, with a size distribution ranging from 1 to 10 nm [123]. The carbon nanostructures displayed uniform particle size distribution and minimal aggregation, with an average diameter of 7.89 nm based on the Gaussian fitting curve. This was determined by measuring around 200 particles, indicating nano-sized characteristics. In another report, the study analyzed the size distribution of C-CQDs from TEM images, finding sizes ranging from 2-12 nm with an average size of 5 nm. The C-CQD structure exhibited crystallites on the surface/edge and in the core, indicating mixed-phase growth [124]. The average size of 18-20 nm CQDs was identified by Baslak, Canan, et al. via the HRTEM technique. HR-TEM showed that the shape of the synthesised CQDs was almost quasi-spherical, with an essentially amorphous core structure and no crystal lattice. DLS analysis also confirmed the TEM images [125].

6.2. Structural Analysis using XRD

Regarding the structural characterisation of CQDs, X-ray diffraction (XRD) is a vital method. It allows us to determine whether the CQDs are crystalline and to analyze their phase composition. The diffraction patterns provide information about interlayer spacing, crystallite size, and the level of graphitisation as depicted in Figure 7 [110]. Typically, the diffraction band at 2θ = 20–30° is attributed to the amorphous structure of CQDs, while sharp bands indicate crystalline clusters [111],[112]. In a study by Singh, Arvind, et al., self-functionalized luminescent CQDs were prepared through nanosecond laser irradiation. XRD analysis showed that these CQDs exhibited weaker, broader diffraction peaks at around 22.5°, with a d-spacing of approximately 0.4 nm, compared to the (002) plane of highly crystalline graphitic microcrystals at about 26.5° with a d-spacing of roughly 0.35 nm. This suggests a polycrystalline nature, likely caused by oxygenated groups. The peak width increased as the particle size decreased [112]. Fluorescent CQDs were also produced from sugarcane bagasse pulp using a chemical oxidation and exfoliation process. The XRD analysis identified characteristic peaks at 2θ = 11.4°, 20.6°, 22.8°, 42.3°, and 45.7°, with prominent peaks at 20.6° and 42.3°, indicating the presence of graphitic carbon. Additionally, SAED patterns and XRD peaks confirmed that the CQDs possess a face-centred cubic crystal structure matching carbon's diffraction pattern. The observed interlayer spacing aligns with the (311) plane of carbon [113].

The Debye-Scherrer formula was used to calculate the average grain size of prepared CQDs by selecting the highest peak value shown in the XRD diffractogram (1).

$$D = \frac{K\lambda}{\beta \cos\theta} \qquad (1)$$

In the previously mentioned equation, $\boldsymbol{D}$, $\boldsymbol{K}$, $\boldsymbol{\theta}$, $\boldsymbol{\beta}$ and $\boldsymbol{\lambda}$ represent the dimensions of the carbon quantum dot, k refers to the constant shape factor within the range of 0.89–1, with a value of 0.9 in this particular study [126], the measured diffraction Bragg angle in degrees, β is the full width at half maximum denoted as FWHM and measured in radians, and λ is the wavelength of the X-ray source, which is 0.15406 nm (Cu$k_\propto$ radiation), respectively. By utilising the equation, the average grain size of the prepared quantum dots was 2 nm and 4 nm.

XRD is crucial for identifying the key characteristics of crystallite-structured C-dots, but it is not suitable for analysing amorphous C-dots. Such structural information is important for understanding the electronic properties of CQDs in fluorescence sensing and photocatalytic fields.

6.3. Morphological Analysis using AFM

Innovative tools like Atomic force microscopy (AFM) are useful in the characterisation of Carbon Quantum Dots and help in the determination of surface morphology and topographical features. AFM offers very accurate measurements of the size, height, and lateral dimensions of CQD particles, which are important when determining the distribution of the sizes of these particles as well as the roughness of the surface. In the same vein, AFM determines the aggregation state of the CQDs and evaluates stiffness as well as adhesion coefficients of the material at the nanoscale. This characterisation provides a detailed, comprehensive profile of CQDs that will enable researchers to enhance fluorescence sensing and photocatalysis applications of CQDs with the best understanding and performance.

AFM works on a setup where a fine tip is placed at a very close distance from the sample material in the form of a flexible lever. The idea of AFM relies on force interactions between the tip and the sample or the surface of the specimen [127]. When the tip scans along the surface, forces such as the van der Waals force the cantilever to bend. A laser beam is reflected off the cantilever, which records these deflections using a photodetector. The collected data is then analysed to produce full-scale, three-dimensional representations of the sample surface [128]. This method enables AFM to offer topographical information and other physical properties at a nanoscale, which makes it productive for characterising nanomaterials such as CQDs. The research used AFM images to measure the size and roughness of the synthesised CQDs. The CQDs were observed to be spherical and very small, with average diameters ranging from 3 to 5 nm and surface roughness of less than 5 nm [129]. The images in Figure 4 illustrate the random arrangement of the CQDs on a silicon wafer substrate at low magnification and provide high magnification images as well as a 3D image with corresponding 2D images. The histogram of the CQDs indicated an average roughness of 4.2 nm and a size ranging from 3 to 5 nm [129].

6.4. Optical Analysis using UV/Vis Spectroscopy

The optical absorption of carbon quantum dots (CQDs) is excellent in the 260 to 320 nm UV range, extending into the visible region. Pure CQDs typically show two absorption peaks, one for the π-π* transition of aromatic sp^2 domains and one for the n-π* transition of surface functional moieties like carbonyl, hydroxyl, ester, and carboxyl groups [94]. However, the position of these peaks heavily relies on the CQDs' synthetic method and the nature of their surface groups [130]. General instrumentation of Uv-Vis spectroscopy is shown in Figure 8.

The optical properties of CQDs are significantly affected by their size, shape, and surface functionalization, leading to shifts in absorption peaks as the size decreases. Additionally, surface functional groups can impact the electronic structure, altering the absorption characteristics. UV–visible spectroscopy is crucial in determining the optical bandgap of CQDs, which is essential for assessing their potential applications in optoelectronic devices [131].

UV-visible spectroscopy is crucial for determining the bandgap of CQDs, which indicates their semiconducting nature and suitability for electronic applications. The absorption spectra provide insights into the behaviour of CQDs under different conditions by indicating variations in size, aggregation, or surface chemistry. The bandgap energy can be precisely determined through meticulous preparation and analysis, enabling a systematic procedure. The construction of a Tauc plot aids in enhancing precision for this purpose [132]. The plot shows a relationship between $(\alpha h\nu)^2$ and photon energy (hν), with α representing the absorption coefficient and hν denoting photon energy. The bandgap energy can be determined by identifying where the tangent line intersects the energy axis at the steepest part of the curve. Subsequently, the bandgap energy can be calculated using a specific equation [133].

$$Eg = hc/\lambda \qquad (2)$$

Eg denotes the bandgap energy, ***h*** signifies Planck's constant, ***c*** epitomises the speed of light and ***λ*** represents the wavelength corresponding to the absorption edge. Bano et. al synthesized photoluminescent N-CDs from Tamarindus indica leaves using the hydrothermal method at 210 °C. When exposed to UV light at 365 nm in a UV chamber, these N-CDs emitted a blue colour. A single absorption peak at 280 nm was observed, attributed to the π-π* electronic transition of the C=C bond [134]. Vaibhav Naik et al. discovered that nitrogen-doped carbon dots, synthesised using a hydrothermal method and ammonia, have potential applications in detecting dopamine and multicolour cell imaging. Their UV-VIS spectroscopy analysis revealed a peak at 278 nm (π-π*), indicating the presence of aromatic sp^2 domains. Furthermore, the addition of dopamine led to a red shift in absorption maxima, suggesting the formation of a ground-state complex between the carbon dots and dopamine [135].

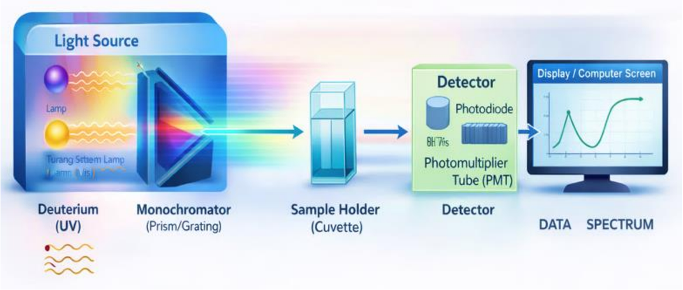

Figure 8: *A schematic representation of the setup employed for recording UV–visible absorption spectra*

6.5. Fourier Transform Infrared Spectroscopy

Fourier transform infrared (FTIR) spectroscopy is a widely employed technique to identify surface functional groups present on carbon quantum dots (CQDs) and to confirm successful surface passivation. A schematic overview of the general instrumentation is presented in Figure 9. The FTIR spectra of CQDs typically display a broad absorption band in the range of 3200–3500 cm^{-1}, which is attributed to the stretching vibrations of hydroxyl (–OH) and amine (–NH) groups, often arising from surface-bound functional moieties and adsorbed moisture [136],[137]. The appearance of absorption bands near 2900 cm^{-1} is generally associated with C–H stretching vibrations, indicating the presence of aliphatic carbon structures on the CQD surface [138]. Distinct peaks observed around 1700–1650 cm^{-1} correspond to the stretching vibrations of carbonyl (C=O) groups, confirming the presence of carboxylic functionalities formed during oxidative carbonisation processes [139]. Additionally, absorption bands in the region of 1600–1550 cm^{-1} are commonly assigned to C=C stretching of aromatic or graphitic domains and N–H bending vibrations, suggesting partial graphitisation and nitrogen incorporation within the CQD framework [3]. The presence of C–O stretching vibrations is evidenced by peaks appearing between 1200 and 1100 cm^{-1}, which are indicative of hydroxyl, ether, or epoxy groups (C–O–C) on the CQD surface [65]. Lower wavenumber peaks in the range of 800–900 cm^{-1} are typically attributed to C–H bending or out-of-plane vibrations of aromatic rings [138].

The abundance of oxygen- and nitrogen-containing functional groups revealed by FTIR analysis highlights the hydrophilic nature and excellent aqueous dispersibility of CQDs, which are crucial for their fluorescence behaviour and metal ion sensing performance [9]. While FTIR provides valuable insight into surface chemistry and functional group distribution, it offers limited information regarding the detailed core structure or heteroatom coordination within CQDs. Therefore, FTIR analysis is often complemented with other characterisation techniques for comprehensive structural evaluation [138].

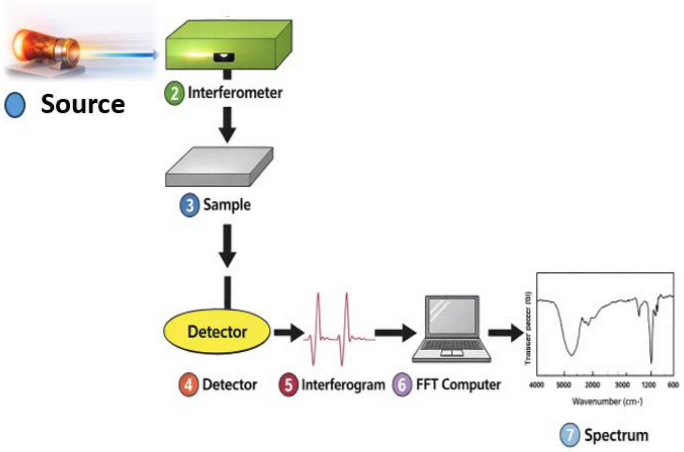

Figure 9: *Diagram representing the basic configuration employed for FTIR measurements*

7. Fluorescence-Based Sensing Applications of Carbon Quantum Dots

One of the most distinctive advantages of CQDs is the ability to tailor their fluorescence characteristics through controlled synthesis and surface engineering. Particle size, degree of graphitisation, surface oxidation, and heteroatom incorporation directly influence band gap energies and emission wavelengths. Smaller CQDs generally exhibit blue-shifted emission due to stronger confinement effects, whereas larger or surface-modified CQDs often display red-shifted fluorescence [140]. This tunability, combined with broad excitation spectra and narrow emission bands, makes CQDs versatile fluorescent probes for sensing applications.

Figure 10 illustrates the schematic representation of the photoinduced electron transfer (PET) process governing the fluorescence quenching behaviour.

The carbon quantum dots in fluorescence modulation are based on the special interactions of the excited states of CQDs with the analytes, and the mechanism predominantly depends on the electronic band of CQDs and the optical or chemical properties of the target. The Static quenching It is possible that the radiative recombination is inhibited by forming stable ground-state solutions with the surface functional groups (e.g., carboxyl, amine, or thiol) by the heavy metal ions on CQDs, and thereby avoiding radiative recombination without affecting the fluorescence lifetime significantly, as was shown in Fe^{3+} sensors where the complexation alters the absorption character but preserves the decay kinetics. More fundamentally, dynamic quenching is significant when the excited CQD and the analyte have spectral overlap, with a preference for FRET under conditions of proximity and strong coupling between the two dipole charges, where the former electronically transfers energy to the electron donor and the latter electronically transfers energy to the electron acceptor [141]. In contrast, IFE is observed when the redox potential of the analyte is no longer favourable. The excited CQD undergoes direct absorption or emission of the excitation light or emission light by the quencher without energy transfer, as has been demonstrated systematically in the graphene quantum dots under different pH conditions [142]. Photoinduced electron transfer (PET): This occurs when the redox potential of the analyte matches that of the excited CQD, which is frequently the cause of such strong quenching to electron-deficient ions as Fe^{3+} or Cr^{6+} [143]. A recent study has shown that solvent-sensitive surface activity in N, S-doped CQDs can directly determine the dominance of static- or dynamic-quenching pathways, reflecting the role of surface chemistry in tuning mechanism and sensitivity. Notably, these processes do not work alone; in most real-world sensing systems, IFE, PET, and FRET synergetically interact, and in order to isolate each mechanism, lifetime measurements and spectral analysis of a combination are necessary to determine which process is selective to a given heavy metal ion [144].

In fluorescence-based sensing, CQDs function as signal transducers whose emission intensity, wavelength, or lifetime changes in response to interactions with target analytes. These interactions may occur through adsorption, coordination bonding, electrostatic attraction, or redox reactions at the CQD surface [145]. Quantitative analysis is commonly achieved by establishing a linear relationship between fluorescence response and analyte concentration, allowing CQDs to serve as sensitive and reproducible sensing platforms [146].

Surface functionalization plays a crucial role in determining the selectivity of CQD-based sensors. The abundance of oxygen- and nitrogen-containing functional groups such as carboxyl, hydroxyl, amino, and amide moieties on CQD surfaces enables strong interactions with specific target species [147]. By modifying surface chemistry or introducing selective ligands, CQDs can be engineered to preferentially recognise and bind particular analytes, including metal ions, small molecules, and biomacromolecules [7].

Fluorescence modulation in CQDs may arise from several mechanisms, among which fluorescence quenching is most commonly exploited for sensing. Förster resonance energy transfer (FRET) has been widely applied in CQD-based sensors, where CQDs act as fluorescent donors and transfer energy to suitable acceptors in a distance-dependent manner [148]. Effective FRET requires spectral overlap between CQD emission and acceptor absorption, as well as donor–acceptor separation typically within 5–10 nm. The broad absorption range and tunable emission of CQDs allow precise control over such spectral overlaps, making them excellent candidates for FRET-based sensing systems [149].

These features of structure determine the dominance of the quenching pathway when metal ions are added. As an example, weakly bound surface ligands, including -COOH, -OH, and $-NH_2$, can bind strongly with the cations, forming efficient photoinduced electron transfer (PET) between the excited CQDs and the metal centre, resulting in fluorescence suppression [150]. Where there is spectral overlap between the CQD emission and the absorption band of the analyte, the FRET or inner filter effects can be realised.

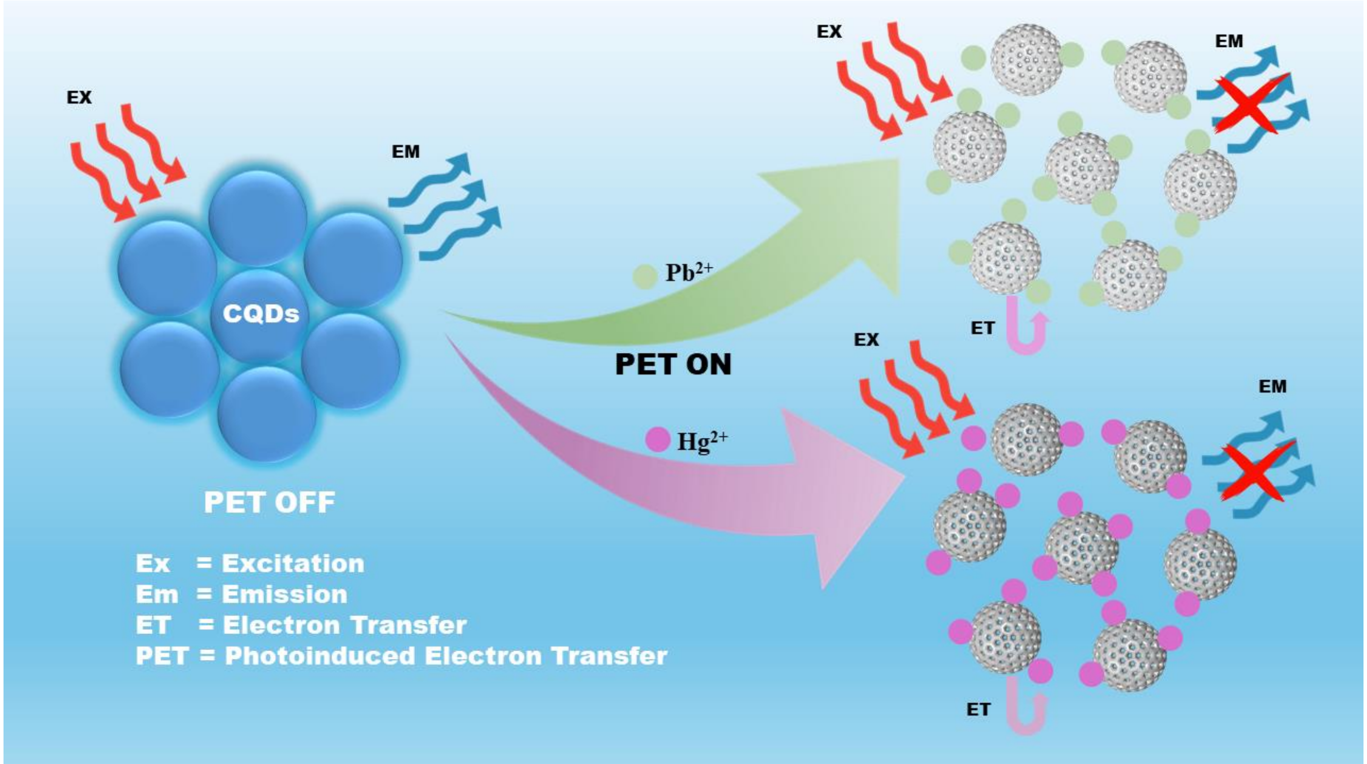

Figure 10: *PET Quenching Mechanism*

In the meantime, strongly defective surfaces might encourage the small-scale structure formation, and more weakly interacting interfaces might encourage dynamic collisional quenching [151].

Notably, sensing selectivity derives from preferential binding affinities when the oriented surface functionalities are compared to the particular ionic radii or redox potentials. As an illustration, sulfur- or nitrogen-bearing locations can tend to increase the recognition of softer acids like Hg^{2+}, whereas oxygen groups can prefer a more rigid metal ion. This leads to the logical approach of tuning electron-transfer probability by careful control of passivation, doping, and surface charge to achieve enhanced analytical discrimination [152].

In addition to FRET, fluorescence responses in CQDs can be influenced by the inner filter effect (IFE), static quenching, and dynamic quenching. IFE occurs when absorbing species in the system attenuate the excitation or emission light, leading to reduced fluorescence intensity without affecting fluorescence lifetime. Static quenching is when the fluorophore (e.g., CQDs) reacts with the quencher to form a non-fluorescent complex, usually with heavy metal ions [153],[154],[155]. This occurs before the fluorophore is exposed to light in a process that prevents fluorescence emission. The quenching depends upon the formation of a stable complex and is generally characterized to have a different temperature and concentration-dependent behaviour from the other mechanisms [156]. Li, Zhaofa, et al. synthesised a hybrid nanoprobe composed of N-doped CQDs and L-cysteine-capped CdSe/ZnS QDs combined with Cu^{2+} to form a stable complex, leading to the static quenching of L-cysteine-capped CdSe/ZnS QDs [157].

Whereas dynamic quenching results from collisional interactions in the excited state. In dynamic quenching, the quencher molecule gets to the vicinity of the fluorophore after the

Table 3
Recent green CQDs produced by the Bottom-Up approach

Source	Target	Readout	Synthesis method	QY (%)	Detection limit	Average Size & Color	Ref
Mango leaves	Fe^{2+}	Fluorescent	Pyrolysis 300 °C for 3 hrs	~18.2%	0.62 ppm	Blue 1–5 nm	[162]
Cabbage	Fe^{3+}	Fluorescent	Hydrothermal 140 °C for 5 h		1.72 x 10−7M	2–4 nm	[35]
CQDs/ZnO/CdS NPs	Fe^{3+}	Fluorescence	Hydrothermal 200 °C for 5 h		1.72 × 10−7 M		[36]
banana juice	Cu^{2+}	Fluorescent	hydrothermal 150 °C for 4 h	32 %	0.3 µg mL−1	Blue 1.27 nm	[163]
biomass tar	Cu^{2+}	Fluorescent	reduction smelting process	27.3%	80 nmol/L	1.98 nm	[164]
Poplar wood powders	Cr^{3+}	Fluorescence	hydrothermal 180 °C for 8 h			Blue-Green 6-8nm	[165]
CQD@γ-Fe2O3	Hg^{2+}	Fluorescence	hydrothermal 3 h at 140 °C		0.376 nM	4.5–6.5 nm	[166]
Glucose N-CQD, B-CQD, and S-CQD	Fe^{3+},Ag+,Ca^{2+}	colorimetric	hydrothermal process 200°C for 6h		0.187mM(Fe3+) 0.391mM(Ca2+) –0.442mM(Ag+)	5-7nm	[38]
Polyalthia longifolia p-CQDs	Cd^{2+}	Fluorescent	hydrothermal 150 ◦C for 6h	22%	2.4 nM	Red 3.33 nm	[39]
excess sludge ESCQDs	heavy metal control	fluorescent	hydrothermal process 200 °C, time varied	28.472 %			[167]
corncob	Pb^{2+}, Cu^{2+}, Fe^{3+}, and Cr^{3+}	fluorescent	Hydrothermal 70–80◦C for 12 h		0.8550 µM/mL Fe3+, 2.8562 µM/mL Cr3+	White ~4 nm	[168]
cane molasses	Ag+, $Hg^{2+}$and Cu^{2+}	fluorescent	Hydrothermal 160 ◦C for 24 h			1.7 nm blue	[169]
5-dimethyl amino methyl furfuryl alcohol and o-phenylene diamine	Hg^{2+}	fluorescent	Hydrothermal 160 °C for 4 hr	12.0%	5.2 nM	Yellow 2.6-3.4 nm	[170]
L-tryptophan-mediated CQDs	Fe^{3+} and Hg^{2+}	fluorescent	Hydrothermal	7.6 %	1.2×10^{-5}M and 1.9×10^{-5} M	Blue 3.0-5.1 nm.	[171]
Bombax ceiba stem	Fe^{3+}/Cd^{2+}	fluorescent	Hydrothermal		1.9 µM	Blue 6.5 nm	[3]
Litsea glutinosa stem	Cu^{2+}/Hg^{2+}	fluorescent	Hydrothermal		0.1 µM and 0.2 µM	Green 7.5 nm	[12]

absorption of light. This energy is then transferred to the quencher upon the collision between the excited fluorophore and quencher, leading to decreased fluorescence [158]. This process is concentration-dependent and can be reversed. For all the types of collisions, the number of such collisions grows with the increase in temperature.

In recent years, CQDs have been extensively explored for heavy metal ion detection in aqueous environments, driven by increasing concerns over water pollution and public health. Toxic metal ions such as Hg^{2+}, Pb^{2+}, Cd^{2+}, Cu^{2+}, Fe^{3+}, and Cr^{6+} are persistent environmental contaminants that pose serious risks even at trace levels [159]. CQDs synthesised via sustainable and green routes have demonstrated exceptional sensitivity toward these ions, often achieving detection limits in the nano- to micromolar range [12],[148].

The strong affinity between metal ions and surface functional groups on CQDs enables efficient fluorescence modulation, primarily through quenching mechanisms. For instance, metal ions with high coordination tendencies can interact with carboxyl or amino groups on CQD surfaces, facilitating non-radiative recombination pathways and resulting in pronounced fluorescence suppression [3]. In some cases, fluorescence enhancement has also been observed due to surface passivation or aggregation-induced emission effects [160]. Importantly, the low cytotoxicity, excellent water solubility, and chemical stability of CQDs make them particularly suitable for environmental monitoring applications [161].

Despite the growing number of reports on CQD-based fluorescence sensors, systematic comparisons of their analytical performance, particularly for heavy metal detection, remain limited. Parameters such as limit of detection, linear response range, selectivity, reproducibility, and recovery efficiency vary significantly depending on synthesis methods, surface chemistry, and sensing mechanisms. A consolidated evaluation of these factors is necessary to identify performance trends and guide the rational design of next-generation CQD sensors.

To better illustrate the current state of research and identify emerging trends, Table 3 presents a representative selection of fluorescence-based carbon quantum dot sensors reported for heavy metal ion detection in water. The compiled studies reflect the diversity of sustainable carbon precursors and synthesis routes employed, as well as the resulting variations in sensing performance toward different metal ions. Collectively, these reports demonstrate that CQD surface chemistry and preparation strategy play a decisive role in determining sensitivity and selectivity, particularly for transition and post-transition metal ions. The comparison also reveals a general trend toward lower detection limits and improved performance when biomass-derived CQDs with abundant surface functional groups are employed, underscoring their suitability for environmentally relevant water monitoring applications.

7.1. Mercury (Hg^{2+}) Ions

Hg^{2+} is one of the most harmful heavy metals due to its high neurotoxicity, bioaccumulation and because it binds firmly with thiol containing biomolecules, causing irreversible damage to both the nervous and the renal systems [172]. The most frequent technologies are chemical precipitation (insoluble $HgS/Hg(OH)_2$ formation), activated carbon adsorption, ion exchange, and membrane filtration. Although effective in high concentrations, they are poor in selectivity at trace levels, form secondary sludge, are expensive to operate and have complex regeneration. Moreover, the high affinity of Hg^{2+} with natural organic matter tends to lower the removal efficiency.

Despite these dangers, mercury remains widely used in industrial activities such as colour-alkali production, battery manufacturing, and electronic industries, increasing the likelihood of its release into aquatic environments. Therefore, continuous and sensitive monitoring of water resources near industrial regions is essential to prevent mercury-related ecological and health impacts [173].

CQDs and especially sulfur or nitrogen doped CQDs are rich in the number of-SH, $-NH_2$ or -COOH groups that strongly coordinate with the soft Lewis acid Hg^{2+}. The two main routes are surface complexation, chelation, and, in many cases, after formation of ground-state complexes, the electron transfer via photoinduced electron transfer (PET) or via static quenching [174]. Excessive specificity of Hg^{2+} and sulfur functionalities is improved in multi-ion systems. CQDs can be produced to recognise and capture ultra-low concentrations of a molecule at once, unlike precipitation, and do not form toxic by-products.

In one study, sulfhydryl-functionalized carbon quantum dots (HS-CQDs) were synthesised via a straightforward one-pot hydrothermal route and employed as a fluorescent "turn-off" probe for mercury ions (Hg^{2+}). The introduction of –SH groups on the CQD surface enhanced the binding affinity toward Hg^{2+}, facilitating the formation of non-fluorescent complexes and promoting electron transfer that leads to fluorescence quenching [175]. These HS-CQDs showed a good linear response to Hg^{2+} concentrations between 0.45 and 2.1 μM and achieved a low detection limit of 12 nM, demonstrating the system's high sensitivity. The practical applicability of this sensor was further validated through the successful detection of Hg^{2+} in real environmental samples, showcasing its potential utility for monitoring mercury contamination in water matrices [175].

Xiang, Jun, et al. synthesised biomass-derived carbon dots from Chenpi (dried citrus peel) via a green hydrothermal approach, serving as label-free fluorescent probes for mercury detection. These biomass CQDs displayed strong fluorescence emission and excellent stability in aqueous environments, and their photoluminescence intensity decreased in the presence of Hg^{2+} ions due to effective quenching interactions. The fluorescence response exhibited a clear linear relationship over the concentration range of 10–300 nM, with a remarkably low detection limit of approximately 7.0 nM, indicating highly sensitive detection capabilities [176].

7.2. Lead (Pb^{2+}) Ion

Pb^{2+} exposure leads to developmental defects, neurological dysfunction, and cardiovascular toxicity, especially in children. It is very persistent and mobile in water systems and thus continuous monitoring is necessary. It primarily exists in three oxidation states: Pb(0), Pb(II), and Pb(IV). A major contributor to lead contamination in drinking water is the corrosion of pipes and plumbing fixtures containing lead, especially under acidic conditions [177]. The permissible concentration of lead in drinking water has been reported to be approximately 15 ppb [178]. Various inorganic nanomaterials, including ZnS, gold nanoparticles, CdS, polymer dots, and enzyme-based sensors, have been explored as fluorescent probes for detecting Pb^{2+} ions. However, these approaches are often limited by high costs. Consequently, the development of cost-effective and environmentally friendly sensing materials remains an active research area [179].

Commonly used methods include precipitation, coagulation, flocculation, electrochemical treatment and adsorption on clays or biosorbents [180]. These techniques are usually however slow kinetics, low efficiency below ppm-ppb, and highly pH dependent. Sludge control and cation exchange are also significant disadvantages.

The presence of oxygen and nitrogen functional groups on the surface of CQD allows several coordination sites with Pb^{2+}. The usual result of binding is either PET or static quenching as a result of the donation of electrons to the empty orbitals of Pb^{2+} by surface ligands [181]. Heteroatom doping enhances the density of charges and stability of the complex, which is reflected in the minimum detection and selectivity.

For instance, Kumar et al. synthesised CQDs using *Ocimum sanctum* and applied them to detect Pb^{2+} in real water samples. They observed fluorescence quenching in the presence of Pb^{2+} ions, achieving a detection limit of 0.59 nM and a quantum yield of 9.3%. This quenching was attributed to electron–hole recombination, resulting from the strong interaction between the empty d-orbitals of Pb^{2+} ions and the amine groups on the CQD surface [182].

Nitrogen-doped CQDs (N-CQDs) prepared from *Lantana camara* berries have been investigated in detail to understand both dynamic and static fluorescence quenching mechanisms. Stern–Volmer analysis at multiple temperatures indicated a direct correlation between quenching constant and temperature. These N-CQDs effectively detect Pb^{2+} in human urine, serum, and water samples, with a notable decrease in fluorescence intensity at 450 nm as Pb^{2+} concentration increased, demonstrating high selectivity [183].

CQDs with an average size of 3.5 nm, synthesised from sugar, also show potential for Pb^{2+} detection. Fluorescence quenching in these CQDs occurs through carboxylate-induced aggregation, which was confirmed using FTIR and XRD analyses. They have been successfully applied to detect Pb^{2+} in real water samples [184]. Additionally, CQDs derived from bamboo leaves have been utilised for selective Pb^{2+} detection in river water, offering practical applications in environmental monitoring and water safety management [185].

7.3. Copper (Cu^{2+}) Ion

Copper is a naturally occurring heavy metal that is widespread in the environment and plays a vital biological role. It acts as an essential mineral, facilitating various enzymatic functions in plants and animals [186]. However, excessive copper exposure can be toxic, highlighting the importance of monitoring its levels in both ecosystems and living organisms. This has led to numerous studies focused on developing effective methods for Cu detection, with CQDs emerging as a promising approach for this purpose [187].

Chauhan et al. reported a dual “turn-on/off” sensor for Cu^{2+} and Cd^{2+} detection in aqueous solutions, using CDs derived from coconut coir via thermal calcination. In their study, Cu^{2+} ions caused quenching of the CD fluorescence, whereas Cd^{2+} induced an enhancement of fluorescence intensity. These changes were attributed to interactions between the metal ions and oxygen-containing groups on the CD surface: Cu^{2+} promoted non-radiative charge recombination leading to quenching, while Cd^{2+} increased the intrinsic radiative decay rate, enhancing fluorescence. The detection limits for Cu^{2+} and Cd^{2+} were found to be 0.28 nM and 0.18 nM, respectively, demonstrating the sensor’s applicability for monitoring these metals in wastewater [188].

A fluorescent paper-based CD sensor was also developed to detect Cu^{2+} ions in water through the photoinduced electron transfer (PET) mechanism [189]. The CDs were synthesized hydrothermally using radish as a precursor, resulting in CDs rich in functional groups capable of chelating Cu^{2+} and forming complexes that quenched fluorescence. The sensor exhibited a linear response for Cu^{2+} concentrations between 10–60 μM, with a limit of detection of 6.8 μM, and was successfully applied to real water samples. Additionally, this sensor demonstrated potential for acetic acid vapour detection [189].

Blue-emitting CDs (BCDs) were fabricated using palm kernel shell and urea via microwave irradiation [190]. When tested in aqueous media, Cu^{2+} ions induced significant fluorescence quenching, which was attributed to electrostatic interactions between the metal ions and CDs. The CDs could detect Cu^{2+} over a 0–0.5 mM concentration range, with a detection limit of 0.05 mM. Beyond sensing, these BCDs were further employed for bacterial cell imaging and as fluorescent inks, highlighting their utility as reliable tools for monitoring Cu in environmental and biological systems [190].

7.4. Iron (Fe) Ion

Iron (Fe), despite being vital biologically, surplus Fe^{3+} can prominently drive the generation of reactive oxygen species, resulting in oxidative stress, organ injury, and a decrease in water quality. In aquatic environments, iron is frequently detected in drinking water and municipal wastewater, particularly in regions influenced by iron- and steel-related industrial activities. The average daily iron intake for humans typically falls within the range of 10–50 mg [191]. According to the U.S. Environmental Protection Agency (EPA), a secondary maximum contaminant level of 0.3 ppm has been recommended for iron in drinking water, as elevated concentrations may lead to undesirable effects such as metallic taste, discolouration, and staining of plumbing fixtures. Although iron concentrations up to approximately 2 ppm are generally regarded as safe, prolonged exposure to higher levels can result in excessive iron accumulation in the body, potentially causing serious health disorders, including hemochromatosis, liver cirrhosis, and diabetes mellitus [192]. Treatment of iron is normally done through oxidation-precipitation or filtration. These are non-selective and simple but ineffective processes of differentiating between oxidation states. They are also highly pH-sensitive and cannot be used in complex matrices [193].

Fe^{3+} is highly attracted to carboxyl groups and hydroxyl groups; thus, surface coordination with CQDs can take place quickly. Due to the potency of Fe $^{3+}$ as an electron acceptor, fluorescence response is often directed by dynamic quenching or PET, in the presence or absence of aggregation. The non-radiative relaxation in Fe^{3+} is further enhanced by its paramagnetic feature, making it highly sensitive even in very low concentrations [194].

Song, Yuanyuan, et al. have synthesised wool keratin-derived nitrogen and sulfur co-doped CQDs via a simple hydrothermal method and exhibit excitation-dependent fluorescence behaviour. These nanoprobes demonstrate selective quenching of their fluorescence signal in the presence of Fe^{3+}, attributed to specific interactions between metal ions and functional groups (e.g., carboxyl and amino groups) on the CQD surface. The quenching response shows a clear, approximately linear correlation with Fe^{3+} concentration, indicating the potential of such green CQDs for rapid and selective detection of ferric ions in environmental water samples. The study also emphasises that the presence of other metal ions does not significantly interfere with the sensing performance, underscoring the selectivity of the CQD probe for iron ions under practical conditions [195].

For instance, Zhao, Pei, et al. used water hyacinth, a highly abundant aquatic plant, as a sustainable carbon source for the hydrothermal preparation of fluorescent carbon dots. These water hyacinth-derived CQDs displayed uniform particle size, strong blue photoluminescence, and excellent dispersibility in water [196]. When introduced to solutions containing Fe^{3+} ions, the fluorescence intensity of the CQDs decreased progressively with increasing ion concentration, enabling selective and sensitive detection. Notably, the detection limit achieved for Fe^{3+} with these biomass CQDs was as low as approximately 0.084 µM, with a broad linear response range up to several hundred micromolars, values that are well below typical regulatory thresholds for safe drinking water [196].

7.5. Chromium (Cr^{2+}) Ion

In aquatic systems, chromium is mainly found as trivalent [Cr(III)] and hexavalent [Cr(VI)] forms, which differ significantly in their biological and environmental effects [197]. While Cr(III) is an essential micronutrient important for animal growth and metabolism, Cr(VI) is highly toxic, exhibiting carcinogenic, mutagenic, and teratogenic properties [198]. Its high environmental mobility further increases the risk of widespread contamination, making its removal from wastewater critical for environmental and public health [199].

Cost-effective carbon quantum dots (CQDs) have been synthesised from lemon peel waste, showing strong photoluminescence, high aqueous stability, and a quantum yield of ~14% [200]. These CQDs functioned as an eco-friendly fluorescent probe for Cr(VI) detection with a detection limit of 73 nM and high selectivity, offering a rapid and sensitive method for water monitoring [200]. Similarly, nitrogen-doped CQDs derived from sugarcane bagasse have been reported for Cr(VI) adsorption [201]. Kinetic studies indicated that adsorption follows both pseudo-first and pseudo-second-order models, with the latter providing a better fit, suggesting chemisorption as the dominant mechanism. Boyd model analysis confirmed that external diffusion governs the rate of Cr(VI) removal [201].

8. Challenges and Future Perspective

Despite the rapid progress in the development of biomass-derived fluorescent carbon quantum dots for heavy metal sensing, several challenges must be addressed before their full-scale practical implementation. One of the primary limitations is the difficulty in translating laboratory-scale synthesis into large-scale, commercially viable production. Although biomass precursors offer sustainability and low cost, achieving consistent quality, reproducibility, and batch-to-batch uniformity remains a significant hurdle for real-world deployment.

Another challenge lies in the relatively lower quantum yield of biomass-derived CQDs compared to chemically synthesised counterparts. While green synthesis routes reduce environmental impact, further optimization of reaction conditions, precursor selection, and surface passivation strategies is required to enhance fluorescence efficiency without compromising sustainability. In addition, the majority of existing studies focus on a limited number of metal ions, particularly Fe^{3+}, Hg^{2+}, and Cu^{2+}, leaving other environmentally hazardous metals insufficiently explored. Expanding CQD design toward target-specific sensing of a broader range of toxic ions remains an important research direction.

Selectivity is another critical concern, especially in complex water matrices containing multiple competing ions. A deeper understanding of metal–CQD interaction mechanisms, including fluorescence quenching pathways and surface binding phenomena, is essential for designing highly selective sensors. Furthermore, challenges related to purification, structural characterisation, and long-term stability must be resolved to ensure reliable performance in real environmental samples. The future perspectives of carbon quantum dots for sustainable synthesis and enhanced heavy metal detection are summarised in Figure 11.

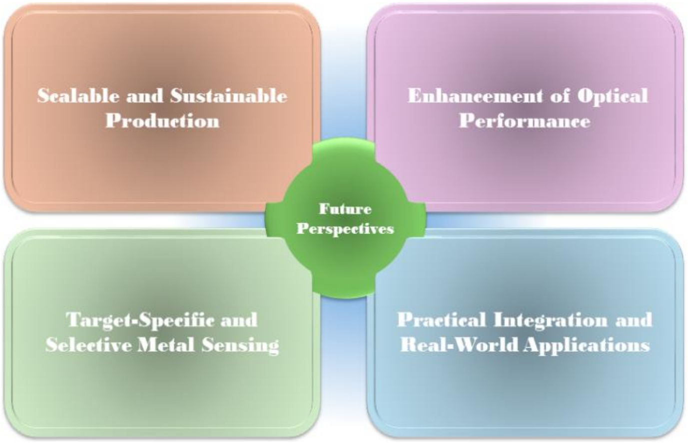

Figure 11: *Schematic representation illustrating the future perspectives of carbon quantum dots for sustainable synthesis, enhanced sensing performance, and practical heavy metal detection in water*

Future research should focus on rational surface engineering, heteroatom doping, and controlled synthesis using tailored biomass precursors to improve optical performance and metal specificity. Integrating CQDs into solid-state platforms, portable devices, and real-time monitoring systems will further enhance their applicability. Addressing these challenges will accelerate the transition of sustainable CQDs from experimental materials to practical tools for environmental monitoring.

9. Conclusion

This review highlights the significant progress toward the sustainable production of fluorescent carbon quantum dots and their growing role in heavy metal detection in water systems. Biomass-derived CQDs have emerged as an environmentally benign alternative to conventional semiconductor quantum dots, offering advantages such as low toxicity, biocompatibility, water solubility, and cost-effective synthesis from renewable resources. The bottom-up green synthesis approach, in particular, enables fine control over CQD surface chemistry and optical properties, which are critical for sensing applications.

The presence of diverse surface functional groups and the possibility of heteroatom doping allow CQDs to interact selectively with various heavy metal ions, making them highly sensitive fluorescent probes. Their low detection limits, photostability, and adaptability to different sensing environments underscore their potential for environmental applications. However, challenges related to large-scale production, fluorescence efficiency, selectivity in complex matrices, and mechanistic understanding still require focused investigation.

Overall, sustainable CQDs represent a promising platform for next-generation heavy metal sensors. Continued research into green synthesis strategies, surface functionalization, and sensing mechanisms will not only improve detection performance but also contribute to the development of eco-friendly technologies for water quality monitoring and environmental protection.

Declaration

AI Disclosure: Artificial Intelligence (AI)-based tools were used in this study only as supportive instruments to improve the clarity and linguistic quality of the manuscript. AI was applied solely for grammatical correction, sentence refinement, and enhancement of readability. No AI tools were employed for content generation, experimental work, data analysis, interpretation of results, or formulation of scientific conclusions. All research findings, analyses, and critical evaluations were conducted independently by the authors, who take full responsibility for the originality, accuracy, and ethical integrity of the manuscript.

Author Contribution Statement: M. A. A. contributed to conceptualization, data curation, formal analysis, and preparation of the original draft. J. A. was responsible for conceptualization, methodology development, visualization, data interpretation, and preparation of the original draft. A. R. provided visualization and technical support. R. contributed to visualization and technical assistance. All authors reviewed and approved the final manuscript.

Competing Interests: The authors declare that they have no known competing financial interests or personal relationships that could have appeared to influence the work reported in this paper.

Consent to Publish: The authors are agreed to publish version of the manuscript in this journal.

Ethical Issues: There are no ethical issues. All data in this paper is publicly available.

Funding Statement: This research did not receive any specific grant from funding agencies in the public, commercial, or not-for-profit sectors.

References

1. Jayaprakash, N., et al., Carbon nanomaterials: revolutionizing biomedical applications with promising potential. 2024.
2. Wang, X., et al., A mini review on carbon quantum dots: preparation, properties, and electrocatalytic application. 2019. 7: p. 671.
3. Akhtar, M.A., et al., Eco-friendly synthesis of N-doped carbon quantum dots from Bombax ceiba stem: A photophysical study with exploratory sensing of Fe3+/Cd2+ and dye degradation. 2025. 78: p. 108704.
4. Cayuela, A., et al., Semiconductor and carbon-based fluorescent nanodots: the need for consistency. 2016. 52(7): p. 1311-1326.
5. Liu, M.L., et al., Carbon dots: synthesis, formation mechanism, fluorescence origin and sensing applications. 2019. 21(3): p. 449-471.
6. Hagiwara, K., S. Horikoshi, and N.J.C.A.E.J. Serpone, Photoluminescent carbon quantum dots: synthetic approaches and photophysical properties. 2021. 27(37): p. 9466-9481.
7. Shabbir, H., E. Csapó, and M.J.I. Wojnicki, Carbon quantum dots: the role of surface functional groups and proposed mechanisms for metal ion sensing. 2023. 11(6): p. 262.
8. Gulati, S., et al., Eco-friendly and sustainable pathways to photoluminescent carbon quantum dots (CQDs). 2023. 13(3): p. 554.
9. Dhariwal, J., G.K. Rao, and D.J.R.S. Vaya, Recent advancements towards the green synthesis of carbon quantum dots as an innovative and eco-friendly solution for metal ion sensing and monitoring. 2024. 2(1): p. 11-36.
10. Nguyen, K.G., et al., Investigating the effect of N-doping on carbon quantum dots structure, optical properties and metal ion screening. 2022. 12(1): p. 13806.
11. Xu, H., et al., Research on green synthesis and performance analysis of biomass-derived carbon quantum dots. 2025. 227: p. 120775.
12. Anum, J., et al., Green-synthesized amino-rich carbon quantum dots: A dual-function platform for fluorescent detection of heavy metals and degradation of malachite green dye. 2025. 77: p. 108472.
13. Zhu, L., et al., State-of-the-art on the preparation, modification, and application of biomass-derived carbon quantum dots. 2020. 59(51): p. 22017-22039.
14. Wu, J., et al., Synthesis and applications of carbon quantum dots derived from biomass waste: a review. 2023. 21(6): p. 3393-3424.
15. Šafranko, S., et al., An overview of the recent developments in carbon quantum dots—promising nanomaterials for metal ion detection and (bio) molecule sensing. 2021. 9(6): p. 138.
16. Singh, P., et al., Assessment of biomass-derived carbon dots as highly sensitive and selective templates for the sensing of hazardous ions. 2023. 15(40): p. 16241-16267.
17. Lim, S.Y., W. Shen, and Z.J.C.S.R. Gao, Carbon quantum dots and their applications. 2015. 44(1): p. 362-381.
18. Xu, Q., et al., Function-driven engineering of 1D carbon nanotubes and 0D carbon dots: mechanism, properties and applications. 2019. 11(4): p. 1475-1504.
19. Xu, X., et al., Electrophoretic analysis and purification of fluorescent single-walled carbon nanotube fragments. 2004. 126(40): p. 12736-12737.
20. Hu, S., et al., Laser synthesis and size tailor of carbon quantum dots. 2011. 13: p. 7247-7252.
21. Pillar-Little, T.J., et al., Superior photodynamic effect of carbon quantum dots through both type I and type II pathways: Detailed comparison study of top-down-synthesized and bottom-up-synthesized carbon quantum dots. 2018. 140: p. 616-623.
22. Yang, S., et al., Fabrication of carbon-based quantum dots via a "bottom-up" approach: Topology, chirality, and free radical processes in "Building Blocks". 2023. 19(31): p. 2205957.
23. Kaur, I., et al., Chemical-and green-precursor-derived carbon dots for photocatalytic degradation of dyes. 2024. 27(2).
24. Nammahachak, N., et al., Hydrothermal synthesis of carbon quantum dots with size tunability via heterogeneous nucleation. 2022. 12(49): p. 31729-31733.
25. Lima-Tenorio, M.K., et al., Magnetic nanoparticles: In vivo cancer diagnosis and therapy. 2015. 493(1-2): p. 313-327.
26. Msto, R.K., et al., Fluorescence turns on-off-on sensing of ferric ion and L-ascorbic acid by carbon quantum dots. 2023. 2023(1): p. 5555608.
27. Arumugam, N. and J.J.M.L. Kim, Synthesis of carbon quantum dots from Broccoli and their ability to detect silver ions. 2018. 219: p. 37-40.
28. Atchudan, R., et al., Hydrophilic nitrogen-doped carbon dots from biowaste using dwarf banana peel for environmental and biological applications. 2020. 275: p. 117821.
29. Thakur, S., et al., Valorization of food industrial waste: Green synthesis of carbon quantum dots and novel applications. 2023: p. 140656.
30. Al-Douri, Y., N. Badi, and C.H.J.L. Voon, Synthesis of carbon-based quantum dots from starch extracts: Optical investigations. 2018. 33(2): p. 260-266.
31. Sadegh Hassani, S., et al., Carbon-based Quantum Dots from Food Waste: Synthesis to Application in Food Safety. 2023.
32. Park, S.J., et al., Color tunable carbon quantum dots from wasted paper by different solvents for anti-counterfeiting and fluorescent flexible film. 2020. 383: p. 123200.
33. Bhunia, S.K., et al., Carbon nanoparticle-based fluorescent bioimaging probes. 2013. 3(1): p. 1473.
34. Lu, Z., et al., Potential application of nitrogen-doped carbon quantum dots synthesized by a solvothermal method for detecting silver ions in food packaging. 2019. 16(14): p. 2518.
35. Singh, H., et al., One-pot hydrothermal synthesis and characterization of carbon quantum dots (CQDs). 2020. 28: p. 1891-1894.
36. Nan, Z., et al., Carbon quantum dots (CQDs) modified ZnO/CdS nanoparticles based fluorescence sensor for highly selective and sensitive detection of Fe (III). 2020. 228: p. 117717.
37. Khan, Z.M., et al., Hydrothermal treatment of red lentils for the synthesis of fluorescent carbon quantum dots and its application for sensing Fe3+. 2019. 91: p. 386-395.
38. Aygun, A., et al., Hydrothermal synthesis of B, S, and N-doped carbon quantum dots for colorimetric sensing of heavy metal ions. 2024. 14(16): p. 10814-10825.
39. Kolaprath, M.K.A., et al., A facile, green synthesis of carbon quantum dots from Polyalthia longifolia and its application for the selective detection of cadmium. 2023. 210: p. 111048.
40. Singh, R., et al., Progress in microwave-assisted synthesis of quantum dots (graphene/carbon/semiconducting) for bioapplications: a review. 2019. 12: p. 282-314.
41. Nadagouda, M.N., T.F. Speth, and R.S.J.A.o.C.R. Varma, Microwave-assisted green synthesis of silver nanostructures. 2011. 44(7): p. 469-478.
42. Bhattacharyya, S., et al., Effect of nitrogen atom positioning on the trade-off between emissive and photocatalytic properties of carbon dots. 2017. 8(1): p. 1401.

43. Nazar, M., et al., Microwave Synthesis of Carbon Quantum Dots from Arabica Coffee Ground for Fluorescence Detection of Fe3+, Pb2+, and Cr3+. 2024. 9(18): p. 20571-20581.
44. Architha, N., et al., Microwave-assisted green synthesis of fluorescent carbon quantum dots from Mexican Mint extract for Fe3+ detection and bio-imaging applications. 2021. 199: p. 111263.
45. Chugh, R. and G. Kaur, Citrus sinensis agro-waste peels mediated CQDs-Ag nanocomposite potentiates numerous applications. 2023.
46. Zaman, A.S.K., et al., Properties and molecular structure of carbon quantum dots derived from empty fruit bunch biochar using a facile microwave-assisted method for the detection of Cu2+ ions. 2021. 112: p. 110801.
47. Monte-Filho, S.S., et al., Synthesis of highly fluorescent carbon dots from lemon and onion juices for determination of riboflavin in multivitamin/mineral supplements. 2019. 9(3): p. 209-216.
48. Suppan, T., et al., Fluorescent 'turn-on'porphyrin CQD nanoprobes for selective sensing of heavy metal ions. 2024: p. 111265.
49. Kaur, R., et al., Waste biomass-derived CQDs and Ag-CQDs as a sensing platform for Hg2+ ions. 2022. 29: p. 100813.
50. Kumari, A., et al., Synthesis of green fluorescent carbon quantum dots using waste polyolefins residue for Cu2+ ion sensing and live cell imaging. 2018. 254: p. 197-205.
51. Zhou, J., et al., Facile synthesis of fluorescent carbon dots using watermelon peel as a carbon source. 2012. 66(1): p. 222-224.
52. Abid, N., et al., Synthesis of nanomaterials using various top-down and bottom-up approaches, influencing factors, advantages, and disadvantages: A review. 2022. 300: p. 102597.
53. Sajini, T. and J.J.R.S. Joseph, Microwave-assisted synthesis of nanomaterials: a green chemistry perspective and sustainability assessment. 2025. 3(11): p. 4911-4935.
54. Kim, H.H., et al., Bottom-up synthesis of carbon quantum dots with high performance photo-and electroluminescence. 2018. 35(7): p. 1800080.
55. Ray, S., et al., Fluorescent carbon nanoparticles: synthesis, characterization, and bioimaging application. 2009. 113(43): p. 18546-18551.
56. Shaik, S.A., et al., Syntheses of N-doped carbon quantum dots (NCQDs) from bioderived precursors: a timely update. 2020. 9(1): p. 3-49.
57. El-Shabasy, R.M., et al., Recent developments in carbon quantum dots: properties, fabrication techniques, and bio-applications. 2021. 9(2): p. 388.
58. Wang, C., et al., Carbon quantum dots prepared by pyrolysis: investigation of the luminescence mechanism and application as fluorescent probes. 2022. 204: p. 110431.
59. Namdari, P., et al., Synthesis, properties and biomedical applications of carbon-based quantum dots: An updated review. 2017. 87: p. 209-222.
60. Dhandapani, E., N. Duraisamy, and P.J.M.T.P. Periasamy, Highly green fluorescent carbon quantum dots synthesis via hydrothermal method from fish scale. 2020. 26: p. A1-A5.
61. Ou, S.-F., et al., N-doped carbon quantum dots as fluorescent bioimaging agents. 2021. 11(7): p. 789.
62. Saikia, T., J. Al-Jaberi, and A.J.A.o. Sultan, Synthesis and testing of monoethylene glycol carbon quantum dots for inhibition of hydrates in CO2 sequestration. 2021. 6(23): p. 15136-15146.
63. Tang, L., et al., Deep ultraviolet photoluminescence of water-soluble self-passivated graphene quantum dots. 2012. 6(6): p. 5102-5110.
64. Hola, K., et al., Photoluminescence effects of graphitic core size and surface functional groups in carbon dots: COO− induced red-shift emission. 2014. 70: p. 279-286.
65. Dager, A., et al., Synthesis and characterization of mono-disperse carbon quantum dots from fennel seeds: photoluminescence analysis using machine learning. 2019. 9(1): p. 14004.
66. Martindale, B.C., et al., Enhancing light absorption and charge transfer efficiency in carbon dots through graphitization and core nitrogen doping. 2017. 129(23): p. 6559-6563.
67. Zhang, W., et al., Large-area color controllable remote carbon white-light light-emitting diodes. 2015. 85: p. 344-350.
68. Yu, T., et al., A rapid microwave synthesis of green-emissive carbon dots with solid-state fluorescence and pH-sensitive properties. 2018. 5(7): p. 180245.
69. Kaur, G.A., et al., Structural and optical amendment of PVDF into CQDs through high temperature calcination process. 2021. 304: p. 130616.
70. Hu, S.-L., et al., One-step synthesis of fluorescent carbon nanoparticles by laser irradiation. 2009. 19(4): p. 484-488.
71. Hou, H., et al., Carbon quantum dots and their derivative 3D porous carbon frameworks for sodium-ion batteries with ultralong cycle life. 2015. 27(47): p. 7861-7866.
72. Arumugham, T., et al., A sustainable synthesis of green carbon quantum dot (CQD) from Catharanthus roseus (white flowering plant) leaves and investigation of its dual fluorescence responsive behavior in multi-ion detection and biological applications. 2020. 23: p. e00138.
73. Qiang, S., et al., New insights into the cellular toxicity of carbon quantum dots to Escherichia coli. 2022. 11(12): p. 2475.
74. Kolanowska, A., et al., Carbon quantum dots from amino acids revisited: Survey of renewable precursors toward high quantum-yield blue and green fluorescence. 2022. 7(45): p. 41165-41176.
75. Chandra, S., et al., Tuning of photoluminescence on different surface functionalized carbon quantum dots. 2012. 2(9): p. 3602-3606.
76. Luo, P.G., et al., Carbon "quantum" dots for optical bioimaging. 2013. 1(16): p. 2116-2127.
77. Arul, V., et al., Optical and Biomedical Features of Green Carbon Quantum Dots, in Green Carbon Quantum Dots: Environmental Applications. 2024, Springer. p. 85-116.
78. Tejwan, N., et al., Multifaceted applications of green carbon dots synthesized from renewable sources. 2020. 275: p. 102046.
79. Sun, Y.-P., et al., Quantum-sized carbon dots for bright and colorful photoluminescence. 2006. 128(24): p. 7756-7757.
80. Atchudan, R., et al., Green synthesized multiple fluorescent nitrogen-doped carbon quantum dots as an efficient label-free optical nanoprobe for in vivo live-cell imaging. 2019. 372: p. 99-107.
81. Ding, H., et al., Surface states of carbon dots and their influences on luminescence. 2020. 127(23).
82. Pan, J., et al., A novel and sensitive fluorescence sensor for glutathione detection by controlling the surface passivation degree of carbon quantum dots. 2017. 166: p. 1-7.
83. Omer, K.M.J.A. and b. chemistry, Highly passivated phosphorous and nitrogen co-doped carbon quantum dots and fluorometric assay for detection of copper ions. 2018. 410: p. 6331-6336.
84. Wang, F., et al., One-step synthesis of highly luminescent carbon dots in noncoordinating solvents. 2010. 22(16): p. 4528-4530.
85. Dong, Y., et al., Carbon-based dots co-doped with nitrogen and sulfur for high quantum yield and excitation-independent emission. 2013. 52(30).
86. Anilkumar, P., et al., Toward quantitatively fluorescent carbon-based "quantum" dots. 2011. 3(5): p. 2023-2027.
87. Wang, H., et al., High fluorescence S, N co-doped carbon dots as an ultra-sensitive fluorescent probe for the determination of uric acid. 2016. 155: p. 62-69.
88. Bourlinos, A.B., et al., Green and simple route toward boron doped carbon dots with significantly enhanced non-linear optical properties. 2015. 83: p. 173-179.
89. Zhou, J., et al., Facile synthesis of P-doped carbon quantum dots with highly efficient photoluminescence. 2014. 4(11): p. 5465-5468.
90. Qu, S., et al., Toward efficient orange emissive carbon nanodots through conjugated sp (2)-domain controlling and surface charges engineering. 2016.
91. Farshbaf, M., et al., Carbon quantum dots: recent progresses on synthesis, surface modification and applications. 2018. 46(7): p. 1331-1348.
92. Molaei, M.J.J.S.E., The optical properties and solar energy conversion applications of carbon quantum dots: A review. 2020. 196: p. 549-566.
93. Zhang, Z., et al., Progress of carbon quantum dots in photocatalysis applications. 2016. 33(8): p. 457-472.
94. Baker, S.N. and G.A.J.A.C.I.E. Baker, Luminescent carbon nanodots: emergent nanolights. 2010. 49(38): p. 6726-6744.
95. Gokus, T., et al., Making graphene luminescent by oxygen plasma treatment. 2009. 3(12): p. 3963-3968.
96. Cao, L., et al., Photoluminescence properties of graphene versus other carbon nanomaterials. 2013. 46(1): p. 171-180.
97. Yuan, F., et al., Bright multicolor bandgap fluorescent carbon quantum dots for electroluminescent light-emitting diodes. 2017. 29(3): p. 1604436.
98. Srivastava, I., et al., Rational design of surface-state controlled multicolor cross-linked carbon dots with distinct photoluminescence and cellular uptake properties. 2021. 13(50): p. 59747-59760.

99. Chan, K.K., S.H.K. Yap, and K.-T.J.N.-m.l. Yong, Biogreen synthesis of carbon dots for biotechnology and nanomedicine applications. 2018. 10: p. 1-46.
100. Park, Y., et al., Improving the functionality of carbon nanodots: doping and surface functionalization. 2016. 4(30): p. 11582-11603.
101. Zhang, F., et al., Photoluminescent carbon quantum dots as a directly film-forming phosphor towards white LEDs. 2016. 8(16): p. 8618-8632.
102. Fang, L.-y. and J.-t.J.N.C.M. Zheng, Carbon quantum dots: Synthesis and correlation of luminescence behavior with microstructure. 2021. 36(3): p. 625-631.
103. Cao, L., et al., Carbon dots for multiphoton bioimaging. 2007. 129(37): p. 11318-11319.
104. Kong, B., et al., Carbon dot-based inorganic–organic nanosystem for two-photon imaging and biosensing of pH variation in living cells and tissues. 2012. 24(43): p. 5844.
105. Li, M., et al., Controlling the up-conversion photoluminescence property of carbon quantum dots (CQDs) by modifying its surface functional groups for enhanced photocatalytic performance of CQDs/BiVO4 under a broad-spectrum irradiation. 2021. 47(8): p. 3469-3485.
106. Yuan, T., et al., Carbon quantum dots: an emerging material for optoelectronic applications. 2019. 7(23): p. 6820-6835.
107. He, P., et al., Growing carbon quantum dots for optoelectronic devices. 2018. 34(11): p. 1250-1263.
108. Dave, K. and V.G.J.N.E. Gomes, Carbon quantum dot-based composites for energy storage and electrocatalysis: Mechanism, applications and future prospects. 2019. 66: p. 104093.
109. Samantara, A.K., et al., Sandwiched graphene with nitrogen, sulphur co-doped CQDs: an efficient metal-free material for energy storage and conversion applications. 2015. 3(33): p. 16961-16970.
110. Chen, J. and K.J.M.C.F. Rong, Nanophotonic devices and circuits based on colloidal quantum dots. 2021. 5(12): p. 4502-4537.
111. Kim, J., et al., Recent progress of quantum dot-based photonic devices and systems: a comprehensive review of materials, devices, and applications. 2021. 2(3): p. 2000024.
112. Arul, V., et al., Carbon quantum dots for smart electronic devices, in Green Carbon Quantum Dots: Environmental Applications. 2024, Springer. p. 367-386.
113. Li, H., et al., Carbon quantum dots/TiO x electron transport layer boosts efficiency of planar heterojunction perovskite solar cells to 19%. 2017. 17(4): p. 2328-2335.
114. Naushad, M., et al., Nitrogen-doped carbon quantum dots (N-CQDs)/Co3O4 nanocomposite for high performance supercapacitor. 2021. 33(1): p. 101252.
115. Guo, R., et al., Functionalized carbon dots for advanced batteries. 2021. 37: p. 8-39.
116. Zhu, Y., et al., A carbon quantum dot decorated RuO 2 network: outstanding supercapacitances under ultrafast charge and discharge. 2013. 6(12): p. 3665-3675.
117. Rasal, A.S., et al., Carbon quantum dots for energy applications: a review. 2021. 4(7): p. 6515-6541.
118. Rooj, B. and U.J.V.J.o.C. Mandal, A review on characterization of carbon quantum dots. 2023. 61(6): p. 693-718.
119. Hu, Q., et al., Characterization and analytical separation of fluorescent carbon nanodots. 2017. 2017(1): p. 1804178.
120. Song, X., et al., Pressure-assisted preparation of graphene oxide quantum dot-incorporated reverse osmosis membranes: antifouling and chlorine resistance potentials. 2016. 4(43): p. 16896-16905.
121. Saikia, M., et al., Feasibility study of preparation of carbon quantum dots from Pennsylvania anthracite and Kentucky bituminous coals. 2019. 243: p. 433-440.
122. Lim, H., et al., Facile synthesis and characterization of carbon quantum dots and photovoltaic applications. 2018. 660: p. 672-677.
123. Cheng, C., et al., Carbon quantum dots from carbonized walnut shells: Structural evolution, fluorescence characteristics, and intracellular bioimaging. 2017. 79: p. 473-480.
124. Ali, M., et al., Gradient heating-induced bi-phase synthesis of carbon quantum dots (CQDs) on graphene-coated carbon cloth for efficient photoelectrocatalysis. 2022. 196: p. 649-662.
125. Baslak, C., et al., Green synthesis capacitor of carbon quantum dots from Stachys euadenia. 2024. 43(3): p. e14340.
126. Jawad, M.M. and L.A.J.J.o.O. Abdullah, Novel characteristics of CQDs synthesized by electrochemical method. 2024: p. 1-9.
127. Butt, H.-J., B. Cappella, and M.J.S.s.r. Kappl, Force measurements with the atomic force microscope: Technique, interpretation and applications. 2005. 59(1-6): p. 1-152.
128. Moraille, P., et al., Experimental methods in chemical engineering: Atomic force microscopy− AFM. 2022. 100(10): p. 2778-2806.
129. Thambiraj, S. and R.J.A.S.S. Shankaran, Green synthesis of highly fluorescent carbon quantum dots from sugarcane bagasse pulp. 2016. 390: p. 435-443.
130. Wang, Y. and A.J.J.o.M.C.C. Hu, Carbon quantum dots: synthesis, properties and applications. 2014. 2(34): p. 6921-6939.
131. Yang, Q., et al., Nitrogen-doped carbon quantum dots from biomass via simple one-pot method and exploration of their application. 2018. 434: p. 1079-1085.
132. Tian, J., et al., Carbon quantum dots/hydrogenated TiO2 nanobelt heterostructures and their broad spectrum photocatalytic properties under UV, visible, and near-infrared irradiation. 2015. 11: p. 419-427.
133. Ateia, E.E., O. Rabie, and A.T.J.T.E.P.J.P. Mohamed, Assessment of the correlation between optical properties and CQD preparation approaches. 2024. 139(1): p. 1-12.
134. Bano, D., et al., Green synthesis of fluorescent carbon quantum dots for the detection of mercury (II) and glutathione. 2018. 42(8): p. 5814-5821.
135. Naik, V., et al., Nitrogen-doped carbon dots via hydrothermal synthesis: naked eye fluorescent sensor for dopamine and used for multicolor cell imaging. 2019. 2(5): p. 2069-2077.
136. ReddyPrasad, P. and E.B.J.J.o.M.S. Naidoo, Ultrasonic synthesis of high fluorescent C-dots and modified with CuWO4 nanocomposite for effective photocatalytic activity. 2015. 1098: p. 146-152.
137. Sha, Y., et al., Hydrothermal synthesis of nitrogen-containing carbon nanodots as the high-efficient sensor for copper (II) ions. 2013. 48(4): p. 1728-1731.
138. Peng, J., et al., Graphene quantum dots derived from carbon fibers. 2012. 12(2): p. 844-849.
139. Sooryakanth, B., et al., Sustainable Conversion of Chitosan Waste into Nitrogen-Doped Graphene Quantum Dots: Green Synthesis Pathways and Biomedical Potential. 2025. 2(3): p. 173-199.
140. Liu, Z., et al., Photoluminescence of carbon quantum dots: coarsely adjusted by quantum confinement effects and finely by surface trap states. 2018. 61(4): p. 490-496.
141. Yu, J., et al., Unveiling the quenching mechanism of metal ions using solvent-driven N, S-doped carbon quantum dots. 2025. 162: p. 116948.
142. Lai, S., et al., Fluorescence sensing mechanisms of versatile graphene quantum dots toward commonly encountered heavy metal ions. 2023. 8(10): p. 3812-3823.
143. Wang, F., et al., Application of carbon quantum dots as fluorescent probes in the detection of antibiotics and heavy metals. 2025. 463: p. 141122.
144. Gao, Y., et al., Carbon quantum dots in spectrofluorimetric analysis: A comprehensive review of synthesis, mechanisms and multifunctional applications. 2025: p. 128066.
145. Preeyanka, N. and M.J.L. Sarkar, Probing how various metal ions interact with the surface of QDs: implication of the interaction event on the photophysics of QDs. 2021. 37(23): p. 6995-7007.
146. Lee-Montiel, F.T. and P.J.J.o.M.C.B. Imoukhuede, Engineering quantum dot calibration standards for quantitative fluorescent profiling. 2013. 1(46): p. 6434-6441.
147. Sun, H. and P.J.J.o.M.S. Wu, Tuning the functional groups of carbon quantum dots in thin film nanocomposite membranes for nanofiltration. 2018. 564: p. 394-403.
148. Molaei, M.J.J.A.M., Principles, mechanisms, and application of carbon quantum dots in sensors: a review. 2020. 12(10): p. 1266-1287.
149. Liang, Z., et al., Probing energy and electron transfer mechanisms in fluorescence quenching of biomass carbon quantum dots. 2016. 8(27): p. 17478-17488.
150. Zu, F., et al., The quenching of the fluorescence of carbon dots: a review on mechanisms and applications. 2017. 184(7): p. 1899-1914.
151. Mo, X., Fluorescent Carbon Quantum Dots Probe for Detection of Deoxygenated Hemoglobin. 2024, National University of Singapore (Singapore).
152. Kou, X., et al., A review: recent advances in preparations and applications of heteroatom-doped carbon quantum dots. 2020. 49(21): p. 6915-6938.

153. Lakowicz, J.R. and J.R.J.P.o.f.s. Lakowicz, Quenching of fluorescence. 1983: p. 257-301.
154. Genovese, D., et al., Static quenching upon adduct formation: a treatment without shortcuts and approximations. 2021. 50(15): p. 8414-8427.
155. Ding, G., et al., Recent advances in carbon quantum dots for antibiotics detection. 2024(0).
156. Sudewi, S., et al., Understanding Antibiotic Detection with Fluorescence Quantum Dots: A Review. 2024: p. 1-25.
157. Sedlář, O., et al., Long-Term Application of Organic Fertilizers in Relation to Soil Organic Matter Quality. 2023. 13(1): p. 175.
158. Liu, Y., et al., N-Doping CQDs as an efficient fluorescence probe based on dynamic quenching for determination of copper ions and alcohol sensing in baijiu. 2025. 35(5): p. 3239-3251.
159. Järup, L.J.B.m.b., Hazards of heavy metal contamination. 2003. 68(1): p. 167-182.
160. Sekar, A., R. Yadav, and N.J.N.J.o.C. Basavaraj, Fluorescence quenching mechanism and the application of green carbon nanodots in the detection of heavy metal ions: a review. 2021. 45(5): p. 2326-2360.
161. Yao, K., et al., Effects of carbon quantum dots on aquatic environments: comparison of toxicity to organisms at different trophic levels. 2018. 52(24): p. 14445-14451.
162. Singh, J., et al., Highly fluorescent carbon dots derived from Mangifera indica leaves for selective detection of metal ions. 2020. 720: p. 137604.
163. Chaudhary, N., et al., One-step green approach to synthesize highly fluorescent carbon quantum dots from banana juice for selective detection of copper ions. 2020. 8(3): p. 103720.
164. Xiang-Yi, D., et al., Synthesis of functionalized carbon quantum dots as fluorescent probes for detection of Cu2+. 2020. 48(10): p. e20126-e20133.
165. Song, Z., et al., Luminescent carbon quantum dots/nanofibrillated cellulose composite aerogel for monitoring adsorption of heavy metal ions in water. 2020. 100: p. 109642.
166. Panda, S., et al., CQD@ γ-Fe2O3 multifunctional nanoprobe for selective fluorescence sensing, detoxification and removal of Hg (II). 2020. 589: p. 124445.
167. Han, Y., et al., Green conversion of excess sludge to N-Ca self-doping sustainable carbon quantum dots with remarkable fluorescence enhancement and residual heavy metal reduction. 2022. 10(6): p. 108934.
168. Jagannathan, M., et al., Green synthesis of white light emitting carbon quantum dots: Fabrication of white fluorescent film and optical sensor applications. 2021. 416: p. 125091.
169. Fan, X., et al., Chiral CQD-based PL and CD sensors for high sensitive and selective detection of heavy metal ions. 2023. 137: p. 113620.
170. Jaison, A.M.C., et al., One pot hydrothermal synthesis and application of bright-yellow-emissive carbon quantum dots in Hg2+ detection. 2023. 33(6): p. 2281-2294.
171. Zalmi, G.A., et al., Hydrothermal Synthesis of Tartaric Acid Functionalized Amino Acid CQD for Sensing of Hg2+ and Fe3+ Ions in Aqueous Medium. 2024. 9(18): p. e202304825.
172. Cohen, J.T., D.C. Bellinger, and B.A.J.A.j.o.p.m. Shaywitz, A quantitative analysis of prenatal methyl mercury exposure and cognitive development. 2005. 29(4): p. 353-353. e24.
173. Salman, B.I., et al., Ultrasensitive green spectrofluorimetric approach for quantification of Hg (II) in environmental samples (water and fish samples) using cysteine@ MnO2 dots. 2023. 38(2): p. 145-151.
174. Pramanik, R.J.C., A review on fluorescent molecular probes for Hg2+ Ion detection: mechanisms, strategies, and future directions. 2025. 10(7): p. e202404525.
175. Yao, W., et al., Sulfhydryl functionalized carbon quantum dots as a turn-off fluorescent probe for sensitive detection of Hg 2+. 2021. 11(57): p. 36310-36318.
176. Xiang, J., et al., Synthesis of Carbon dots from Biomass Chenpi for the Detection of Hg 2+. 2023. 11(10).
177. Harrison, R., Lead pollution: causes and control. 2012: Springer Science & Business Media.
178. Gupta, A., et al., Paper strip based and live cell ultrasensitive lead sensor using carbon dots synthesized from biological media. 2016. 232: p. 107-114.
179. Dhaffouli, A.J.M.J., Eco-friendly nanomaterials synthesized greenly for electrochemical sensors and biosensors. 2025: p. 115051.
180. Badran, A.M., et al., Advancements in adsorption techniques for sustainable water purification: a focus on lead removal. 2023. 10(11): p. 565.
181. Al-Saidi, H.M.J.C.P., Recent advancements in organic chemosensors for the detection of Pb2+: a review. 2023. 77(9): p. 4807-4822.
182. Kumar, A., et al., Green synthesis of carbon dots from Ocimum sanctum for effective fluorescent sensing of Pb2+ ions and live cell imaging. 2017. 242: p. 679-686.
183. Bandi, R., et al., Green synthesis of highly fluorescent nitrogen–Doped carbon dots from Lantana camara berries for effective detection of lead (II) and bioimaging. 2018. 178: p. 330-338.
184. Ansi, V., N.J.S. Renuka, and A.B. Chemical, Table sugar derived Carbon dot–a naked eye sensor for toxic Pb2+ ions. 2018. 264: p. 67-75.
185. 1Liu, Z., et al., Ratiometric fluorescent sensing of Pb2+ and Hg2+ with two types of carbon dot nanohybrids synthesized from the same biomass. 2019. 296: p. 126698.
186. Goel, A., et al., A multi-responsive pyranone based Schiff base for the selective, sensitive and competent recognition of copper metal ions. 2021. 249: p. 119221.
187. Elkhatat, A.M., et al., Recent trends of copper detection in water samples. 2021. 45(1): p. 218.
188. Chauhan, P., et al., Usage of coconut coir for sustainable production of high-valued carbon dots with discriminatory sensing aptitude toward metal ions. 2020. 16: p. 100247.
189. Praneerad, J., et al., Multipurpose sensing applications of biocompatible radish-derived carbon dots as Cu2+ and acetic acid vapor sensors. 2019. 211: p. 59-70.
190. Balakrishnan, T., et al., Formation mechanism and application potential of carbon dots synthesized from palm kernel shell via microwave assisted method. 2022. 5(2): p. 150-166.
191. Intakes, S.C.o.t.S.E.o.D.R., et al., Dietary reference intakes for vitamin A, vitamin K, arsenic, boron, chromium, copper, iodine, iron, manganese, molybdenum, nickel, silicon, vanadium, and zinc. 2002: National Academies Press.
192. Shander, A., M. Cappellini, and L.J.V.s. Goodnough, Iron overload and toxicity: the hidden risk of multiple blood transfusions. 2009. 97(3): p. 185-197.
193. Korchef, A., et al., Iron removal from aqueous solution by oxidation, precipitation and ultrafi ltration. 2009. 9(1-3): p. 1-8.
194. Shahbaz, M., et al., Fluorescent/Photoluminescent Carbon Dots as a Sensor for the Selective and Sensitive Detection of Fe3+/Fe2+ Metal Ions. A Review of the Last Decade. 2025: p. 1-24.
195. Song, Y., et al., Green fluorescent nanomaterials for rapid detection of chromium and iron ions: wool keratin-based carbon quantum dots. 2022. 12(13): p. 8108-8118.
196. Zhao, P., et al., Facile and green synthesis of highly fluorescent carbon quantum dots from water hyacinth for the detection of ferric iron and cellular imaging. 2022. 12(9): p. 1528.
197. Bahadır, Z., et al., Separation and preconcentration of lead, chromium and copper by using with the combination coprecipitation-flame atomic absorption spectrometric determination. 2014. 20(3): p. 1030-1034.
198. Wang, N., et al., Visible light photocatalytic reduction of Cr (VI) on TiO2 in situ modified with small molecular weight organic acids. 2010. 95(3-4): p. 400-407.
199. Yang, W.-M., et al., Efficient reduction of Cr (VI) with carbon quantum dots. 2022. 7(27): p. 23555-23565.
200. Tyagi, A., et al., Green synthesis of carbon quantum dots from lemon peel waste: applications in sensing and photocatalysis. 2016. 6(76): p. 72423-72432.
201. Tohamy, H.A.S., M. El-Sakhawy, and S.J.J.o.F. Kamel, Eco-friendly synthesis of carbon quantum dots as an effective adsorbent. 2023. 33(2): p. 423-435.

Author(s) Bio

Muhammad Arslan Akhtar received his Master's degree in Chemistry from COMSATS University Islamabad. His research interests focus on the synthesis, characterization, and applications of carbon quantum dots, particularly for sensing applications. He has published two research articles in Q1 journals and is the author of three review articles in this field. He has extensive research experience in carbon quantum dot–based nanomaterials. Email: arslanimran042@gmail.com

Jalwa Anum received her Master's degree in Chemistry from COMSATS University Islamabad. Her research interests include the green synthesis, characterization, and sensing applications of carbon quantum dots. She has published two research articles in Q1 journals related to carbon quantum dots and has gained solid research experience in nanomaterial-based sensing systems.
Email: jilashah444@gmail.com

Abdul Rehman obtained his Bachelor's degree in Chemistry from Government College University Faisalabad. He is currently pursuing his Master's degree in Chemistry at the Institute of Molecular Plus, Tianjin University, China. His research focuses on the synthesis of nanomaterials, chemical sensors, and electrocatalysis. He has published a review article in *Nano Research*.
Email: abdul372r@gmail.com

Rabia obtained her Bachelor's degree in Applied Chemistry from GC University Faisalabad, Sahiwal Campus. She is currently pursuing her Master's degree in Chemistry at the Institute of Molecular Aggregation Science, Tianjin University, China. Her research focuses on the development of chemical sensors, and she has published one review article in *Chemical Research in Chinese Universities (CRCU)*.
Email: rabiaabdulshakoor4@gmail.com